

HIGH SPEED, LOW DRIVING VOLTAGE  
VERTICAL CAVITY MQW MODULATORS FOR  
OPTICAL INTERCONNECT AND COMMUNICATION

A DISSERTATION  
SUBMITTED TO THE DEPARTMENT OF  
ELECTRICAL ENGINEERING  
AND THE COMMITTEE ON GRADUATE STUDIES  
OF STANFORD UNIVERSITY  
IN PARTIAL FULFILLMENT OF THE REQUIREMENTS  
FOR THE DEGREE OF  
DOCTOR OF PHILOSOPHY

Hong Liu  
March 2001

© Copyright by Hong Liu 2001  
All Rights Reserved

I certify that I have read this dissertation and that in my opinion it is fully adequate, in scope and quality, as a dissertation for the degree of Doctor of Philosophy.

---

James S. Harris, Jr. (Principal Advisor)

I certify that I have read this dissertation and that in my opinion it is fully adequate, in scope and quality, as a dissertation for the degree of Doctor of Philosophy.

---

Martin M. Fejer

I certify that I have read this dissertation and that in my opinion it is fully adequate, in scope and quality, as a dissertation for the degree of Doctor of Philosophy.

---

David A. B. Miller

Approved for the University Committee on Graduate Studies:

# *Abstract*

The circuit-switched public network infrastructure is being stretched by the incredible growth of the internet and data transmission and limits of scaling set by Moore's law and the shortcomings of high speed electrical interconnects, which have high power consumption, poor signal integrity due to cross talk, large signal skew and jitter. Vertical cavity multiple quantum well (MQW) optical modulators, which offer high bandwidth, high contrast ratio, low power consumption and easy two-dimensional integration with silicon electronics, offer the promise to relieve the bottleneck in dense interconnect and data communication. The devices consist of MQWs in a Fabry-Perot cavity configured as p-i-n diodes. The absorptive characteristics of the MQW region can be modified through a field induced absorption change, known as the quantum-confined Stark effect (QCSE). This absorption change modulates the optical reflection of the device.

High-speed modulation and low driving voltage are the keys for the device's practical use. At lower optical intensity operation, the ultimate limitation in speed will be the RC time constant of the device itself and the parasitics of the microwave probe pads. At high optical intensity, the large number of photo generated carriers in the MQW region will limit the performance of the device through photo carrier related voltage drop and exciton saturation. The focus of this thesis is the optimization of MQW material and cavity design, minimization of the parasitic capacitance of the probe pads for high speed, low voltage and high contrast ratio operation. The design, fabrication and high-speed characterization of devices of different sizes, with different bias voltages and termination resistor are presented. We demonstrated a modulator, with a high contrast ratio of 11dB, a small driving voltage of 3.5V and an  $f_{3dB}$  bandwidth greater than 18GHz. If the device is used as a high-speed photodetector, it has high quantum efficiency of 95% and an  $f_{3dB}$  bandwidth greater than 10GHz. Carrier dynamics under ultra-fast laser excitation and high-speed photocurrent response are also investigated.

# *Acknowledgments*

This work would not have been possible without the help of many people. First of all, I am grateful to my advisor Professor James “Coach” Harris. His unique way of managing his research group gives us tremendous freedom to pursue our own research interest and benefits us individually in the long term. His kindness towards his students makes my life at Stanford the most pleasant experience and I shall cherish it for the rest of my life.

I am grateful to Professor Krishna Saraswat for serving as my orals chairman and especially grateful to Professor Martin Fejer and Professor David A. B. Miller for serving on my orals committee and for reading my dissertation.

I am grateful to Professor Tom Lee for his generosity so that I could use the expensive high frequency equipment in his lab. I learned a great deal from the high frequency laboratory course that he taught.

This work would not have been possible without the help of Professor David A. B. Miller and his group. I am very grateful for Professor Miller’s technical advice, discussion and the classes he taught at Stanford, which really brought me into the deep world of optoelectronics. I would like to thank Micah Yairi and Ryohei Urata for their help on the pump-probe measurement and the wonderful discussion with them from optical gates to the every tiny detail of experimental setup.

I would like to thank past and present members of the Harris group. Especially I would like to thank Chien-Chung Lin, who grew the wafers for me in the past years. I started the very first piece of GaAs processing with Chris Coldren and I am grateful for his knowledge and patience. I am also grateful to Erji Mao and Wayne Martin for their help inside and outside the cleanroom. They are always willing to help me move the heavy instruments and correct my English in my papers and presentations. Our computer system guru Vicent Gambin and Wayne Martin deserve thanks for their time and effort. Many thanks to

the daily lunch friends Xian Liu and Fely Barrera for sharing many entertaining stories and making my daily life interesting.

Our administrative assistants, Gail Chun-Creech and Lu Miao, have offered us great help in keeping our group functional. Our group wouldn't have survived without them and I am truly grateful to their work.

Finally, I am grateful to my parents in China. Although they are so far away, I can always feel their strong support and encouragement. They set such a high standard for me, ever since I was a little girl. I would like to dedicate this dissertation to them.

Last but not least, I would like to thank my husband, Alex Yunzhong Chen, for his love and support over the years.

The work for this dissertation was funded by the Army Research Office under contracts DAAH04-96-1-002 and DAAG55-97-1-002.

# *Table of Content*

Abstract.....	iv
Acknowledgments .....	v
Table of Content .....	vii
List of Figures.....	xi
<b>Chapter 1 Introduction</b> .....	<b>1</b>
1.1 Optical Interconnects .....	1
1.1.1 Power consumption.....	1
1.1.2 Bandwidth.....	3
1.1.3 Crosstalk and other advantages.....	3
1.2 Transmitter Solutions: VCSEL vs Modulator.....	4
1.3 Other Applications .....	6
1.4 Organization.....	7
<b>Chapter 2 Background</b> .....	<b>9</b>
2.1 Quantum Confined Stark Effect.....	9
2.1.1 Quantum well.....	9
2.1.2 Quantum confined Stark effect .....	11
2.1.3 Quantum confined Stark shift - well width dependence .....	13
2.2 Asymmetric Fabry-Perot modulator .....	14
2.2.1 Modulator configuration .....	14
2.2.2 Asymmetric Fabry-Perot reflection modulator .....	15
<b>Chapter 3 Device Design for High Speed Operation</b> .....	<b>21</b>
3.1 Low Driving Voltage and Large Absorption Change .....	21
3.2 High Speed Operation.....	23
3.2.1 Low optical intensity - RC limited .....	24
3.2.1.1 Series resistance $R_s$ .....	25
3.2.1.2 Modulator capacitance $C_{dev}$ and probe pad capacitance $C_{pad}$ .....	27
3.2.2 High optical intensity .....	28
3.2.2.1 Exciton saturation .....	28
3.2.2.2 Photovoltage screening .....	31
3.2.2.3 Thermal effect.....	34

3.3	Transmission Line Structure .....	35
<b>Chapter 4</b>	<b>Device Fabrication and DC Characterization</b>	<b>37</b>
4.1	Epitaxial Structure .....	37
4.2	Device Fabrication .....	40
4.2.1	Processing steps .....	40
4.2.2	Photo BCB processing .....	44
4.3	DC Characteristics .....	47
<b>Chapter 5</b>	<b>High Speed Characterization</b>	<b>51</b>
5.1	Equivalent Circuit Extraction .....	51
5.1.1	Microwave scattering parameters .....	51
5.1.2	Accurate de-embedding technique.....	53
5.1.3	Resistance and capacitance of the intrinsic modulator diode .....	56
5.2	High Speed E-O Response.....	61
5.2.1	Measurement setup .....	61
5.2.2	Results and discussions.....	62
<b>Chapter 6</b>	<b>Carrier Dynamics and Photocurrent Response</b>	<b>67</b>
6.1	Carrier Dynamics .....	67
6.1.1	Photovoltage .....	67
6.1.1.1	Carrier sweep-out mechanism .....	67
6.1.1.2	Photo-induced electric screening .....	73
6.1.1.3	Diffusive conduction recovery.....	75
6.1.1.4	Photovoltage evolution .....	78
6.1.2	Pump/probe measurement setup .....	79
6.1.3	Results and discussion .....	81
6.2	High Speed Photocurrent .....	84
6.2.1	High speed dual function photodetector .....	84
6.2.2	Characterization and discussion.....	88
<b>Chapter 7</b>	<b>Conclusions</b>	<b>93</b>
7.1	Summary .....	93
7.2	Future Work .....	94

<b>Appendix A</b>	<b>Atlas Input Deck File</b>	<b>97</b>
<b>Appendix B</b>	<b>Coplanar Waveguide Parameters</b>	<b>101</b>
A.1	Coplanar waveguide with infinite ground plane.....	101
A.2	Coplanar waveguide with lower ground plane .....	103
A.3	Coplanar waveguide with finite ground plane .....	104
<b>Appendix C</b>	<b>High-speed Modulator Fabrication Process Flow</b>	<b>107</b>
<b>Bibliography</b>		<b>111</b>



# *List of Figures*

Figure 1.1:	Model of electrical interconnect. ....	2
Figure 1.2:	Model of optical interconnect. ....	2
Figure 1.3:	Laser diode modulation: light output vs modulated input current. ....	5
Figure 2.1:	Optical absorption of quantum wells: (a) electron and heavy hole energy levels and wavefunctions (b) optical absorption spectrum with exciton peaks at band edge. ....	10
Figure 2.2:	Band diagrams and wavefunctions of electron and heavy hole under (a) zero field (b) finite electric field. ....	11
Figure 2.3:	Quantum well absorption change as a function of applied field for 75Å GaAs quantum well with 35Å AlAs barrier. ....	12
Figure 2.4:	Vertical cavity modulator: (a) single pass transmission modulator (b) double pass reflection modulator. ....	15
Figure 2.5:	Schematic of high speed Asymmetric Fabry-Perot modulator structure. Front and back mirrors are as depicted, with quantum wells inside. ....	16
Figure 2.6:	Analytical model of an asymmetric Fabry-Perot modulator. ....	17
Figure 2.7:	Total reflectivity of asymmetric Fabry-Perot as a function of effective back mirror reflectivity. Devices with 30% and 50% front mirror reflectivity are depicted. ....	18
Figure 2.8:	Insertion loss of asymmetric Fabry-Perot modulator as function of front mirror reflectivity $R_f$ with different absorption ratio $X$ . ....	19
Figure 2.9:	Electroabsorption and ratio change in GaAs/Al <sub>0.33</sub> Ga <sub>0.67</sub> As MQWs as a function of well width $L_z$ . ....	20
Figure 3.1:	Simulation result of modulator reflectivity vs wavelength at various biases. ....	23
Figure 3.2:	Schematic (a) cross section and (b) top view of high speed modulator structure with superimposed circuit elements. ....	24
Figure 3.3:	Schematic diagram of n intracavity contact structure. ....	27
Figure 3.4:	Exciton radius and binding energy as a function of electron concentration in a 100Å GaAs/AlGaAs quantum well. ....	30
Figure 3.5:	(a) Net charge density, (b) electric field and (c) voltage for device with 1µm intrinsic region thickness under illumination at different optical intensities. ....	33
Figure 3.6:	Characteristic impedance of probe pad and feed line. ....	36

Figure 4.1: Epitaxial structure of high speed asymmetric Fabry-Perot modulator.38

Figure 4.2: Un-normalized reflectance spectrum of the wafer structure after growth. ....39

Figure 4.3: Reflectivity of the device from the center to the edge of the wafer. ....40

Figure 4.4: Processing steps for fabricating high speed modulators. ....42

Figure 4.5: The SEM views of a device: (a) after p-contact ring and n contact etch (b) after n intracavity contact. ....43

Figure 4.6: The SEM view of (a) the completed devices and (b) close-up of a device. ....44

Figure 4.7: Structure of Benzocyclobutenes (BCB). ....45

Figure 4.8: I-V characteristics of the devices with different sizes. ....48

Figure 4.9: (a) DC modulation spectra of a typical device at various biases (b) reflectivity vs bias at 847nm. Maximum contrast is achieved when operating between 0V and 3.5V. ....49

Figure 5.1: Port variable definitions. ....52

Figure 5.2: S-parameter port variable definitions. ....52

Figure 5.3: Complete equivalent circuit model of modulator diode and pad parasitics. ....54

Figure 5.4: Open pad calibration test structure and its circuit model. ....55

Figure 5.5: Admittance of open device as a function of frequency. ....55

Figure 5.6: Pad short test structure and its circuit model. ....56

Figure 5.7: Series resistance of modulators of different sizes. ....57

Figure 5.8: Capacitance of the modulator diode. ....58

Figure 5.9:  $S_{11}$  parameter of a complete device. ....59

Figure 5.10: Schematic of experiment setup to measure high speed E-O response.61

Figure 5.11: Signal flow of (a) combined microwave networks consisting of microwave probe, MQW modulator and photodetector (b) equivalent measured two-port network. ....62

Figure 5.12: Normalized electro-optical response for a  $40\mu\text{m}\times 40\mu\text{m}$  device under different terminations. ....63

Figure 5.13:  $S_{11}$  parameter of device under different terminations. ....64

Figure 5.14: Normalized electro-optical response for devices of different sizes. ....65

Figure 6.1: Various time constants involved in the carrier sweep-out. ....68

Figure 6.2: Photocarrier density distribution at time t, when  $n_0v_i t$  carriers have accumulated on the two electrodes. ....73

Figure 6.3: Normalized electron and hole currents as a function of time. ....74

Figure 6.4:	Propagation of the photo carrier in (a) one dimensional transmission line (b) two dimensional surface with lateral resistance and vertical capacitance.....	75
Figure 6.5:	Voltage relaxation of the initial Gaussian excitation. ....	77
Figure 6.6:	Time evolution of the normalized photovoltage for different (a) diffusive recovery time $t_c$ (b) carrier transit time $\tau_e = \tau_h$ (c) electron, hole transit time $\tau_e \neq \tau_h$ .....	80
Figure 6.7:	Schematic of pump/probe setup.....	81
Figure 6.8:	Measurement result of (a) reflectivity change (b) normalized photovoltage change as function of pump-probe delay time. ....	82
Figure 6.9:	Rise time of the device as a function of bias voltage.....	83
Figure 6.10:	Fall time as a function of bias voltage. ....	84
Figure 6.11:	High speed modulator works as a high efficiency photodetector. ....	85
Figure 6.12:	Equivalent circuit model of photodetector diode and probe pad. ....	86
Figure 6.13:	P-I-N photodetector bandwidth dependence on depletion intrinsic region thickness for $10\mu\text{m} \times 10\mu\text{m}$ and $20\mu\text{m} \times 20\mu\text{m}$ devices. ....	88
Figure 6.14:	Schematic of high speed photodetector characterization setup. ....	89
Figure 6.15:	High speed photocurrent response of the $40\mu\text{m}$ device.....	90
Figure 6.16:	Photocurrent response for (a) $40\mu\text{m} \times 40\mu\text{m}$ device under different bias voltages (b) devices of different sizes.....	91
Figure B.1:	Coplanar waveguide with infinite ground plane (CPW). ....	101
Figure B.2:	Coplanar waveguide with lower ground plane. ....	103
Figure B.3:	Coplanar waveguide with finite lateral ground plane. ....	105

:

# 1

# *Introduction*

## **1.1 Optical Interconnects**

Optical interconnects, which have made great advances in recent years, are beginning to impact electronic systems. The phenomenal growth in the performance and range of applications of optical interconnects is fueled by an exponential rate of improvement in the underlying semiconductor technology. Every three years, the number of devices that can be fabricated on a chip, and more importantly the number of wire grids on a chip, quadruples. As the speed and the density of a chip increase, electrical interconnects have become the bottleneck of chip-to-chip, module-to-module and board-to-board connection due to the nature of electrical wires: larger power consumption, low bandwidth, large electromagnetic interference at dense integration and their limitation to two-dimensional integration. Optical interconnects, on the other hand, have lower power consumption, larger bandwidth, immunity to electromagnetic interference and are suitable for dense volume integration. They also promise to alleviate the bottlenecks of interconnection greatly [1][2][3].

### **1.1.1 Power consumption**

Optical interconnects will allow lower power processors to be developed. It is generally considered that the energy and volume consumed by data links will be critical factors limiting the achievable switching time of all-electronic computers. System and circuit limits are more restrictive than device limits, mainly because the electrical connections between devices do not scale to the same degree as device themselves [4]. In the electrical connection as shown in Figure 1.1, to obtain high-speed operation, very fast low impedance ( $50\Omega$ ) transmission lines are commonly used. At high frequencies, transmission lines

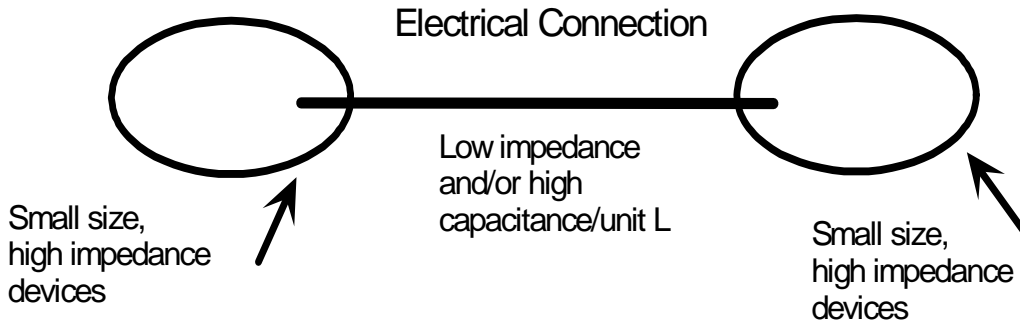


**Figure 1.1:** Model of electrical interconnect.

are superior to ordinary point-to-point wiring because of lower distortion, lower radiation and lower crosstalk. In exchange for these good properties, such low impedance and high capacitance transmission lines draw high current, therefore consume a lot of power while being charged and discharged [5]. Since the capacitance of the transmission line between source and detector increases proportionally with its length, it therefore becomes advantageous to use optical interconnects for distances in excess of a critical value.

The typical scheme of optical interconnect is shown in Figure 1.2, it consists of a transmitter and a receiver. The transmitter converts the electrical signals to optical signals and the receiver converts the optical signals into electrical signals. The transmission media can be either free space or optical fiber. Because of this conversion, the mismatch of impedance between devices and transmission lines gets solved quantum mechanically. The only power consumed is that to drive the optical transmitter of one chip and the receiver of the other. Whereas in electrical interconnects, the data comes out from a

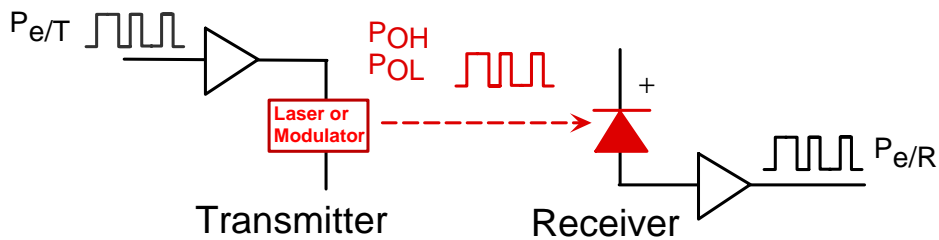


**Figure 1.2:** Model of optical interconnect.

CMOS driver pad, travels to the line driver and then to the other board. The total power consumption has contributions from all these operations, which is much higher than that projected for optical interconnects [6][7][8].

### 1.1.2 Bandwidth

An electrical wire is a low pass filter and will limit the bandwidth of data transmission. At high frequency, the current takes the path of least inductance which is primarily on the surface of transmission line, and is known as “skin effect” [9]. The skin depth, where the current density has fallen off to  $1/e$  of its maximum value is given by

$$\delta = (\pi f \mu \sigma)^{-1/2} \quad (1.1)$$

where  $\sigma$  is the conductivity of the material and  $f$  is the frequency of signal.

This will decrease the conductive cross section of wire and increase the wire resistance and attenuation. This frequency-dependent attenuation due to skin effect causes the signal pulse to spread out, and leads to inter symbol interferences (ISI) as the tails of the response to past symbols interfere with new symbols.

Optical transmission media, either free space or fiber, are very broad band, typically greater than 25THz. As a result, the optical modulation frequency is very small compared to the very high optical carrier frequency ( $10^{15}$ Hz). Therefore, there is essentially no frequency dependent loss or reflection due to impedance mismatch in optical interconnects. Broadband impedance matching is rather easy in optics by simply using anti-reflection coating whenever necessary.

### 1.1.3 Crosstalk and other advantages

An electrical wire acts as a good antenna at high frequencies, and it broadcasts its signal to adjacent wires through inductive and capacitive coupling between transmission lines. Since the crosstalk falls with increasing distance between wires, electromagnetic interference (EMI) will limit the density of electrical interconnects at high frequencies

[10]. Optical signals are inherently immune to EMI. They don't generate or detect RF signals. They have wavelength multiplexing capability and no topological constraints [11][12].

There are other advantages of optical interconnects. They offer high reliability due to the lack of physical contacts. They have no line capacitance or mutual coupling. They potentially take smaller chip area and volume, therefore "real estate" wasted on output pin bond pads and drivers can be eliminated. It may possible to perform monolithic integration of III-V compound optoelectronics with Si CMOS circuit using heteroepitaxial growth, and various wire or flip-chip bonding techniques can be used to implement dense two dimensional arrays and three dimensional volume neural networks, smart displays and high speed communication switching fabrics [10][13][14][15][16].

## 1.2 Transmitter Solutions: VCSEL vs Modulator

There are two most competitive transmitter solutions. One is the technology based on vertical cavity surface emitting lasers (VCSEL), the other is the technology based on vertical cavity multiple quantum well (MQW) modulators. They are both vertical surface devices, and compared to in-plane devices, one- and two-dimensional arrays can be easily fabricated simultaneously on the same wafer, resulting in low-cost, high performance, multichannel lightwave transmitters [17][18][19].

A VCSEL is a highly efficient device that can convert an electrical signal into an optical signal at the transmitter end. The use of a directly modulated VCSEL as optical transmitter has the advantage of simple optical system design by elimination of the requirement of an external laser source and associated optics, and this will lower the cost of the system [20]. Compared to a LED, a laser has a much larger modulation bandwidth because the carrier lifetime is greatly reduced under stimulated emission. In terms of power consumption, VCSEL links consume more power than those using modulators at low bit rates because of the threshold current of a VCSEL. However at high bit rates (>1Gbit/s), the power consumption of a VCSEL is limited by its slope efficiency and is

comparable to that of modulators [19][20]. As the VCSEL technology evolves, low threshold, high slope efficiency and high power VCSELs are very promising for two-dimensional array applications.

However VCSELs have several issues to overcome to be used in large, dense array system.

The laser threshold voltage has always been a concern in a VCSEL because of the large series resistance from the layered distributed Bragg reflection (DBR) mirrors. The large threshold voltage affects electro-optical conversion efficiency as well as the threshold power penalty. Also this large threshold voltage requires high bias voltage which is not compatible with future silicon CMOS circuits [19][21].

Under the high bit rate modulation, the turn-on jitter and delay caused by laser threshold variation and driver circuit cause inter-symbol interference (ISI). The increasing jitter and delay with higher bit rate can impose a serious limit on the system bandwidth. To decrease the jitter spread, a VCSEL is normally pre-biased to a current above threshold in the region above spontaneous emission as shown in Figure 1.3. However, this decreases the contrast ratio due to the increase of laser output in the low or “off” state. This is detri-

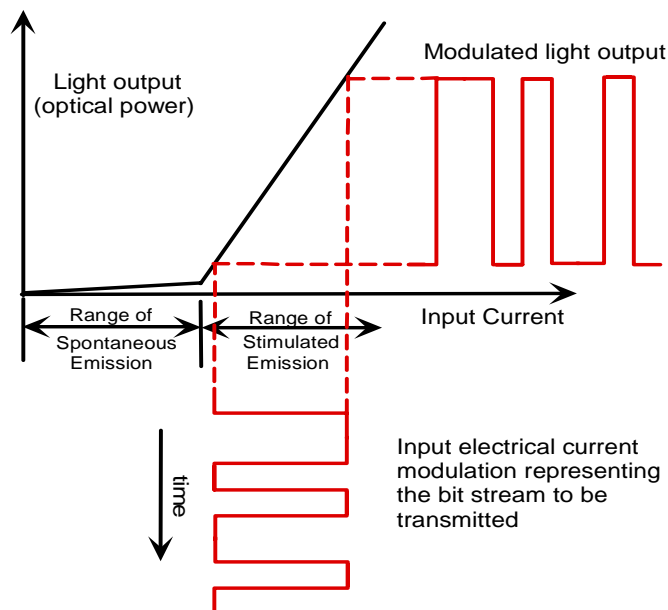


**Figure 1.3:** Laser diode modulation: laser light output vs modulated input current.

mental to the system performance. To compensate for the decrease of contrast ratio, higher modulation current will be needed which increases power dissipation [22][23].

Modulators have advantages over active light emitters in terms of timing since there is only one optical source in the system. In these systems, the clock can be distributed optically to eliminate clock skew and jitter problems that exist in large-scale systems [20].

At this stage, large array integration of VCSELs with a silicon circuit through flip-chip bonding is more challenging than for modulators due to the non-uniformity of laser arrays and the high power consumption of large arrays of emitters. Modulators already have demonstrated two dimensional integration of more than 256 devices, all of which can be operated simultaneously [12][14]. Such a large array is crucial for system applications since it avoids multiplexing signals to a high bandwidth on a small number of channels and offers greater failure tolerance through redundancy.

A modulator can also serve dual function as a high efficiency photodetector at the receiver end by using a different electronic control circuit. This has the advantage of doubling the optical I/O to a photonic layer since each optical diode can act as both a modulator and a photodetector. It can also help reduce power losses associated with providing multiple optical paths to the optoelectronic chips arising from the beam splitters and scattering [27].

As for reliability, the modulator seems more attractive because it is essentially a reverse biased diode. By contrast, the forward biased VCSEL is more sensitive to the formation of defects at the light emitting junction and shows a reduced lifetime, particularly at elevated temperature [11].

### **1.3 Other Applications**

Modulators have also found applications in the area of optical fiber telecommunications and data links. Quantum well modulators are routinely used in integrated laser-modulator structures for high speed telecommunications. Traditionally, travelling wave modulators are used at  $1.3\mu\text{m}$  or  $1.5\mu\text{m}$  where fibers have the lowest dispersion

and/or loss, because vertical cavity devices cannot compete for speed and efficiency at this long wavelength. However, very short reach (VSR) applications (<300m), such as data links of network backbone, data communications and computer interconnects, are all converging on the need for low-cost 10-Gb/s optical interconnects. Multi-channel parallel-optical interconnects using fiber ribbons provide aggregate data rates of up to 30 Gb/s in a compact, low-cost package. Since loss and dispersion in the fiber for this application are not the critical issues, 850nm, where GaAs/AlGaAs material and processing are relatively mature and cheap, becomes a good choice of wavelength.

The large power consumption, low contrast ratio and large jitter spread of directly modulated VCSEL arrays have made them impractical in real systems. Vertical cavity modulators have large contrast ratio >10dB, low insertion loss and small power consumption. Therefore, a good solution to the above problem is to use an external modulator while keeping the laser continuously operating [19].

## 1.4 Organization

The objective of this thesis is to optimize and characterize the high speed performance of vertical cavity MQW modulators for optical interconnect and communication applications. Chapter 2 provides the background on modulator fundamentals including the quantum confined Stark effect and Fabry-Perot modulators. Chapter 3 discusses design trade-offs and optimization of the device for high speed, low driving voltage operation. The high speed limitation of the device at low and high optical intensity will also be discussed. Chapter 4 discusses the fabrication and the DC measurement results of the device. In Chapter 5, high speed experimental results are presented, including equivalent circuit extraction and high speed electro-optical response. In Chapter 6, the results of carrier dynamics of the device under ultra-fast laser excitation are presented along with a demonstration and discussion of using this device as a high speed and high efficiency photodetector. Finally, Chapter 7 summarizes and discusses future work which can lead to further performance improvement for these high speed devices.



# 2

## *Background*

### 2.1 Quantum Confined Stark Effect

The quantum confined Stark effect is a fundamental phenomenon for the operation of high speed, low driving voltage electro-absorption modulators.

#### 2.1.1 Quantum well

A quantum well (QW) consists of a small bandgap semiconductor material, referred to as the well, sandwiched between larger bandgap materials, referred to as barriers. Alternating layers of small bandgap materials and large bandgap materials result in multiple quantum wells (MQW). GaAs, AlAs and  $\text{Al}_x\text{Ga}_{1-x}\text{As}$  are very attractive as quantum well materials. The lattice mismatch is very small and high quality interfaces can be produced. The bandgap increases with Al concentration. At room temperature, the bandgap of GaAs (used as the well material) is 1.424eV, and  $\text{Al}_x\text{Ga}_{1-x}\text{As}$  (used as the barrier material) is [28]:

$$E_g(x) = 1.424 + 1.247x \quad (0 \leq x \leq 0.45) \quad (2.1)$$

$$E_g(x) = 1.424 + 1.247x + 1.147(x - 0.45)^2 \quad (0.45 < x \leq 1) \quad (2.2)$$

For the direct bandgap region ( $x < 0.45$ ), the difference in the bandgap between GaAs and AlGaAs is split between conduction and valence band offset in a ratio of 65% vs 35% [29]. With the advance of growth technology, high quality thin single crystal semiconductor layers with atomic layer precision can be grown by using either molecular beam epitaxy (MBE) or metal organic chemical vapor deposition (MO-CVD).

When the well width is on the order of 10nm or less, electrons and holes confined in the wells exhibit quantum effects at room temperature. This quantum confinement results

in step-like density of states (2D) and discrete energy levels in the conduction and valence bands of the QWs, similar to the quantized energies for particles inside a one-dimensional-box. As shown in Figure 2.1(a), the ground states of the electron in the conduction band and heavy hole in the valence band are marked as  $E_{e1}$  and  $E_{hh1}$ . The envelope wave functions of the electrons and holes are sinusoidal inside the well with a tail exponentially decaying into the barrier due to the finite barrier height. A full description of such an inter-band optical transition will have to include the  $1/r$  Coulomb interaction between the electron and hole. The electron-hole pair are bound to form a hydrogenic exciton in the well within less than one hydrogenic Bohr radius ( $\sim 30\text{nm}$ ). This results in strong exciton resonance and enhancement of the optical absorption due to the increase of wave function overlap between electron and hole, near the bandgap with no applied electrical field as shown in Figure 2.1(b). In the bulk semiconductor, there is also an exciton resonance, but they are quickly broadened with electrical field and diminished due to the field ionization of excitons [30][31][32][33][34].

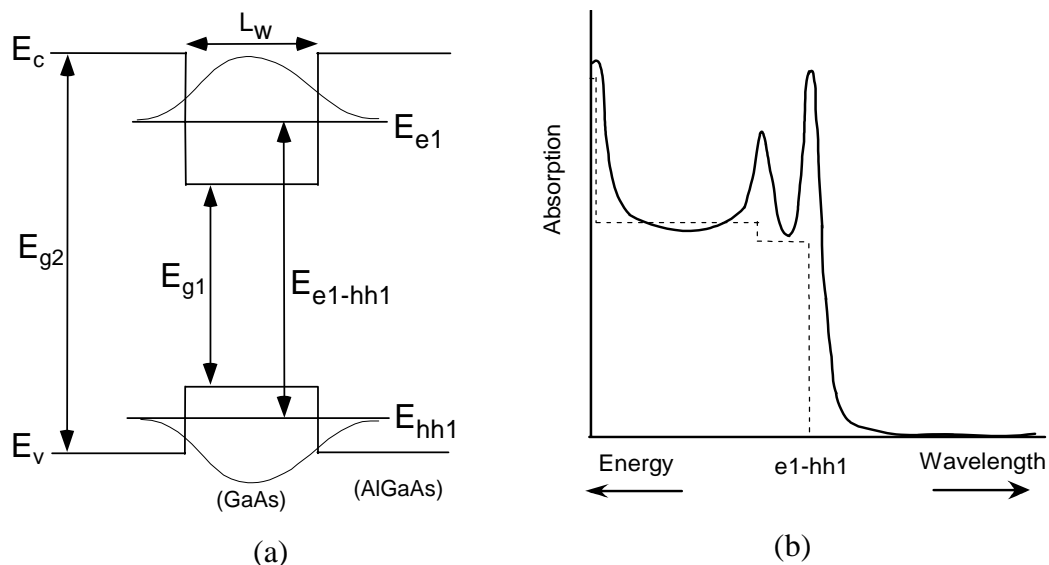


**Figure 2.1:** Optical absorption of quantum wells: (a) electron and heavy hole energy levels and wavefunctions (b) optical absorption spectrum with exciton peaks at band edge.

### 2.1.2 Quantum confined Stark effect

When an electrical field is applied to the MQW material, different electro-absorption behaviors are observed for the parallel-field vs perpendicular-field case. When the electrical field is parallel to the MQW layers, the exciton resonances are broadened with field, disappearing at fields  $\sim 10^4$  V/cm, just as those in bulk semiconductor materials. However, when the applied electrical field is perpendicular to the MQWs, the exciton peaks shift to lower energies up to 2.5 times the zero-field exciton binding energy, with the exciton resonances remaining well resolved and without ionization even at fields as high as  $\sim 10^5$  V/cm [33][34]. In this case, the excitons are not easily field ionized because of quantum confinement, which results in long tunneling lifetime out of quantum wells and strong Coulomb attraction between the electrons and holes in the very thin wells. This perpendicular-field electroabsorption in quantum well material is called the quantum confined Stark effect (QCSE). QCSE is a powerful way of changing the optical absorption properties in the quantum wells. The large shift of exciton peak results in larger and sharper absorption changes with applied electrical field at room temperature. This feature makes MQW devices favorable in achieving low insertion loss and low driving voltage.

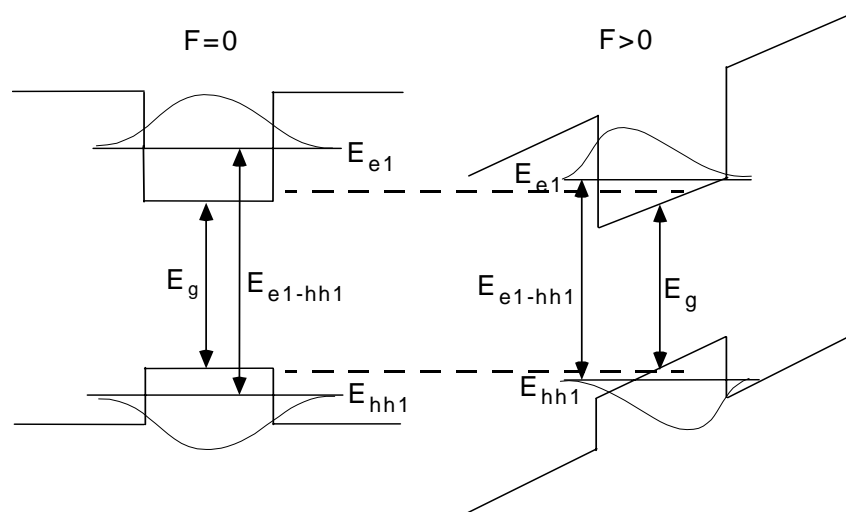


**Figure 2.2:** Band diagrams and wavefunctions of electron and heavy hole under (a) zero field (b) finite electric field.

Figure 2.2 shows the band diagrams and wavefunctions under zero and finite applied electric field. The bands are tilted as a result of the applied electrical field. This decreases both the electron and hole energy levels and thus reduces the energy separation between the two levels. In the mean time, since the electron and the hole are pushed to opposite sides of the quantum well, the spatial wave function overlap is reduced and this will decrease the exciton oscillator strength. This combination translates into an optical absorption change with applied electrical fields.

Figure 2.3 is experimental data of optical absorption change of quantum wells with 75Å GaAs wells and 35Å AlAs barriers. The exciton peaks are red shifted to longer wavelength with increasing electrical field. Because the exciton oscillator strength and lifetime are reduced, the exciton peaks are broadened at the same time with increasing field. The absorption of bulk GaAs is also shown for comparison. The significant electro-absorption changes for the quantum well material are due to the strong quantum confinement effect on electrons and holes. There are two wavelength regions where absorption modulators are commonly operated: the normally-off state modulator where operating wavelength,  $\lambda_0$ ,

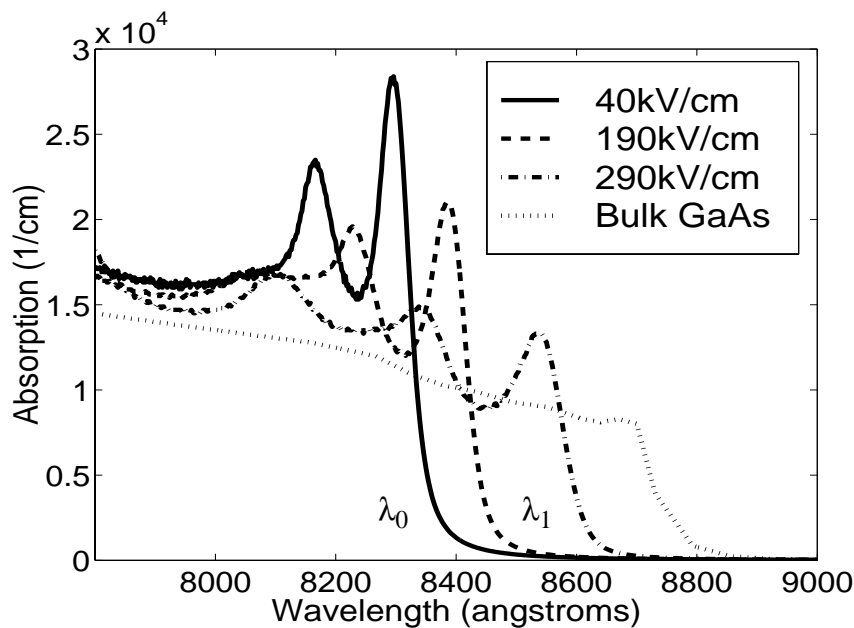


**Figure 2.3:** Quantum well absorption change as a function of applied field for 75Å GaAs quantum well with 35Å AlAs barrier.

(830nm) is at the strong absorbing exciton wavelength at zero bias and normally-on state modulator where the operating wavelength,  $\lambda_1$ , is longer than exciton wavelength at zero bias, but within the range where the exciton shifts with applied bias. Since there is a bigger residual optical absorption for  $\lambda_0$  operation, modulation contrast ratio is larger and insertion loss is smaller for  $\lambda_1$  operation. Our devices are designed to operate in the normally-on state since the insertion loss is small at zero bias.

### 2.1.3 Quantum confined Stark shift - well width dependence

To incorporate the quantum well in the device, the absorption change with applied electrical field needs to be understood. The exact solution of electron and hole subband energies and envelope wave functions, for an electron and hole pair inside a finite well in the presence of external field, can be found using the transfer matrix approach [36]. The exciton binding energy for the  $n = 1$  electron-heavy hole can be solved by the variational method [37][38]. The excitonic transition energy  $E_{ex}$  can be expressed as

$$E_{ex} = E_g + E_e + E_h - E_b \quad (2.3)$$

where  $E_g$  is the bulk bandgap energy of the quantum well material,  $E_e$  is the electron subband energy,  $E_h$  is hole subband energy and  $E_b$  is exciton binding energy.

In the presence of an electrical field, the exciton energy shift (quantum confined Stark shift) is found to be quadratic in the applied electrical field,  $F$ , and proportional to the 4th power of quantum well width  $L$  [37],

$$\Delta E_{ex} = -\frac{\pi^2 \Omega^2 m^* e^2 F^2 L^4}{2 h^2} \quad (2.4)$$

where  $\Omega$  is a constant determined by the barrier height,  $m^*$  is the electron effective mass,  $e$  is the electron charge and  $h$  is the Planck constant.

In order to enhance the absorption change and reduce the operating voltage, the well width, the barrier height and the barrier width have to be optimized. It is theoretically pre-

dicted and experimentally verified that the largest quantum confined Stark effect can be achieved with wider wells with a smaller driving voltage. However since the exciton oscillator strength is reduced with larger wells, more quantum wells are needed to achieve the same absorption change. This results in an increased intrinsic region thickness, therefore a larger driving voltage. There is an optimum quantum well width for high absorption change. Theoretical and experimental data show that the optimum well width is about  $75\text{\AA}$  for an  $\text{Al}_{0.33}\text{Ga}_{0.67}\text{As}$  barrier [39][40]. When the well width is narrower than the optimal well width, the Stark shift is small and a large electric field has to be applied to shift the exciton, resulting in a broadening of the exciton spectrum and smaller absorption change. When the well width is larger than the optimal width, the oscillator strength decreases under electrical field due to greater separation and reduced overlap of the electron and hole wavefunctions, which results in a smaller absorption change.

## 2.2 Asymmetric Fabry-Perot modulator

### 2.2.1 Modulator configuration

There are two basic configurations to make a vertical cavity modulator using quantum wells: a transmission modulator or a reflection modulator. Electrically, both are formed from a p-i-n diode with quantum wells in the intrinsic region so that the optical absorption of quantum well can be changed with a reverse bias voltage applied on the p-i-n diode.

In the transmission modulator, as shown in Figure 2.4(a), the optical beam passing through the cavity is modulated by the absorption change of the quantum wells. To minimize any optical loss associated with the GaAs substrate, the device either operates at a longer wavelength than that associated with the bandgap of GaAs and thus the substrate is transparent, or the substrate is locally removed. The simpler structure of transmission modulator may make them easier to integrate into certain systems because they do not require highly reflective mirrors. They are thus easier to fabricate and have a larger optical bandwidth because they don't rely on Fabry-Perot resonant effects. Therefore they are

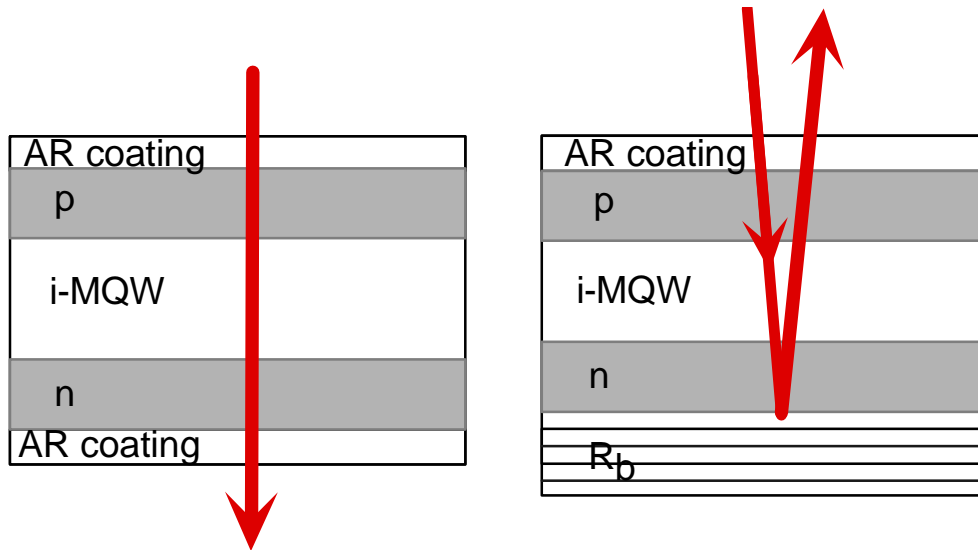


**Figure 2.4:** Vertical cavity modulator: (a) single pass transmission modulator  
(b) double pass reflection modulator.

more flexible, especially when we want to implement larger arrays. However, since the optical beam is only making a single pass through the active absorption region, it has a limited contrast ratio. Increasing the active region thickness will increase the contrast ratio, but it would mean higher operating voltage in order to achieve the same electric field in the quantum well region, and higher insertion loss due to the accumulated residual optical absorption.

In the reflection modulator shown in Figure 2.4(b), the reflection of the incoming light is modulated by the absorption change in the quantum wells. The p-i-n diode is integrated with an optical back mirror, which effectively increases the optical path by a factor of two without increasing the operating voltage. Since the light enters and leaves the same side of device, the substrate is out of the optical path. It is relatively easier to integrate the device with an electronic circuit, and the substrate does not need to be removed.

### 2.2.2 Asymmetric Fabry-Perot reflection modulator

To further increase the contrast ratio, an asymmetric Fabry-Perot resonant optical cavity can be implemented as shown in Figure 2.5. It consists of both top and bottom mirrors

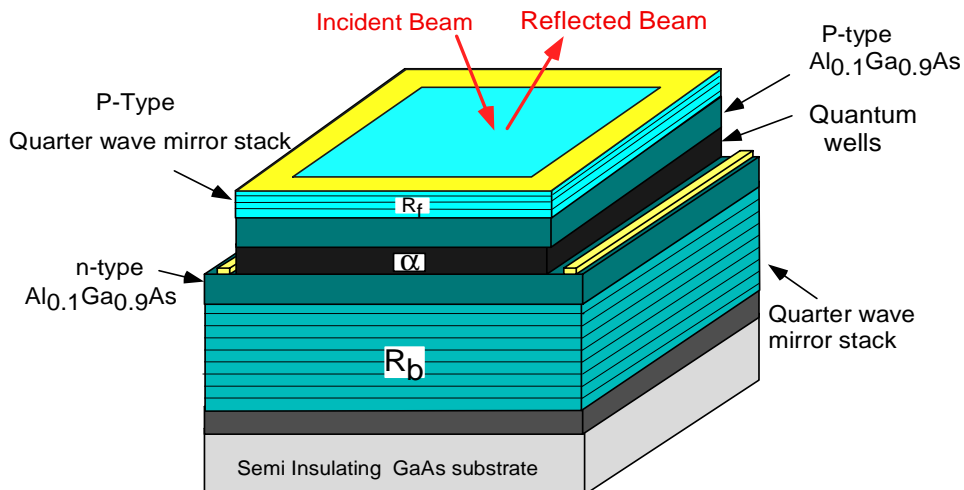


**Figure 2.5:** Schematic of high speed Asymmetric Fabry-Perot modulator structure. Front and back mirrors are as depicted, with quantum wells inside.

with non-equal reflectivities. The top mirror reflectivity is made smaller than that of the bottom mirror, so that the absorption of quantum wells balances the Fabry-Perot cavity and nulls the overall reflection of the device at a certain bias voltage. This is known as an asymmetric Fabry-Perot modulator (AFPM). In practice, the top and bottom mirrors are made of alternating quarter wave stacks of narrow and wide bandgap material capable of providing the desired refractive index contrast, such as  $\text{Al}_{0.35}\text{Ga}_{0.65}\text{As}$  (index  $\sim 3.393$  @847nm) and  $\text{AlAs}$  (index  $\sim 2.993$  @847nm). These mirrors are also known as distributed Bragg reflection (DBR) mirrors.

A schematic cross sectional view of an AFPM is shown in Figure 2.6. Quantum wells with absorption coefficient  $\alpha$  are placed in an optical cavity of thickness  $L$ . The electric field reflection coefficient of the top and bottom mirrors are  $r_f$  and  $r_b$  respectively. The total reflectivity of the incident wave is the sum of the reflection of the front mirror and back mirror after a round trip in the cavity and can be expressed as [41][42]:

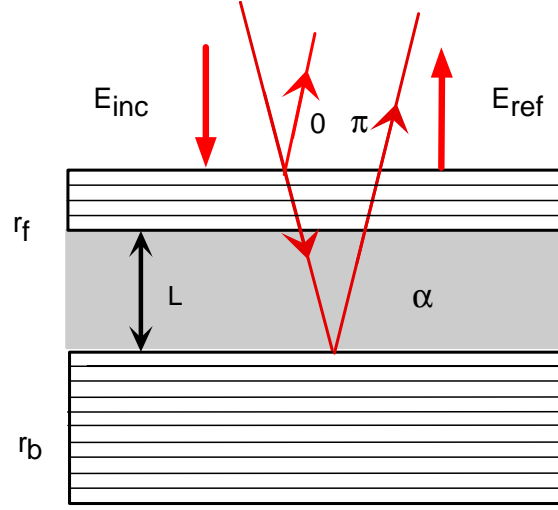


**Figure 2.6:** Analytical model of an asymmetric Fabry-Perot modulator.

$$R = \frac{r_f^2 r_{beff}^2 - 2r_f r_{beff} \cos(2\beta L)}{1 + r_f^2 r_{beff}^2 - 2r_f r_{beff} \cos(2\beta L)} \quad (2.5)$$

where  $\beta$  is the propagation constant inside the optical cavity and  $r_{beff}$  is the effective back mirror reflectivity ( $r_{beff} = r_b e^{-\alpha L}$ ).

At the Fabry-Perot resonant wavelengths which occur when  $\beta L = m\pi$  ( $m=1,2,3\dots$ ), or equivalently when the cavity length is an integral number of half wavelengths, the total reflectivity drops to a minimum value  $R_{tot}$ , which is

$$R_{tot} = \left[ \frac{r_f - r_{beff}}{1 - r_f r_{beff}} \right]^2 \quad (2.6)$$

We plot total reflectivity  $R_{tot}$  as a function of the effective back mirror reflectivity  $R_{beff}$  for different values of front mirror reflectivity  $R_f$  in Figure 2.7. The reflectivity of the device drops from the high reflective state, with reflectivity  $R_{on}$ , to the low reflective state, with reflectivity  $R_{off}$ , as the absorption of quantum wells increases from  $\alpha_{min}$  to  $\alpha_{max}$ . The increased optical field at the optical resonant wavelength effectively enlarges the optical interaction length. Therefore, fewer quantum wells are needed to absorb the same fraction

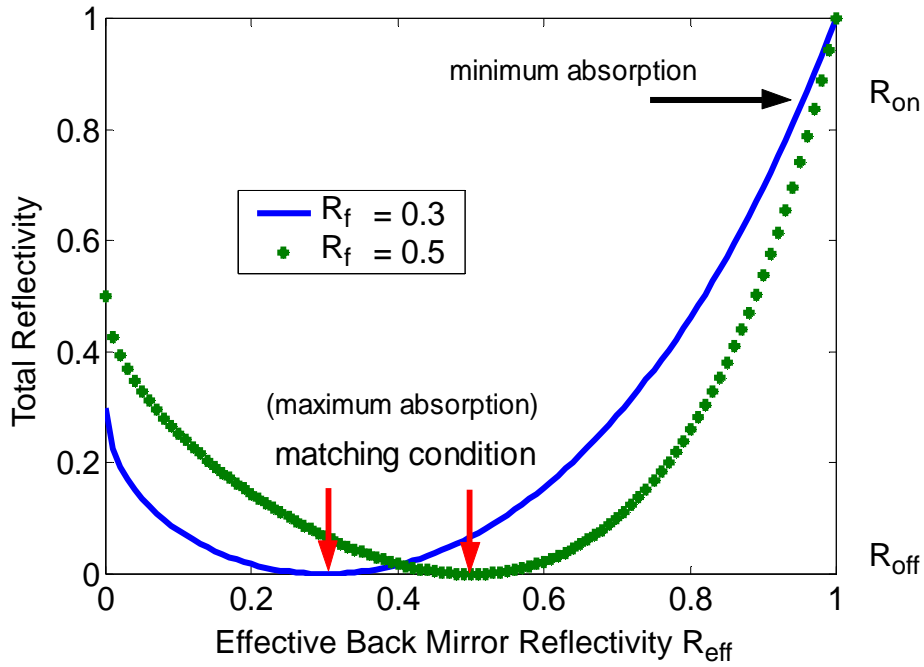


**Figure 2.7:** Total reflectivity of asymmetric Fabry-Perot as a function of effective back mirror reflectivity. Devices with 30% and 50% front mirror reflectivity are depicted.

of light, and the modulator can therefore operate at a lower voltage. Zero reflection is achieved when the front mirror reflectivity equals that of the effective back mirror reflectivity, which is

$$r_f = r_b e^{-\alpha_{max}L} \quad (2.7)$$

In this case, the round trip propagation of a wave inside optical cavity, which equals an integer number of  $1/2 \lambda$ , results in a phase matching between the two reflected waves. But the reflection from the front mirror is going from low index to high index material which produces  $\pi$  phase shift while reflection from the back mirror is going from high index to low index material, and thus produces a 0 phase shift. Therefore, the reflectance from the front mirror and back mirror adds destructively and the total reflectance can approach perfect 0.

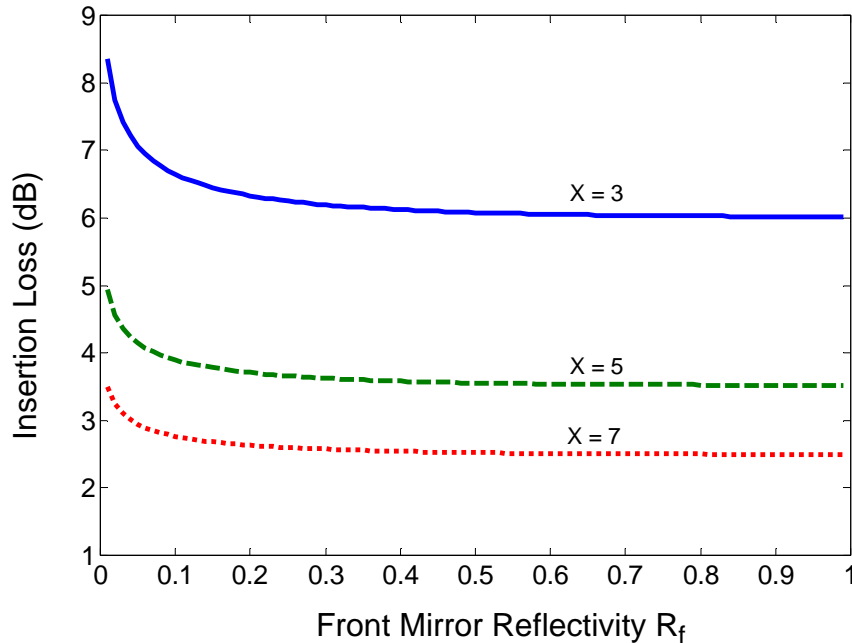


**Figure 2.8:** Insertion loss of asymmetric Fabry-Perot modulator as function of front mirror reflectivity  $R_f$  with different absorption ratio  $X$ .

The insertion loss (IL), which is defined as  $-10\log(R_{on})$ , determines the fan-out of such a modulator in a cascaded system. Figure 2.8 plots the insertion loss of the device as a function of front mirror reflectivity for different values of absorption ratio,  $X = \alpha_{max}/\alpha_{min}$ . The insertion loss increases as the front mirror reflectivity decreases, however the effect is rather small since the nominal reflectivity from GaAs is  $\sim 30\%$ . This is because in the on state, the absorption of the quantum wells is small and the reflectivity is dominated by the back mirror reflection. The insertion loss decreases as the absorption ratio,  $X$ , increases. As one can imagine, if we have a totally transparent quantum well ( $\alpha_{min}=0$ ) in the on state, the insertion loss will be 0dB. Practically, the achievable  $X$ , for  $\text{Al}_{0.33}\text{Ga}_{0.67}\text{As}$  barriers, peaks with a maximum of 6 occurring at a quantum well width around  $50\text{\AA}$  as shown in Figure 2.9 [39]. When the well width is narrower than  $50\text{\AA}$ , the ground state energy is high and the evanescent wave penetrates into the quantum barrier more. This results in less wavefunction overlap and exciton spectrum has smaller absorption change. When the well width is larger than  $50\text{\AA}$ , the oscillator strength decreases with wider well width under

electric field due to reduced quantum confinement, which results in a smaller absorption change.

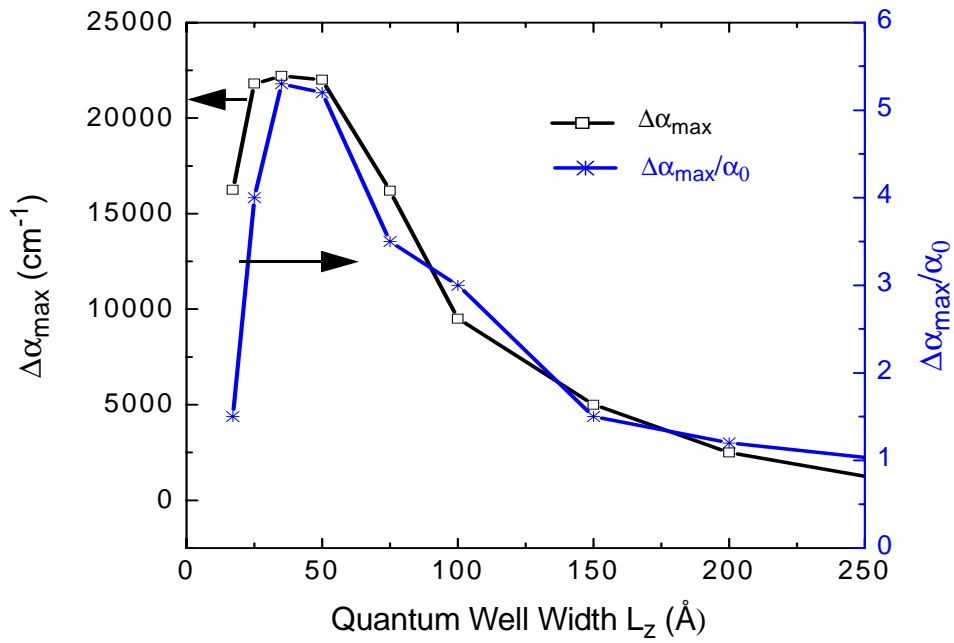


**Figure 2.9:** Electroabsorption and ratio change in GaAs/Al<sub>0.33</sub>Ga<sub>0.67</sub>As MQWs as a function of well width  $L_z$  [39].

# 3

## *Device Design for High Speed Operation*

For most system applications, there are specific performance criteria for modulators, such as high contrast ratio [42][43], small insertion loss [42][44], low driving voltage [45][46][47], large  $f_{3dB}$  bandwidth [48][49][50][51], and wide optical bandwidth [46]. Based on these requirements, design trade-offs and different optimizations can be proposed. None of the previous work on modulators considered the optimization of both high speed and low driving voltage which are key performance parameters in practical applications. In the previous chapter, the optimization of devices for high contrast ratio and small insertion loss was discussed. This chapter will focus on the device design and optimization for high speed and low driving voltage operation.

### **3.1 Low Driving Voltage and Large Absorption Change**

At high speed, low driving voltages (both DC bias and RF voltage swing) across the device are imperative for the system power budget. The ideal driving voltages of the device should be CMOS compatible to eliminate the need for an additional power supply and complex expensive RF microwave amplifiers.

The driving voltage of the device is a function of the intrinsic region thickness, quantum confined Stark shift and the spacing between the exciton absorption peak resonance and Fabry-Perot resonant dip. In order to enhance the absorption change and reduce the operating voltage, it is necessary to optimize the quantum well width, the barrier height and the barrier width. To maximize the absorption change, smaller wells are preferable

since their oscillator strengths remain larger at the operating voltage. From our previous analysis in Chapter 2, the Stark shift is proportional to the fourth power of quantum well width, therefore larger wells require smaller electrical fields for the same amount of Stark shift. It is theoretically predicted and experimentally verified that a larger quantum confined Stark effect can be achieved with wider wells with a smaller electric field. However, since the exciton oscillator strength is reduced with larger wells, more quantum wells are needed to balance the front mirror, and this will increase the intrinsic region thickness, therefore increasing driving voltage. There is thus an optimum quantum well width for large absorption change. Theoretical and experimental data show that the optimum well width is about  $75\text{\AA}$  for  $\text{Al}_{0.33}\text{Ga}_{0.67}\text{As}$  barrier [39][40]. When the well width is narrower than this optimal width, the Stark shift is small and a large electric field has to be applied to shift the exciton, resulting in a broadening of the exciton spectrum and smaller absorption change. When the well width is larger than the optimal width, the oscillator strength decreases under the electrical field due to the reduced quantum confinement, which results in a smaller absorption change. From Figure 2.9, absorption change per well,  $\Delta\alpha_{max}$ , is a strongly peaked function with a maximum of 0.012 occurring near  $L_z = 75\text{\AA}$  [40]. We chose a quantum well width of  $75\text{\AA}$  so that the fewest number of quantum wells are needed in the intrinsic region to achieve the desired absorption change.

As for the spacing between exciton and Fabry-Perot dip, smaller spacing between these two will result in a smaller driving voltage. However, as the exciton peak is put closer to the Fabry-Perot resonance, the insertion loss is increasing due to the increasing residual optical absorption below exciton resonance. Therefore, the device performance is optimum when it is operating at a electric field where the absorption change,  $\Delta\alpha$ , peaks. The Fabry-Perot peak is put at the same wavelength as the exciton peak at the operating electric field. For  $75\text{\AA}$  GaAs wells with  $\text{Al}_{0.3}\text{Ga}_{0.7}\text{As}$  barriers, this wavelength is around 845nm [39][40]. We designed our Fabry-Perot optical cavity at the wavelength of 845nm, while the exciton peak is at 830nm for zero field. The spacing between these two is opti-

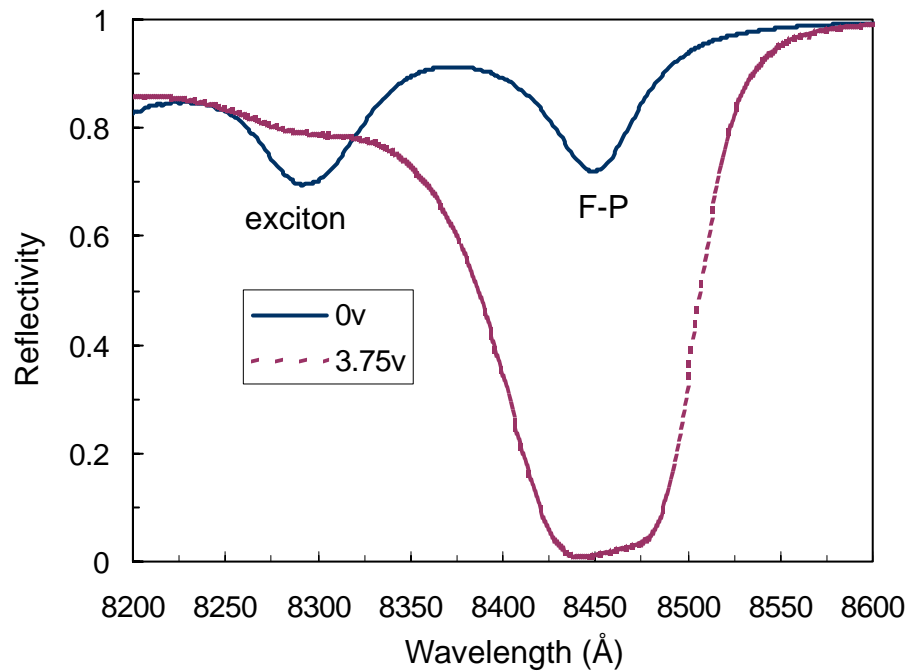


**Figure 3.1:** Simulation result of modulator reflectivity vs wavelength at various biases.

mized at about 15nm. Figure 3.1 shows the simulation results of modulation spectra of a typical AFPM for different bias voltages.

## 3.2 High Speed Operation

The quantum confined Stark effect is a very fast process, limited only by how fast the wave functions respond to the external electric fields. Therefore at low optical intensity, the high speed limitation of the device is its RC time constant, which is due to how fast the device can be charged and discharged, not carrier transit times. However at high optical intensity, the large number of photo-generated carriers in the intrinsic region could limit the device's performance either by photovoltage screening, exciton saturation or thermal effect.

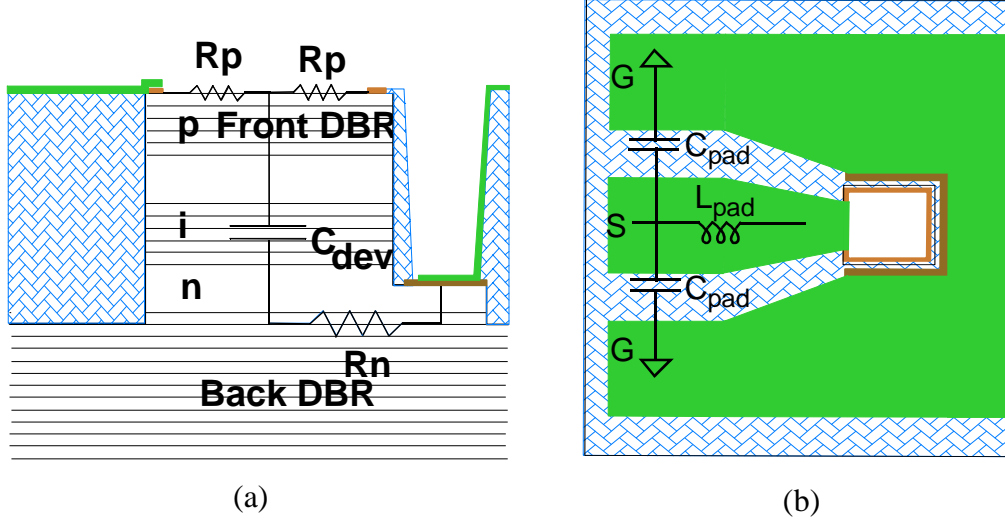


**Figure 3.2:** Schematic (a) cross section and (b) top view of high speed modulator structure with superimposed circuit elements.

### 3.2.1 Low optical intensity - RC limited

At low optical intensity, the device is RC limited. Figure 3.2 is a schematic cross section and top view of a high speed modulator integrated with coplanar microwave probe pads. The modulator itself is a reverse biased p-i-n diode with series resistance  $R_s$  and capacitance  $C_{dev}$ . The probe pad has capacitance  $C_{pad}$  and inductance  $L_{pad}$  as shown in the superimposed equivalent circuit elements. Since  $j\omega L_{pad}$  is small compared to  $1/j\omega C_{pad}$  in the frequency range of operation (as high as 20GHz), its influence on the modulation bandwidth is negligible. The  $f_{3dB}$  bandwidth can be found using open circuit model [53], which is:

$$f_{3dB} = \frac{1}{2\pi[C_{dev}(R_s + Z_0) + C_{pad}Z_0]} \quad (3.1)$$

where  $R_s = R_p + R_n$ , the series resistance of the modulator diode from p and n sides.  $Z_0$  is the output impedance of the driver. In order to increase the modulation bandwidth, it is imperative to minimize the electrical resistance and capacitance of the device.

### 3.2.1.1 Series resistance $R_s$

The Fabry-Perot cavity is formed by molecular beam epitaxial (MBE) growth where the active quantum well region is sandwiched between two DBR mirror stacks. Due to the heterojunctions, DBR mirrors provides index contrast and high optical reflectivity. However DBR mirrors also have a larger series resistance than bulk material due to the heterojunction carrier transport. Intracavity contact layers are commonly used to reduce the series resistance. However, since the intracavity contact layer is embedded in the optical cavity where the optical field is strong, this will cause free carrier absorption, especially for p-type mirrors [54]. Different structures are used for p-type and n-type contacts in the high speed devices.

Since the holes have a relatively lower mobility, an intracavity p-type contact layer thicker than  $1\mu\text{m}$  is needed to have small lateral resistance. Such thick highly p-type doped material will cause large free-carrier absorption. Therefore, p-type layers are not suitable for intracavity contact. To minimize the p-type mirror resistance, yet still maintain high optical reflectivity, different bandgap engineering techniques are used in VCSEL fabrication to flatten the valence band offset. These include linear, parabolic and uniparabolic digital alloy grading [55][56][57], using different alloys at each GaAs/AlGaAs heterojunction [58]. However, such profiles are rather difficult to implement with the MBE growth technique. The continuous grading from binary GaAs to  $\text{Ga}_x\text{Al}_{1-x}\text{As}$  composition was not possible by MBE without many shutter openings and closings, which cause excessive wear and damage to the MBE machine after many pairs of mirror growth, so alternate structure were considered.

Another approach to lower the p-type mirror resistance is to increase the doping, which will narrow the potential spike and carriers can simply tunnel through across the junctions [56][59]. However, the high free-carrier density will cause higher free-carrier absorption losses in the mirror and deteriorate the performance of DBR mirrors. This is a critical issue for VCSELs where a large number of mirror pairs are needed to approach almost unity reflectivity. However, for modulators, only two pairs of highly doped mirror

layers are needed to achieve a reflectivity of about 50% to form a Fabry-Perot cavity. Doping concentration as high as  $1.8 \times 10^{19} \text{cm}^{-3}$  was used in the last  $40 \text{\AA}$  region where the metal contact is to reduce the p-type resistance. This is easier to grow using MBE compared to the complex bandgap engineering described above. Since this high p-type doping layer is very thin, the optical absorption loss is negligible.

For n-type layer, since electrons have higher mobility and lower free-carrier absorption, a simple n-type layer is suitable for making intracavity contacts. To get a better contact,  $\text{Al}_{0.1}\text{Ga}_{0.9}\text{As}$  was used as the intracavity contact layer. Since the n-type dopant, Si, has a larger diffusion coefficient and lower solubility in  $\text{Al}_x\text{Ga}_{1-x}\text{As}$  than in GaAs, the doping efficiency of Si in  $\text{Al}_x\text{Ga}_{1-x}\text{As}$  decreases with higher aluminum concentration [60]. Decreasing the aluminum concentration in the  $\text{Al}_x\text{Ga}_{1-x}\text{As}$  contact layer will increase the Si doping efficiency, therefore increasing conductivity. However, the heavy doping in the material causes bandgap shrinkage, and lower aluminum concentration  $\text{Al}_x\text{Ga}_{1-x}\text{As}$  might become optically opaque at the operating wavelength and increase the associated optical loss. For  $\text{Al}_{0.1}\text{Ga}_{0.9}\text{As}$ , the silicon doping efficiency is high enough, yet the material is still optically transparent at the wavelength where the device is operating. Since the contact layer  $\text{Al}_{0.1}\text{Ga}_{0.9}\text{As}$  is heavily doped and will lead to some free-carrier absorption, we want to use the thinnest layer possible. On the other hand, the lateral ohmic loss is less if a thicker contact layer can be used. In order to have good lateral conductivity, the contact layer thickness needs to be at least  $5\lambda/4$  ( $\sim 0.384 \mu\text{m}$ ) for a GaAs contact layer [59] and  $1 \mu\text{m}$  for an AlAs contact layer [61]. A  $0.5 \mu\text{m}$  thick  $\text{Al}_{0.1}\text{Ga}_{0.9}\text{As}$  was chosen as intracavity contact layer for our device. The doping level was  $1.9 \times 10^{18} \text{cm}^{-3}$  for the first  $0.25 \mu\text{m}$  near the active quantum well region and this was increased to a relatively high doping of  $4.1 \times 10^{18} \text{cm}^{-3}$  for the last  $0.25 \mu\text{m}$ . An annular metal contact is made at the higher doping contact layer to minimize the contact resistance as shown in Figure 3.3.

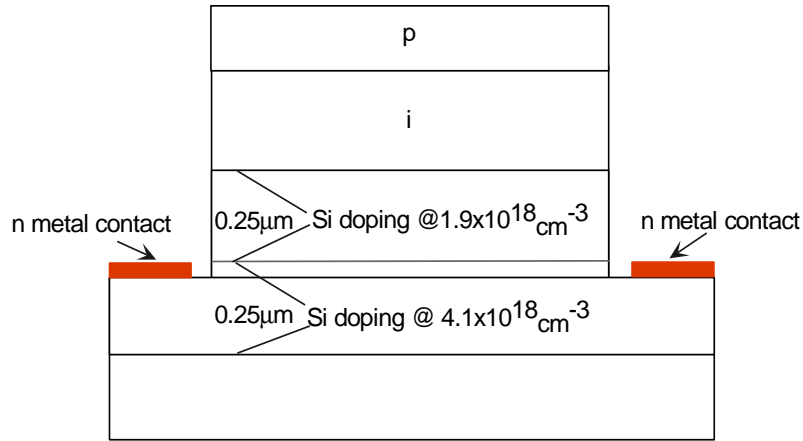


**Figure 3.3:** Schematic diagram of n intracavity contact structure.

### 3.2.1.2 Modulator capacitance $C_{dev}$ and probe pad capacitance $C_{pad}$

The capacitance of the modulator diode itself can be modeled as a parallel plate capacitor as:

$$C_{dev} = \frac{\epsilon A}{d} \quad (3.2)$$

where  $A$  is the area of modulator p-i-n diode,  $d$  is the intrinsic region thickness and  $\epsilon$  is the dielectric constant.

A thicker intrinsic region thickness,  $d$ , will reduce the modulator diode capacitance, therefore increase the device modulation bandwidth. However it is not desirable to have a very thick intrinsic region since the operating voltage is proportional to the intrinsic region thickness. There is thus a trade-off between driving voltage and modulation bandwidth. However by shrinking the device in the lateral dimension, the diode capacitance can be reduced. Devices of different sizes ranging from  $100\mu\text{m} \times 100\mu\text{m}$  to as small as  $10\mu\text{m} \times 10\mu\text{m}$  were designed and fabricated; the physical limit of lateral dimension will be discussed in Chapter 5. As we shall discover, there is a physical limit in shrinking the device capacitance as the fringe capacitance will eventually dominate.

To minimize parasitic capacitance between the probe pad and the conducting substrate, a semi-insulating substrate is used and coplanar probe pads were placed on thick low dielectric constant material, photo benzocyclobutene (BCB), to further reduce the probe pad parasitic capacitance.

### 3.2.2 High optical intensity

At high optical intensity, the performance of the device is not only limited by the device RC time constant, but is also limited by the large number of photo-generated carriers which cause exciton saturation, photovoltage screening, and/or thermal effects.

#### 3.2.2.1 Exciton saturation

At high optical intensities, the large number of photo-generated electrons and holes will cause exciton saturation and broaden or even inhibit the QCSE shift entirely. There are several mechanisms that cause this nonlinearity. They are:

**Phase-space filling:** The main physics behind this mechanism is a so-called “many body” effect. The electrons and holes are Fermions and each can occupy only a single quantum state due to the Pauli exclusion principle. As the number of photo-excited carriers increase, they start filling all available states from the bottom of the band, so that the lowest energy states are occupied first. The exciton resonance loses oscillator strength, both because of the occupation of states out of which the excitons are constructed and because of the loss of e-h correlation (the excitons are becoming larger) due to the phase-space filling process [62][63].

Phase-space filling induced exciton saturation is essentially due to the electrons present in the wells rather than to the holes. This is mainly due to the fact that the density of electronic states is significantly smaller than that of hole states. For a given carrier, the density of states close to the subband edge is proportional to its effective mass in the plane of the quantum wells, and holes have a much larger effective mass than electrons. Also, since in a quantum well, the k-space only has two dimension, one less than that of bulk

semiconductor (3D), it takes fewer carriers to fill the available states. Therefore, phase-space filling induced exciton saturation is more severe in quantum wells than for bulk material.

**Bandgap renormalization:** As the number of electrons and holes increases, the bandgap shrinks or renormalizes due to the Coulomb interaction among the laser excited carriers. The bandgap shrinks as [35]:

$$\Delta E_g = E_g' - E_g = -3 \cdot (Na_0^2)^{1/3} E_b \quad (3.3)$$

where  $N$  is the 2D e-h pair density,  $a_0$  is Bohr radius and  $E_b$  is the exciton binding energy. The bandgap narrowing exhibits the same characteristic  $N^{1/3}$  as a bulk semiconductor. It leads to an increasing absorption in the spectral region below the exciton resonance and a decreasing absorption in the exciton resonance due to the loss of oscillator strength.

**Plasma screening:** One of the consequences of the interaction among these photo-excited carriers is that they screen the Coulomb interaction among the carriers in the same band as well as between the electrons and holes in different bands. They reduce the range of the Coulomb potential of a charge in the presence of other charges. The screened potential is

$$V(q; z_e, z_h) = \frac{-e^2}{2\pi\epsilon r} e^{-q|z_e - z_h|} \frac{1}{q\epsilon(q)} \quad (3.4)$$

rather than the Coulomb potential,  $e^2/r$  and  $q\epsilon(q)$  strongly influences the potential behavior as the carrier concentration increases. Figure 3.4 plots the exciton radius and binding energy as a function of carrier density. The exciton radius increases and the binding energy decreases with increasing background carrier density. The exciton essentially disappears when the carrier concentration is greater than  $3 \times 10^{11} \text{ cm}^{-2}$ . The increasing number of carriers increase the Bohr radius and decrease the exciton binding energy [30].

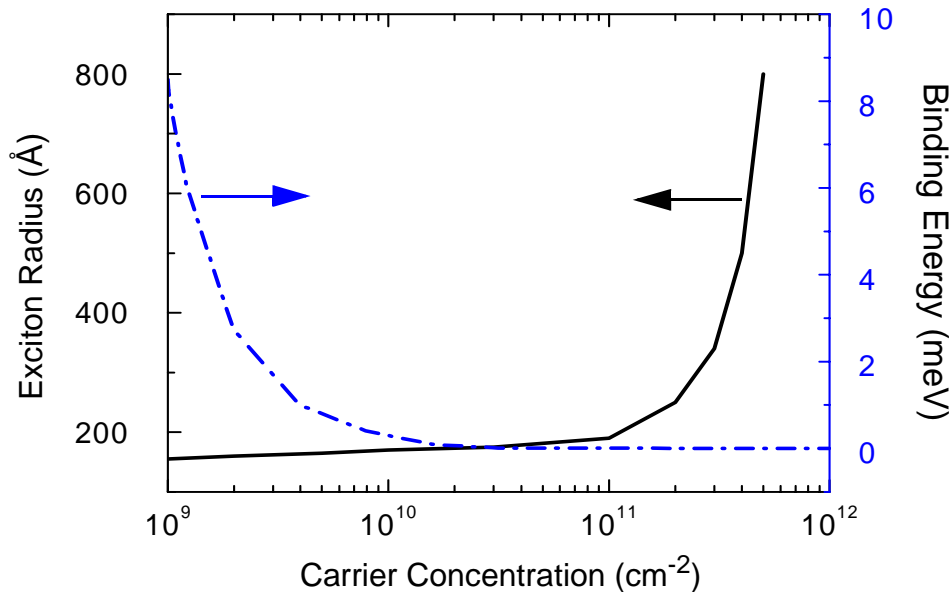


**Figure 3.4:** Exciton radius and binding energy as a function of electron concentration in a 100Å GaAs/AlGaAs quantum well [30].

The reduction of exciton binding energy blue shifts the exciton resonance and it decreases the oscillator strength at the original frequency, though the blue shift is essentially compensated by the bandgap renormalization.

**Electric field screening:** Since the sweep-out times of electrons and holes are different, space charge builds up inside the quantum well. These charges screen the applied electric field, which in turn alters the absorption change through the QCSE. The charges also change the gradient of the electrical field distribution inside the wells, and therefore cause exciton broadening due to a non-uniform electrical field. Normally, this effect is governed by the carrier with the longest escape time.

Despite the different mechanisms that cause exciton saturation, it is found that the absorption spectrum changes do not depend significantly on the excitation wavelength or on its pulse duration. These changes depend primarily only on the density and temperature of the photo-excited e-h pairs. The absorption change as a function of optical intensity is:

$$\alpha = \frac{\alpha_0}{1 + |I_p|^2 / |I_s|^2} \quad (3.5)$$

where  $\alpha_0$  is the optical absorption at low optical intensity and  $I_s$  is the exciton saturation intensity, which is [64]:

$$I_s = \frac{h\omega N_s}{\alpha_0(L_w + L_b)} \frac{m_e + m_h}{m_e \tau_e + m_h \tau_h} \quad (3.6)$$

Exciton saturation intensity,  $I_s$ , strongly depends on the carrier sweep-out time  $\tau_e$  and  $\tau_h$  in the quantum well region. Therefore it has the following dependences, just as the carrier sweep-out time:

- (1)  $I_s$  increases with applied field, F.
- (2)  $I_s$  decreases with well thickness,  $L_w$  [39].
- (3)  $I_s$  decreases with the barrier height and thickness,  $L_b$ .

There is a detail discussion of carrier transit time in Section 6.1. To minimize the carrier sweep-out time, the barrier height and width were reduced to a minimum yet still maintaining enough exciton oscillator strength for adequate QCSE (barrier: 45Å Al<sub>0.35</sub>Ga<sub>0.65</sub>As). Since the barrier has finite height, there is some coupling between neighboring wells for 45Å barrier width. The coupling of the quantum wells will form miniband and broaden the exciton linewidth. However, the linewidth broadening caused by miniband is rather small since the dominant sources of linewidth broadening are longitudinal optical (LO) phonons, interface roughness and alloy disorder in the quantum well region [40].

### 3.2.2.2 Photovoltage screening

At high optical intensity, the large number of photogenerated carriers in the intrinsic region causes an electrical field non-uniformity. Different quantum wells in the intrinsic region will experience different local electric fields. The carrier, electric field and voltage

distribution in the intrinsic absorption region under laser illumination can be solved using commercial CAD software ATLAS [61] or PROPHET [65]. These simulations don't include the quantum effects (carrier absorption and mobility), and we need to scale the illumination power according to the total photocurrent generated to better reflect the absorption and mobility difference of carriers in bulk GaAs and quantum well material. Figure 3.5(a) is the simulation results of the carrier (hole-electron) distribution inside the 1 $\mu$ m intrinsic region with -3V bias voltage under constant laser illumination using ATLAS. The corresponding electric field in the intrinsic region for different laser intensities is shown in Figure 3.5(b). Compared to the uniform electric field with no laser illumination, the electric field redistributes corresponding to the carrier density in the intrinsic region which can be quite severe at high optical intensities. Here we assume the absorption is the same across the intrinsic region. If we take into account the quantum confined effect, the uniformity will be even worse. The simulation structure and ATLAS input file are given in Appendix A.

The exciton shift due to QCSE is quadratic to the electric field, the absorption change to the first order is proportional to the local electrical field if the switching voltage is small. The total reflectivity signal is then determined by the effective voltage across the intrinsic region, which is determined by the integral of the electric field:

$$R = \left[ \frac{r_f - r_b e^{-\int_0^L \alpha_0 E(l) dl}}{1 - r_f r_b e^{-\int_0^L \alpha_0 E(l) dl}} \right]^2 = \left[ \frac{r_f - r_b e^{-\alpha_0 V}}{1 - r_f r_b e^{-\alpha_0 V}} \right]^2 \quad (3.7)$$

If the total voltage drop across the intrinsic region remains the same despite different electrical field distribution, we will have the same reflected signal from the device. Figure 3.5(c) shows the voltage across the intrinsic region as a function of n-type contact layer thickness for different optical intensities. The effective voltage across the intrinsic region decreases, due to the resistivity drop of intrinsic region, with increasing optical intensities

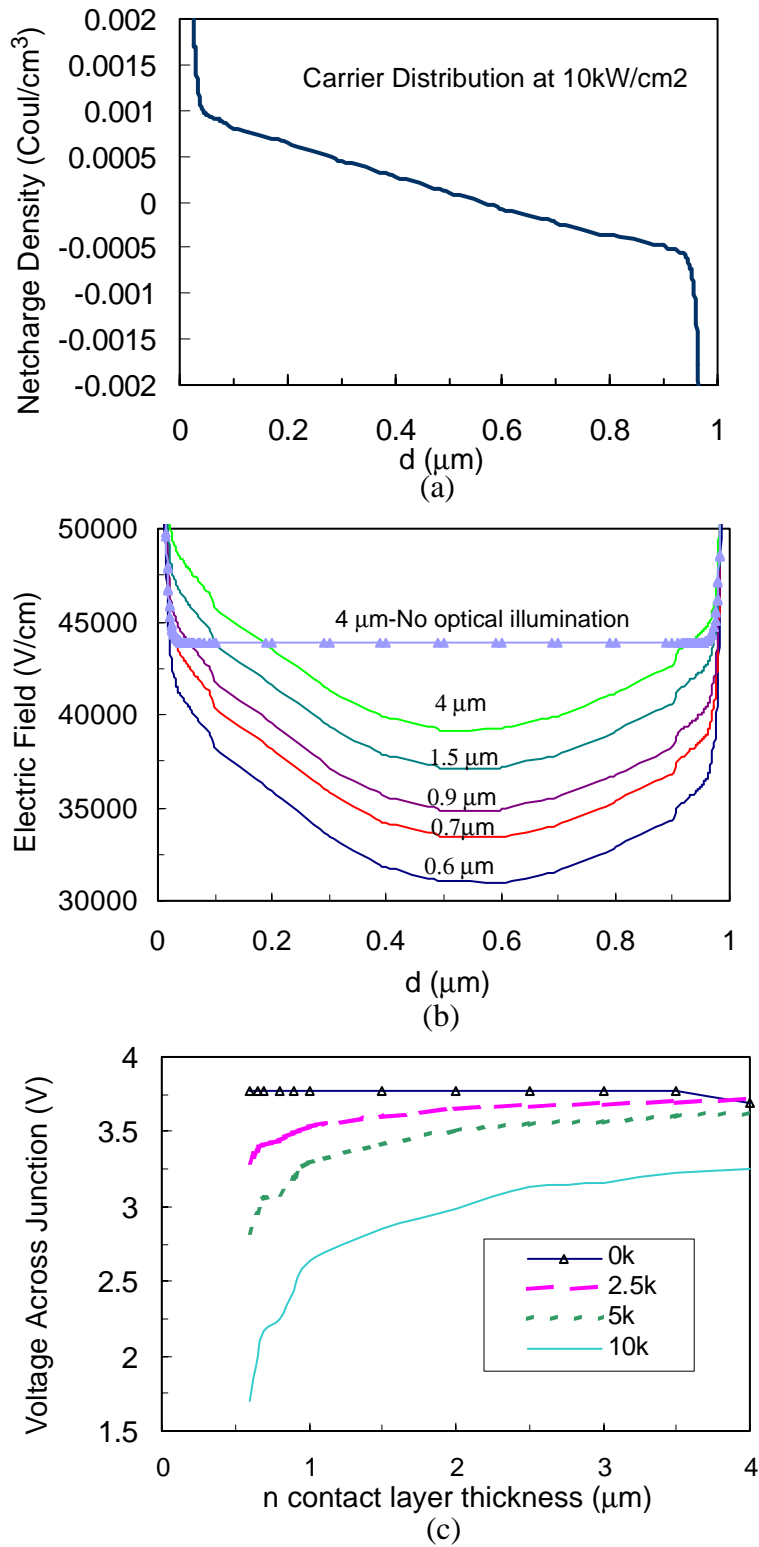


**Figure 3.5:** (a) Net charge density, (b) electric field and (c) voltage for device with 1μm intrinsic region thickness under illumination at different optical intensities.

under the same bias voltage. The additional voltage drops across the intracavity contact layer the leakage photocurrent generated by the laser illumination. Since the lateral resistance increases with decreasing n-type contact layer thickness, the effective voltage drops even more for n-type contact layer thickness smaller than  $1\mu\text{m}$ . To minimize the voltage drop at high optical intensities, the first 14 pairs of the bottom DBR mirrors are n-doped to increase the n-type contact layer thickness. Since the DBR mirrors are out of the optical cavity and they are n-type, the optical free-carrier absorption is rather small. Further increase in the contact layer thickness will increase fringe capacitance caused by the thick conducting contact layer.

### 3.2.2.3 Thermal effect

Another probable mechanism that could affect the high speed performance, especially contrast ratio, of the device at high optical intensity is the thermal effect. As the incident optical power increases, the temperature of the device also increases. The modulator is designed to have a maximum contrast ratio when the wavelength spacing between the exciton peak and Fabry-Perot dip has a certain value (around 15nm for our design). This condition can only be achieved within a small temperature range because of the significantly different temperature dependencies of the exciton peak and Fabry-Perot resonance. The exciton resonance shift is caused by the reduction of the bandgap energy with increasing temperature, resulting in a red shift of  $2.4\text{\AA}/^\circ\text{C}$ . The Fabry-Perot resonance also shifts to a longer wavelength due to the thermally induced refractive index change, but at the slower rate of  $0.8\text{\AA}/^\circ\text{C}$  [66]. Because of the different shift rate of the exciton absorption and Fabry-Perot resonance, the net effect is a reduction of the wavelength spacing between the exciton peak and the Fabry-Perot resonance, and hence the optical absorption at resonance. This also red shifts the wavelength and decreases the value of the highest contrast ratio.

However, the rising temperature will only affect the modulation depth of the device, not the  $f_{3dB}$  modulation bandwidth of the device. In comparison for VCSELs, this same

mismatch of the shifts causes the laser output power to decrease and eventually, lasing to terminate [55].

### 3.3 Transmission Line Structure

The modulator diode is integrated with a coplanar microwave probe for wafer level testing. The benefits of on-wafer microwave testing are well demonstrated in the GaAs MMIC community. The key advantages are much lower measurement cost, greater accuracy and faster testing as it eliminates the need to dice and bond devices. Final processing and bonding can be done after microwave measurements. On-wafer measurements are much more accurate since there are no bond wire or package parasitics to obscure the intrinsic device data. This is also a practical means to gather statistical quantity data.

To minimize the microwave reflection of the coplanar microwave probe, the characteristic impedances of the probe and the tapered feed line are designed to be  $50\Omega$ . The characteristic impedance,  $Z_0$ , is equal to that of coplanar waveguide (CPW), and can be found from commercial software such as Agilent ADS [67]. However, an analytical form is sometimes more desirable as it provides greater intuitive insight into the process. An analytical expression is given in Appendix B [68][69][70]. The characteristic impedance of the probe for a pitch size of  $150\mu\text{m}$  along with the tapered microwave feed line is shown in Figure 3.6. The metal line width and spacing are adjusted so that the characteristic impedance is as close to  $50\Omega$  as possible. In comparison, the characteristic impedance

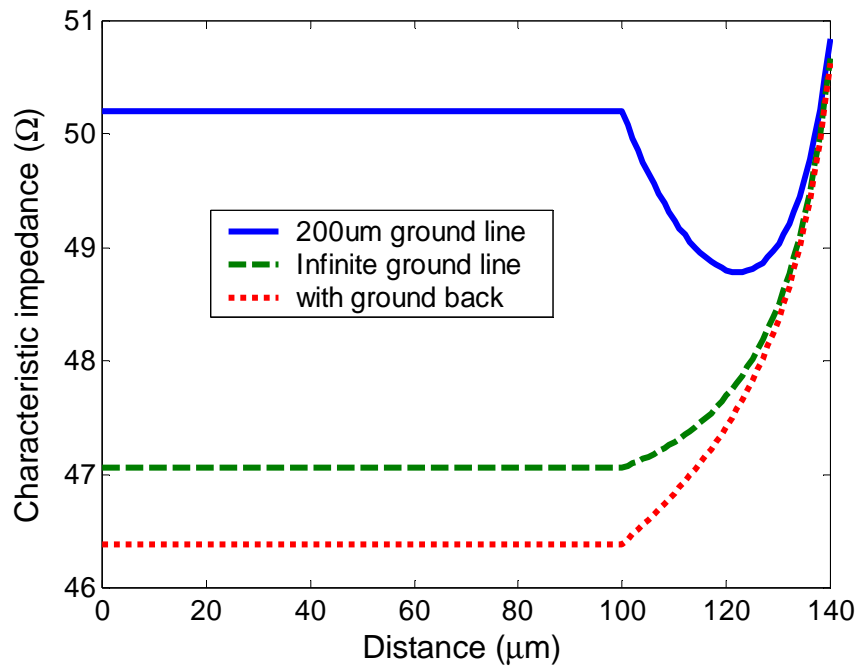


**Figure 3.6:** Characteristic impedance of probe pad and feed line.

for infinite ground line width or with back ground plane are also shown in the same figure as dash and dot lines respectively.

To reduce the microwave metal loss, relatively thick metal  $0.5\mu\text{m}$  Au lines are used. This thick metal only effects the metal-air impedance, not the characteristic impedance of the microwave feedline.

# 4

## *Device Fabrication and DC Characterization*

### 4.1 Epitaxial Structure

Following the optimization for high speed, low driving voltage operation, a high speed modulator was designed based on 75Å GaAs quantum wells. The device is grown on a semi-insulating GaAs substrate for high-speed operation using molecular beam epitaxy (MBE). The growth temperature is 650°C. Figure 4.1 shows the complete epitaxial structure.

26 pairs of 75Å GaAs quantum well with 45Å Al<sub>0.35</sub>Ga<sub>0.65</sub>As barriers were embedded in the optical cavity, which is 2.5λ long (including spacer, quantum well region and 0.5μm intracavity contact region). To match the effective back mirror reflectivity, the top mirror consists of 2 pairs of DBR with alternating Al<sub>0.35</sub>Ga<sub>0.65</sub>As/AlAs quarter wave layers centered at 845nm, giving a calculated  $R_f = 50.6\%$ . The back mirror consists of 25.5 pairs of the same DBR multilayer stacks, giving a calculated  $R_b = 99.3\%$ . The DBR mirror stacks, consisting of Al<sub>0.35</sub>Ga<sub>0.65</sub>As and AlAs, both have larger bandgap energies than the optical transition energy, there is no optical loss from the mirror stacks. Fewer pairs of DBR stacks could be used to achieve the same reflectivity if a lower bandgap material with lower Al concentration were used instead of Al<sub>0.35</sub>Ga<sub>0.65</sub>As due to the higher index contrast. However, the same Al concentration was used in both the mirrors and the barriers due to the difficulty associated with ramping the Al source temperature up and down during MBE growth.

The first 14.5 pairs of back Al<sub>0.35</sub>Ga<sub>0.65</sub>As/AlAs DBR mirror near the quantum well region were Si doped n-type at  $2.4 \times 10^{18}/\text{cm}^3$  (Al<sub>0.35</sub>Ga<sub>0.65</sub>As) and  $5.6 \times 10^{18}/\text{cm}^3$  (AlAs), the intracavity contact layer Al<sub>0.1</sub>Ga<sub>0.9</sub>As was Si doped n-type at  $1.9 \times 10^{18}/\text{cm}^3$  and

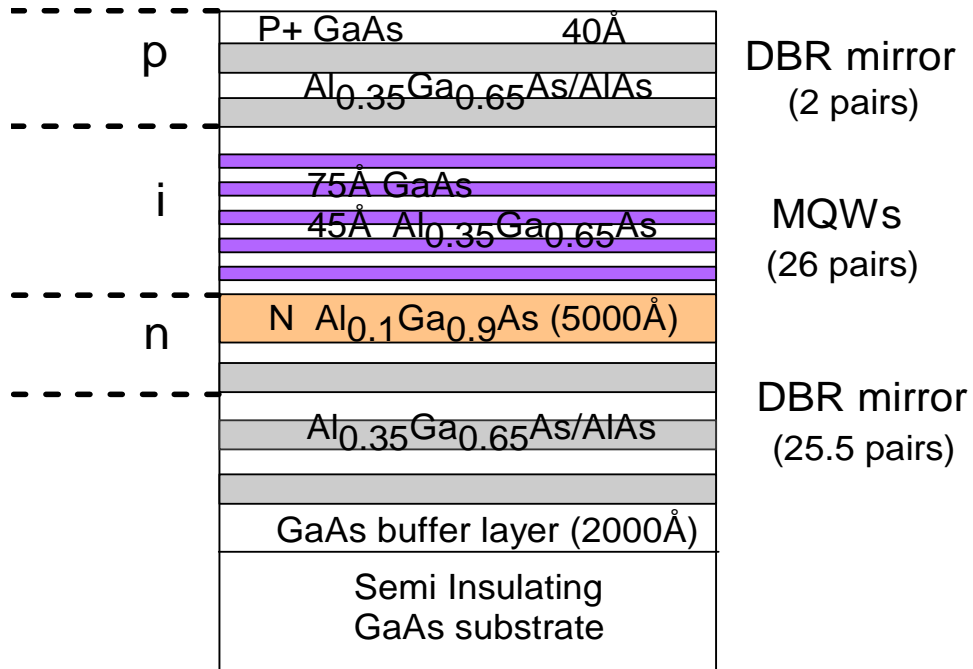


**Figure 4.1:** Epitaxial structure of high speed asymmetric Fabry-Perot modulator.

$4.1 \times 10^{18}/\text{cm}^3$  for the first and subsequent 2500Å respectively. The front quarter-wave stacks were Be doped p-type at  $5.1 \times 10^{18}/\text{cm}^3$  ( $\text{Al}_{0.35}\text{Ga}_{0.65}\text{As}$ ) and  $6.8 \times 10^{18}/\text{cm}^3$  (AlAs). The 20Å  $\lambda/2$ -cavity spacer layer was Be doped p-type at  $1.9 \times 10^{19}/\text{cm}^3$ . The last 40Å GaAs cap layer, which was added to prevent AlGaAs from oxidizing, was doped at  $1.8 \times 10^{19}/\text{cm}^3$  to assure better p-metal contact. This very thin 40Å cap layer, although heavily p doped, is outside the optical cavity and its optical effect is insignificant.

In order to obtain precision growth of the device, two *in situ* corrections were used during growth. At two selected points, the growth was interrupted and the reflection spectrum was measured without moving the wafer from the vacuum system[71]. After growing the first 11 pairs of the bottom DBR layer stacks, the wafer was positioned near a viewport in the transfer tube of ultra high vacuum (UHV) MBE system. The reflectivity spectrum was taken and compared with optical simulation result. A subsequent growth

correction was made to center the mirror's high reflectivity at the wavelength where the device was to operate ( $\sim 845\text{nm}$ ). In order to achieve high contrast ratio, the optical wavelength spacing between Fabry-Perot resonance and exciton absorption peak is very critical. Another *in-situ* growth correction was made right before the growth of the top DBR mirror stack. By comparing the measured reflectivity spectrum with simulation results, we can precisely determine how much cavity remains to be grown to ensure the right spacing between the exciton resonance and Fabry-Perot dip. An additional  $20\text{\AA}$   $\text{Al}_{0.1}\text{Ga}_{0.9}\text{As}$  layer was added to adjust the optical cavity length to an exact integer number of  $\lambda/2$ , giving a cavity order of  $m=5$  (optical cavity length= $5\times\lambda/2$ ).

Figure 4.2 shows the reflectivity spectrum of the wafer after growth and optical simulation results. Note the good agreement between them, which also demonstrates the power of *in-situ* correction to obtain the designed device. The amplitude discrepancy is due to the photodetector response.

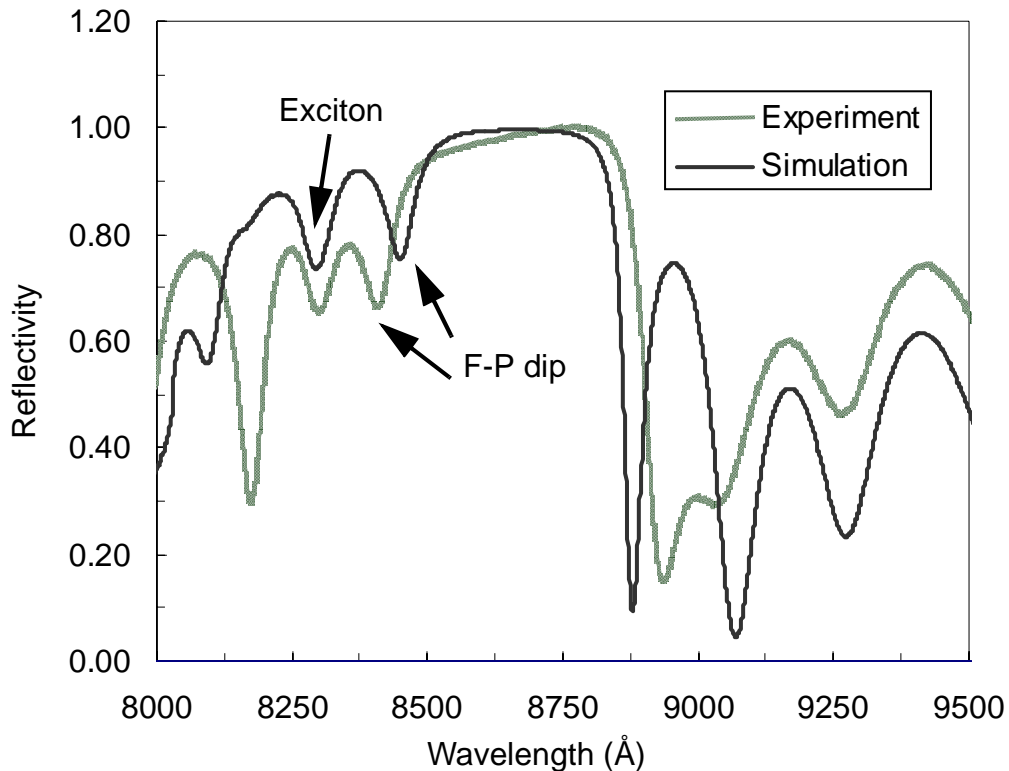


**Figure 4.2:** Un-normalized reflectance spectrum of the wafer structure after growth.

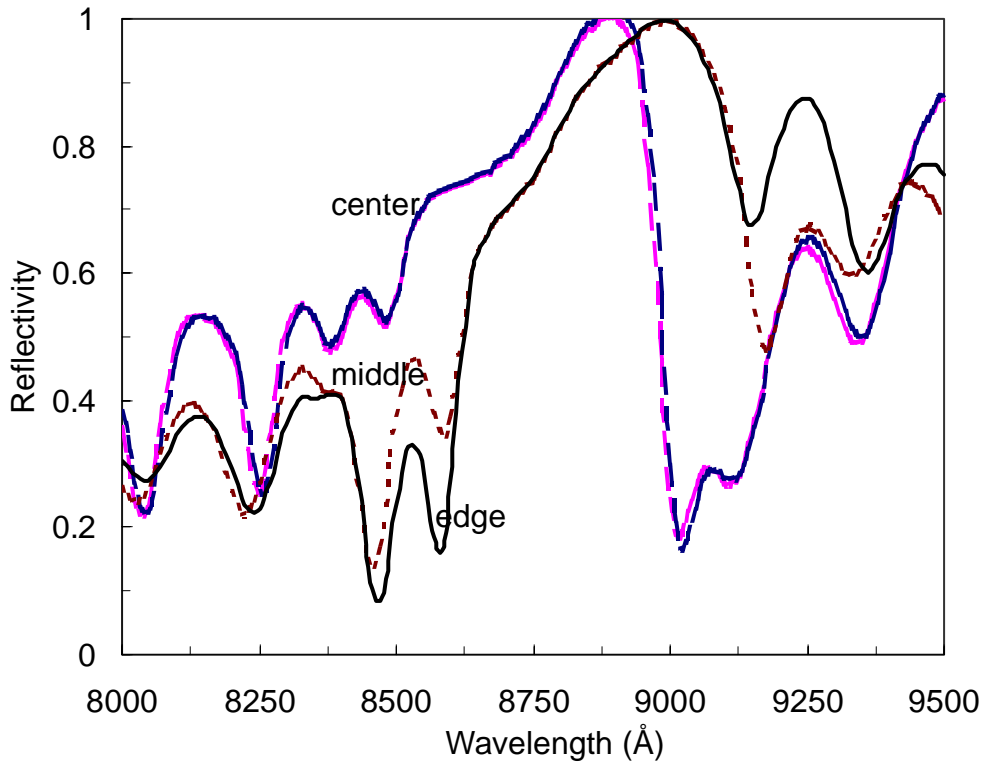


**Figure 4.3:** Reflectivity of the device from the center to the edge of the wafer.

Due to the growth rate variation across wafer, the device characteristics vary across the wafer. For the MBE system we use, Varian Gen II, the uniformity from the center to the edge of the 2" wafer is about 2%. Figure 4.3 shows the reflectivity spectra from the center to the edge of 2" wafer (#524) after growth. Due to the growth variation, the working wavelength and the contrast ratio vary across wafer.

## 4.2 Device Fabrication

### 4.2.1 Processing steps

After the wafer has been grown by MBE successfully, we fabricate the high speed modulators using the processing steps outlined in Figure 4.4. The processing steps include 1) p-contact metal evaporation and lift-off, 2) intracavity contact layer etch, 3) n-contact

metal evaporation, lift off and contact annealing, 4) mesa etch, 5) photo BCB passivation/planarization, and 6) transmission line evaporation and lift-off.

Detailed processing steps are listed in Appendix C. Below is a brief description of the process steps.

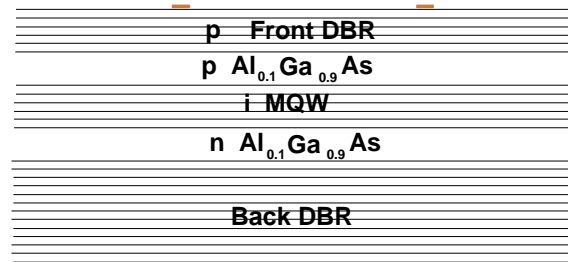
The first step (Figure 4.4(a)) is evaporation of the Ti/Pt/Au (250Å/400Å/1000Å) p-contact metal by electron beam evaporation. Titanium (Ti) helps the metal contact adhere to the wafer while platinum (Pt) in the p-contact helps prevent gold diffusion in subsequent high temperature processing. Following the p-contact metal evaporation, a standard metal lift-off process in an ultrasound bath is used to form the p-contact.

Using the second mask, we etch through the intrinsic layer to the n-intracavity contact layer region with a reactive-ion-etch (RIE) using a mixture of Ar/Cl<sub>2</sub> gases, followed by a short wet etch to remove any surface damage caused by RIE. To better control the etch depth, a dummy wafer, with the same epitaxial structure, was RIE etched to calibrate the etch rate right before the RIE etching of real devices. An SEM picture of the device at this point is shown in Figure 4.5(a).

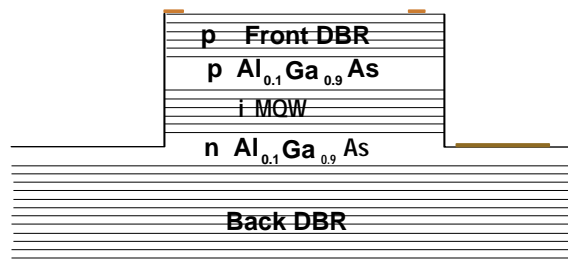
The third mask process was n-contact (Figure 4.4(b)). An n-contact metal consisting of Au/Ge/Ni/Au (400Å/120Å/125Å/1000Å) was E-beam evaporated. After lift-off, the contacts were alloyed using rapid thermal annealing (RTA) at 405°C for 30 seconds. Figure 4.5b shows SEM picture of the device after this processing step.

The fourth mask process was the mesa RIE etch. This step removes the remaining conductive layers and etches all the way down to the semi-insulating GaAs substrate in the feed line and transmission line regions. Thicker photoresist was used as the etch mask and the same mixture of Ar/Cl<sub>2</sub> gases as above was used in RIE etching.

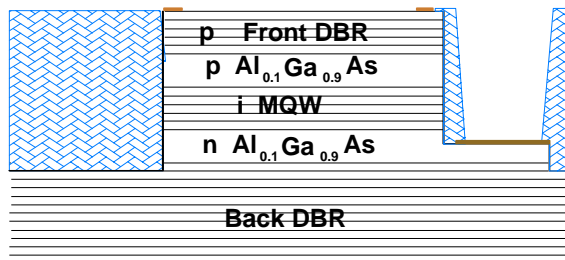
After further RIE etching through the n-doped region to form the mesa, photo benzocyclobutenes (BCB) was used to passivate and planarize the device with the fifth mask (Figure 4.4(c)). Photo BCB is a photo imagable material, its properties and detailed processing will be discussed in the following section.



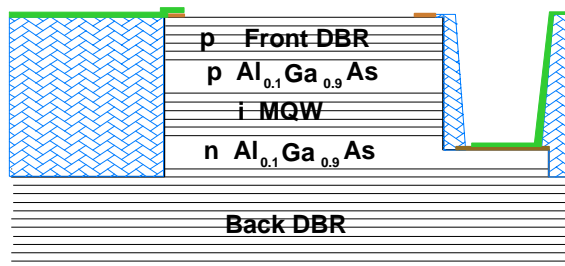
(a)



(b)

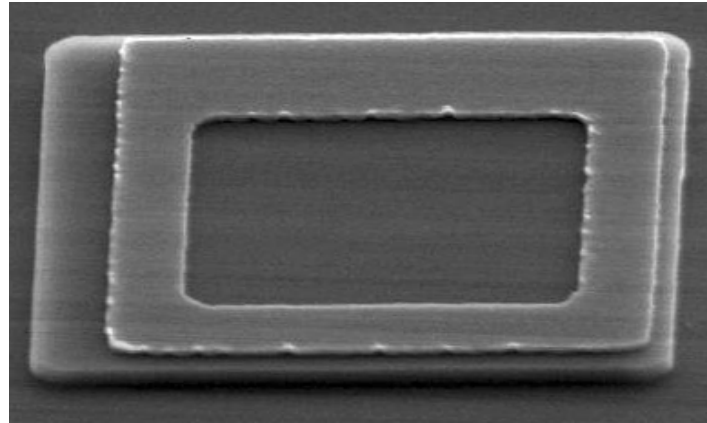


(c)

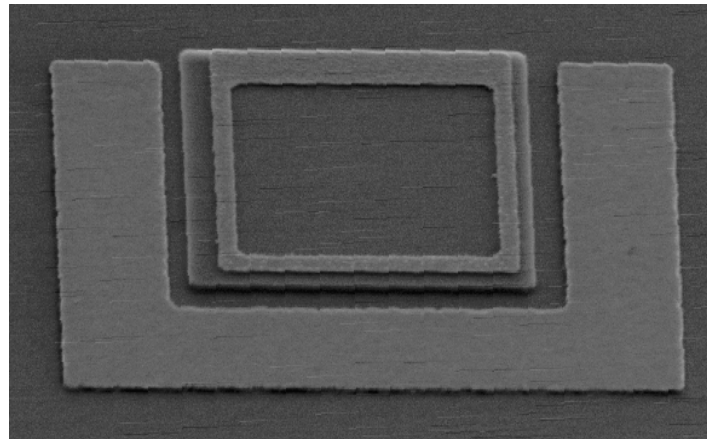


(d)

**Figure 4.4.** Processing steps for fabricating high speed modulators



(a)



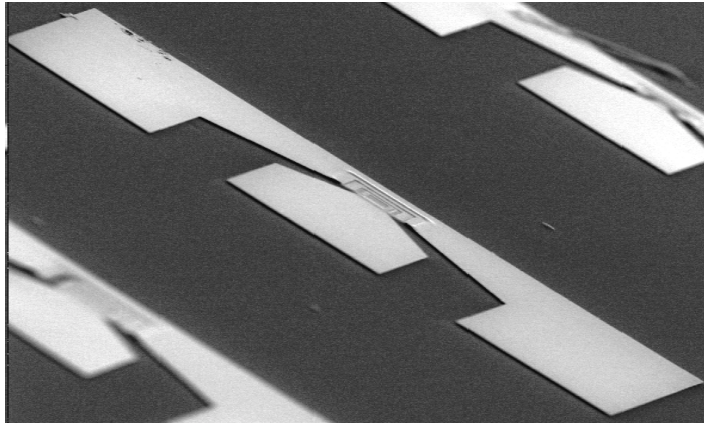
(b)

**Figure 4.5:** The SEM views of a device: (a) after p-contact ring and n contact etch (b) after n intracavity contact.

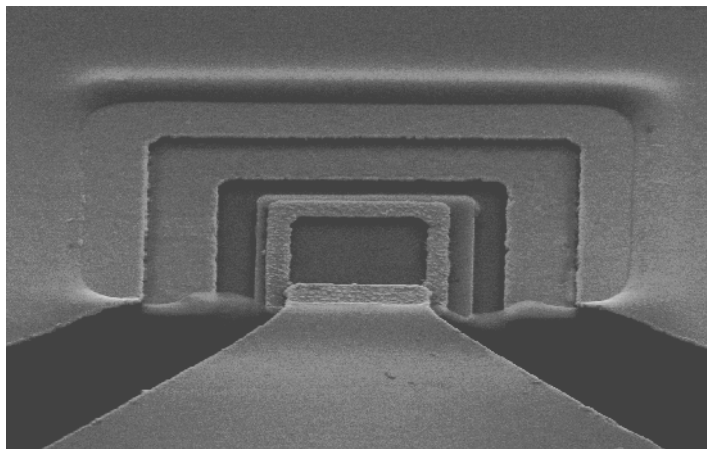
The sixth mask process was the final transmission line evaporation (Figure 4.4(d)). Thick metal Ti/Au ( $500\text{\AA}/5000\text{\AA}$ ) was evaporated for better microwave conductivity. Thicker photoresist and chlorobenzene soaking were used to help the lift-off.

Figure 4.6(a) is an SEM picture of the completed devices with coplanar microwave feed line, microwave probe and modulators marked on the pictures. The mask pattern contained many devices of different sizes, ranging from  $100\mu\text{m}$  down to  $5\mu\text{m}$ . The mask pattern also contained calibration devices (open, short) for probe pad parasitic removal

(PPR). Figure 4.6(b) is the close-up SEM view of a single device with optical window, photo BCB region, p-contact and n-contact.



(a)



(b)

**Figure 4.6:** The SEM view of (a) the completed devices and (b) close-up of a device.

### 4.2.2 Photo BCB processing

In the processing of high speed devices, photo BCB was used to passivate and planarize the devices. The planarization of devices is very important for subsequent flip-chip bonding. Photo BCB is an organic polymer dielectric. It overcomes some of the limitations of traditional inorganic dielectric materials, such as silicon nitride  $\text{Si}_3\text{N}_4$  or  $\text{SiO}_2$ ,

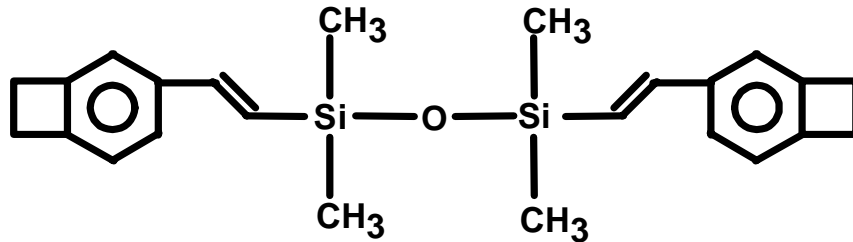


**Figure 4.7:** Structure of Benzocyclobutenes (BCB).

which are commonly used as passivation material in thin conformal coatings for ICs. When the applied film thickness is greater than  $1\mu\text{m}$ , inorganic dielectric materials tend to sustain stress and do not planarize the substrate. BCB polymer is derived from prepolymerized monomers of a generic form and its structure is shown in Figure 4.7. The polymerization of BCB is achieved by thermal rearrangement of the molecules under thermal curing. The  $250^\circ\text{C}$  cure temperature of BCB is lower than that for most polyimides, which are typically around  $350^\circ\text{C}$  to  $400^\circ\text{C}$ . It is solvent resistant once it is cured so that it can withstand solvents and etches used in standard Si or GaAs processing. More importantly, it offers several advantages over inorganic dielectrics and other kinds of polyimides. It has low stress ( $< 28\text{MPa}$ ), high degree of planarization ( $> 90\%$ ) and good adhesion to both GaAs substrate, metals (such as copper, gold, or aluminium) and itself [72].

Electrically it has a low dielectric constant of 2.65 up to 20GHz and small dissipation factor of 0.002 up to 10GHz. In high frequency interconnects, the transmission line losses consist of conductor and dielectric losses. Conductor losses caused by the “skin effect” phenomenon are usually proportional to the square root of frequency whereas the dielectric losses are directly proportional to frequency. As the operation frequency increases, dielectric losses begin to dominate. By using low dielectric constant and low microwave loss material as the passivation layer, the parasitic capacitance and transmission line losses can be minimized [73][74].

The pattern of photo BCB is defined by conventional photolithography techniques. It offers nice via shape and surface smoothness compared to non-photo-imagable BCB. The gentle sidewall slope ( $\sim 70^\circ$ ) facilitates the metallization after the via is formed since the metal can cover the sidewall easily. This also eliminates the time-consuming patterning methods used by non-photo-imagable BCB, ultimately reducing processing cost and improving yield [75].

Because of the nice mechanical and electrical properties of photo BCBs, they are gaining great popularity as interlayers of multilayer interconnect structures in high density multichip modules (MCM), redistribution layer in flip-chip solder bumping and planarization layer in flat panel displays [72][75]. They also find great applications in the area of optoelectronic integrated circuits, where they can be used as light-guiding layers as well as dielectric interlayers to optimize the high-speed characterization of optoelectronic devices.

The processing of photo BCB includes: (1) spin coating and pre-exposure bake, (2) exposure, (3) solvent development, (4) thermal curing, and (5) plasma descum [76]. The detailed recipe is described in Appendix C.

In order to achieve the desired film thickness, different photo BCB formulation and spin coating procedures will have to be used. Cyclotene 4024 from Dow Chemical Company was used in our devices, which gives a cured film thickness of  $3\sim 7\mu\text{m}$  before plasma descum.

The photosensitive Cyclotene formulations are negative acting and sensitive to 365nm light (I-line of mercury lamp) or broad band radiation. Typical exposure dosage for Cyclotene 4024 is about  $25\text{mJ}/\text{cm}^2$  per  $\mu\text{m}$ . Pattern development after exposure is accomplished in DS3000 solvent at  $32^\circ\text{C}$  and rinsed in the same solvent at  $23^\circ\text{C}$ . To stabilize the via shape, hot plate bake is used after the development.

After the photolithographic processing, the patterned film is polymerized in thermal curing to ensure the resistance to subsequent processing. Since Cyclotene films are

susceptible to oxidation at elevated temperatures, the thermal curing must be carried out in an inert gas or vacuum oven. The cure profile is listed in Appendix C, a temperature of 250°C for 60 minutes is used for hard cure to reach a polymer conversion ratio of greater than 95% [77].

Following thermal curing, the film is descummed by brief exposure to a plasma to remove any residual polymer (< 1000Å thick) left behind in the developing process. Since there is silicon in the Cyclotene polymer, some fluorine is necessary in the etch gas. An mixture of O<sub>2</sub>/SF<sub>4</sub> gases (90:10) was used. This provides a good balance of organic etching by O<sub>2</sub> and silicon etching by SF<sub>4</sub>.

### 4.3 DC Characteristics

The electrical characteristics of the completed devices were measured with a HP 4156 semiconductor parameter analyzer. The completed devices exhibit very good diode characteristics with a turn-on voltage of 1.1V, a breakdown voltage of 15V and very low

leakage current density, about  $15\text{pA}/\mu\text{m}^2$ . Figure 4.8 shows the measured I-V curves for different device sizes.

The degree of planarization is  $> 80\%$  due to the use of photo BCB. This is a very desirable feature for the device integration with Si circuit using flip-chip bonding technique.

The DC reflection spectra are obtained using tungsten white light source, a half meter spectrometer and a silicon photodetector [42]. These spectra are of great interest as they provide the trace of exciton absorption and the optical bandwidth of the devices. Figure 4.9(a) shows the reflection spectra of a typical device under different reverse bias voltages. The device has small insertion loss of 1.74dB. As the bias voltage increases, the heavy hole exciton peak is shifted to a longer wavelength. When the exciton peak overlaps with Fabry-Perot dip, minimum reflection is achieved. The maximum contrast occurs at 846.7nm, where the reflection changed from 68% to 6.5% with a 3.5V swing, or from 52% to 6.5% with only 1.75V swing as shown in Figure 4.9(b). The device has very good

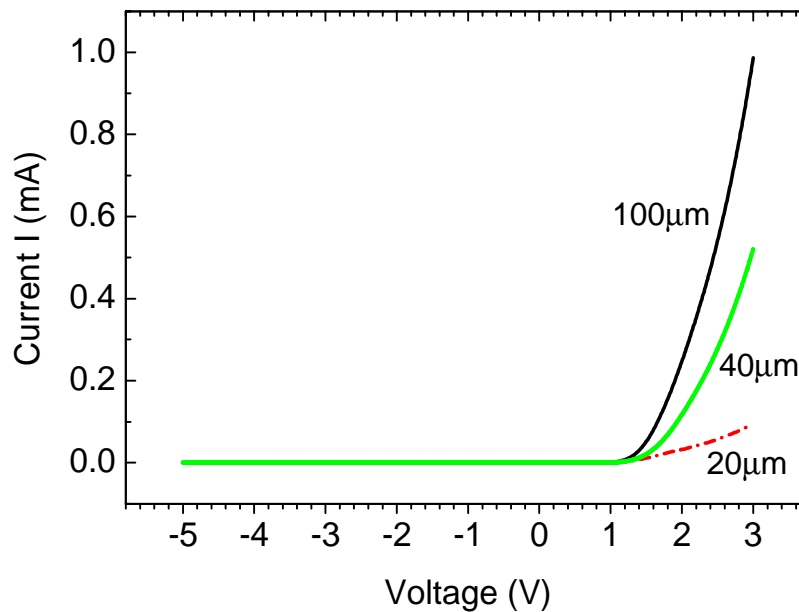


**Figure 4.8:** I-V characteristics of the devices with different sizes.

linearity between 1.75V and 3.5V range with 50% to 8% reflection change, which is a nice feature for analog applications.

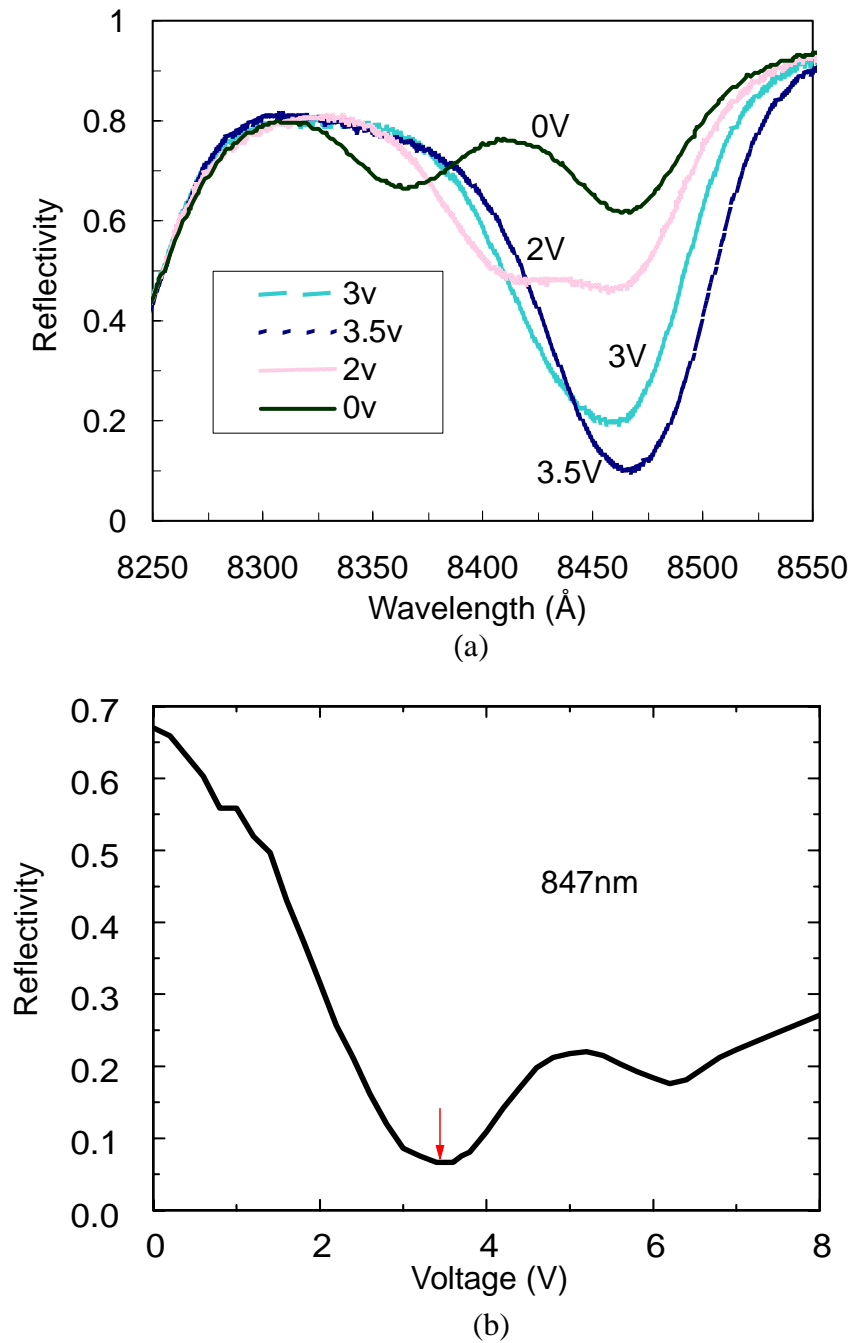


**Figure 4.9:** (a) DC modulation spectra of a typical device at various biases (b) reflectivity vs bias at 847nm. Maximum contrast is achieved when operating between 0V and 3.5V.

The measured spectra match the theoretical prediction in the previous chapter, although we didn't achieve the exact matching condition. There are several reasons that cause this imperfect matching. First, the spot size of incident light in the measurement is bigger than the optical window of the device, thus spurious reflections from the surrounding metal contact ring distort the absolute reflectivities. Other possible reasons are the limited resolution of spectrometer. Finally, this is also a result of MBE growth variation. Numerical simulation shows that the actual growth thickness is about 99% of the targeted value. This causes a misalignment of spacing between the exciton peak and Fabry-Perot dip, which decreases the contrast ratio.

# 5

## *High Speed Characterization*

### **5.1 Equivalent Circuit Extraction**

Accurate equivalent circuits are very important for designing devices with low parasitic elements and optimizing their high speed performance. They also help us understand the physical limitations of high speed operation. We obtain an equivalent circuit model of devices by using accurate de-embedding techniques which will determine the intrinsic physical parameters of the modulator diode itself and probe pad parasitics.

#### **5.1.1 Microwave scattering parameters**

Systems can be characterized electrically in numerous ways. At low frequencies, several parameter sets, such as impedance ( $z$ ), admittance ( $y$ ) and hybrid ( $h$ ) parameters are commonly used to represent the related voltages and currents. For the two port system shown in Figure 5.1, the relevant equations for impedance parameter sets are:

$$V_1 = Z_{11}I_1 + Z_{12}I_2 \quad (5.1)$$

$$V_2 = Z_{21}I_1 + Z_{22}I_2 \quad (5.2)$$

In order to determine the various  $Z$  parameters experimentally, open-circuit ports are conveniently used. For example,  $Z_{11}$  is determined easily once output port 2 is open-circuited ( $I_2=0$ ), and measuring voltage  $V_1$  and current  $I_1$  allows direct computation of  $Z_{11}$ , which is

$$Z_{11} = \left. \frac{V_1}{I_1} \right|_{I_2=0} \quad (5.3)$$

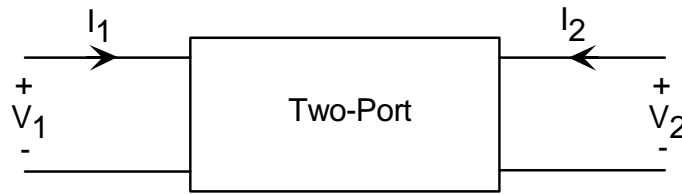


**Figure 5.1:** Port variable definitions.

At high frequencies, port voltages or currents are difficult to define and measure. It is also difficult to provide broadband opens or shorts. Some high frequency active devices (such as transistors) may experience oscillation or even stop functioning when they are terminated with open or short circuits.

A different set of parameters, called scattering parameters (or simply S-parameters), are used to avoid these measurement problems. They relate the incident and reflected voltage waves rather than port voltages and currents as shown in Figure 5.2. The source and load terminations are  $Z_0$ . The two port relation using S-parameters can be expressed as

$$b_1 = s_{11}a_1 + s_{12}a_2 \quad (5.4)$$

$$b_2 = s_{21}a_1 + s_{22}a_2 \quad (5.5)$$

where  $a_n$  and  $b_n$  are incident and reflected voltage waves normalized by the square root of  $Z_0$  so that they are physically equal to the square root of the power of the corresponding incident or reflected waves.

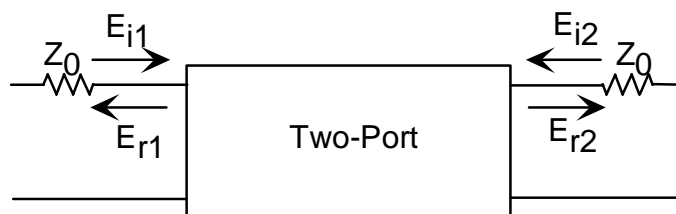


**Figure 5.2:** S-parameter port variable definitions.

The S-parameters can be easily found by driving one port with the other port terminated in  $Z_0$ . For example, by terminating the output with  $Z_0$ , the following parameters can be determined:

$$s_{11} = \frac{b_1}{a_1} = \frac{E_{r1}}{E_{i1}} = \Gamma_1 \quad (5.6)$$

$$s_{21} = \frac{b_2}{a_1} = \frac{E_{r2}}{E_{i1}} \quad (5.7)$$

Thus  $s_{11}$  is the input reflection coefficient, while  $s_{21}$  is a sort of gain which relates output wave to the input wave. Similarly,  $s_{22}$  and  $s_{12}$  can be determined using the same technique.

Usually, the reflection coefficient and the normalized load impedance are deterministic, which can be expressed as:

$$\Gamma = \frac{Z_1 - Z_0}{Z_1 + Z_0} = \frac{Z_{n1} - 1}{Z_{n1} + 1} \quad (5.8)$$

where  $Z_1$  is the load impedance and  $Z_0$  is the characteristic impedance of the line. Therefore more intuitive equivalent circuit elements, which are directly related to the device parameters, can be extracted by converting the more easily measurable S-parameters at high frequencies to impedance Z-parameters.

### 5.1.2 Accurate de-embedding technique

The complete equivalent circuit model of a high speed modulator integrated with microwave probe pads is shown in Figure 5.3. It consists of the intrinsic modulator diode and microwave probe pad parasitics. The intrinsic modulator diode has series resistance,  $R_s$ , and capacitance,  $C_d$ , while probe pad parasitics include pad capacitance,  $C_{pad}$ , and inductance,  $L_{pad}$ . Since the parasitics are independently measured using on wafer test patterns (open, short), we can de-embed the intrinsic circuit parameters of the modulator diode from parasitics using matrix manipulation. Practically, the commercial measurement

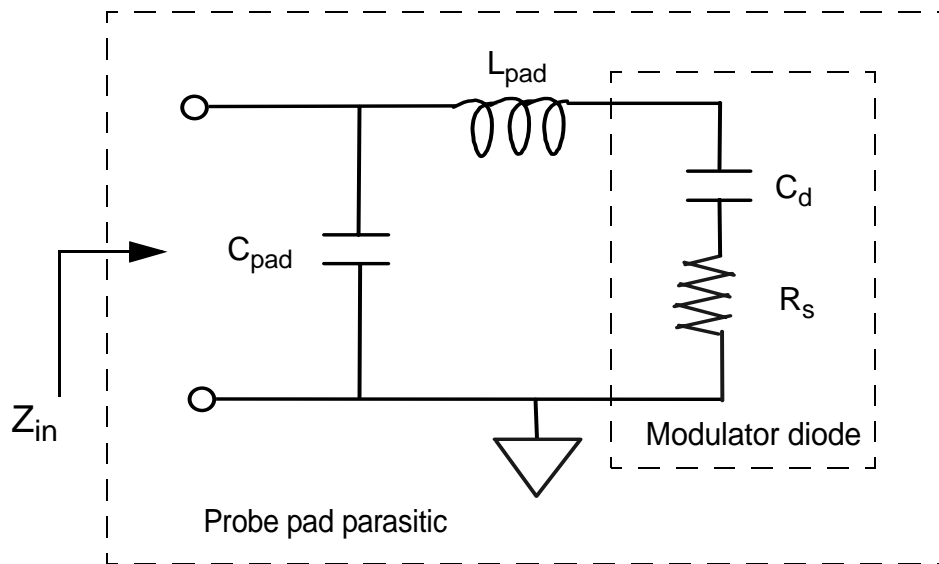


**Figure 5.3:** Complete equivalent circuit model of modulator diode and pad parasitics.

control software WinCal 2.1 from Cascade Microtech, a function called PPR (pad parasitic removal) will take care of the matrix manipulation and give us the S-parameter of the intrinsic modulator diode after the PPR de-embedding [78].

The scattering parameters of the device were measured over the frequency range of 0.1GHz to 20GHz by using Cascade MicroTech Summit 9301-U Probe Station, Cascade MicroTech air coplanar 40GHz probe (ACP-40-GSG-150) and an HP 8510C network analyzer. The measurement procedure is summarized as follows:

- 1) calibrate the port up to the point where the device is going to be inserted using Cascade Microtech on wafer LRM impedance standard substrate (101-190).
- 2) measure the S-parameters of the open pad test pattern
- 3) measure the S-parameters of the short pad test pattern
- 4) measure the S-parameters of the modulator diode integrated with probe pad
- 5) apply PPR function to the above three S-parameters to obtain the S-parameters of the intrinsic modulator diode.

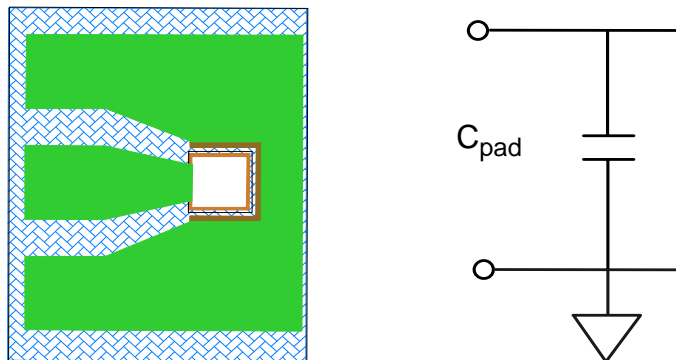


**Figure 5.4:** Open pad calibration test structure and its circuit model.

The pad parasitic capacitance was determined by measuring  $S_{11}$  parameter of a test pattern with the pads only. Figure 5.4 shows the open pad test structure and its corresponding circuit model. The simplicity of this circuit model with only one capacitance element is a direct consequence of the semi-insulating GaAs substrate and device isolation all the way down to the semi-insulating substrate. If a conducting substrate is used, a more complex model will have to be used with additional elements [81].

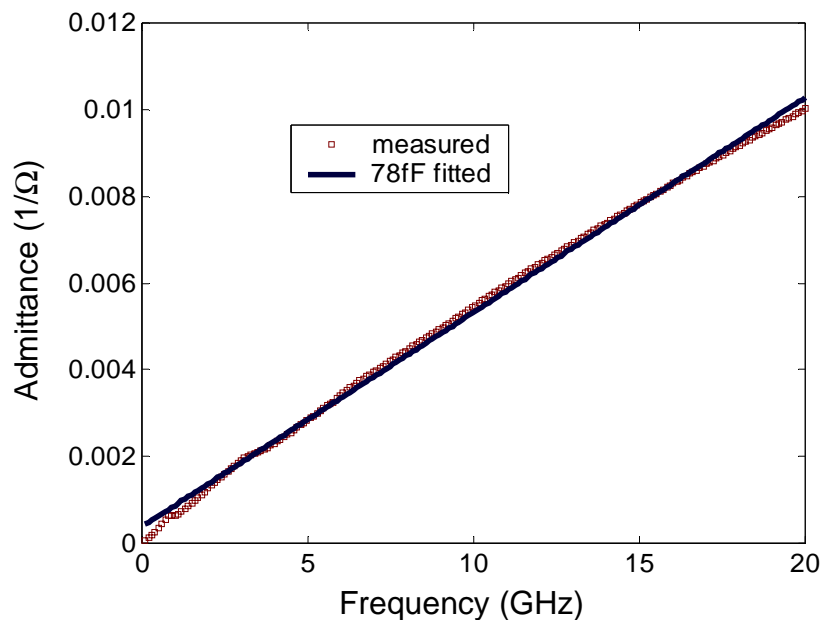


**Figure 5.5:** Admittance of open device as a function of frequency.

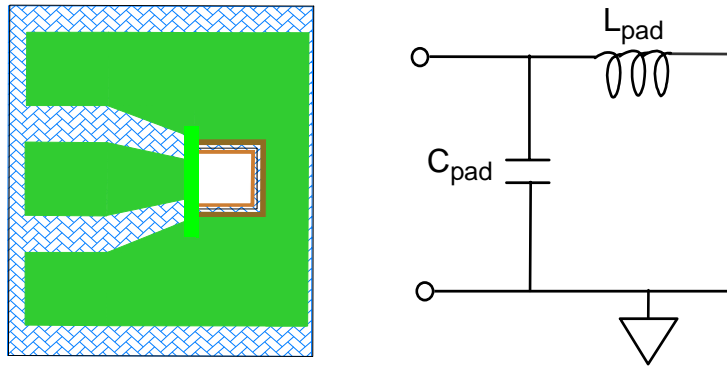


**Figure 5.6:** Pad short test structure and its circuit model.

The admittance of the open pad can be obtained from an independent measurement of  $S_{11}$  parameter of a open pad. The pad capacitance value,  $C_{\text{pad}}$ , was extracted as the slope of the imaginary part of the admittance  $\text{Im}[Y]=\text{Im}[j\omega C_{\text{pad}}]$  as shown in Figure 5.5.  $C_{\text{pad}}$  is about 78fF and is nearly constant from 0.1GHz to 20GHz with deviations from the mean values being less than 5%.

Similarly, the inductance of the probe pad can be extracted from an  $S_{11}$  parameter measurement of an independent short pad. Both capacitance and inductance of the probe pads are included in the pad short circuit as shown in Figure 5.6. We subtract  $C_{\text{pad}}$  (obtained from open pad measurement) first and  $L_{\text{pad}}$  is just the slope of imaginary part of impedance  $\text{Im}[Z]=\text{Im}[j\omega L_{\text{pad}}]$ . The inductance value is  $L_{\text{pad}} = 24\text{pH}$  and varies with frequency by 5%.

### 5.1.3 Resistance and capacitance of the intrinsic modulator diode

Having extracted capacitance,  $C_{\text{pad}}$ , and inductance,  $L_{\text{pad}}$ , of the parasitic probe pad, the resistance,  $R_s$ , and capacitance,  $C_{\text{dev}}$ , of the modulator diode can be obtained from  $S_{11}$

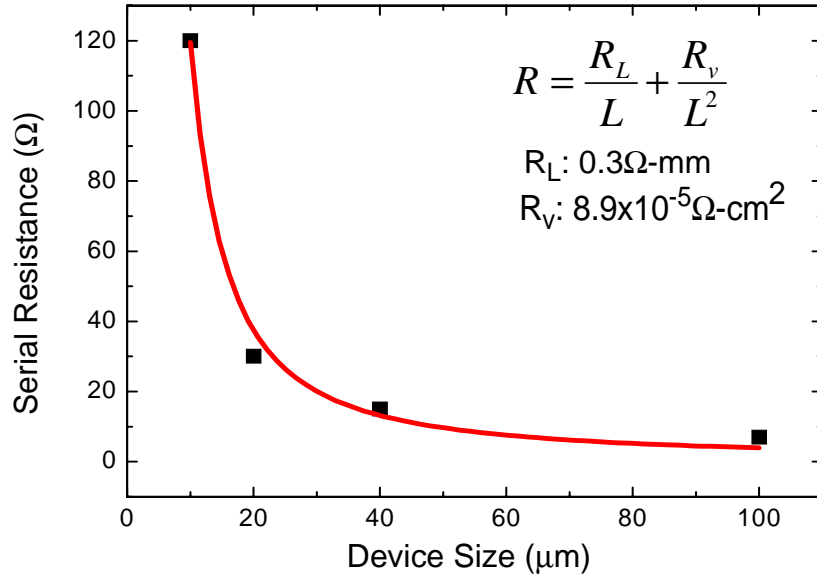


**Figure 5.7:** Series resistance of modulators of different sizes.

parameter after pad parasitic removal (PPR). The impedance of the modulator diode can be obtained from reflection coefficient  $S_{11}$  and is expressed as:

$$Z_{in} = \frac{1 + s_{11}}{1 - s_{11}} \cdot Z_0 = R_s + \frac{1}{j\omega C_{dev}} \quad (5.9)$$

The extracted serial resistance  $R_s$  of the modulator diode, which is the real part of  $Z_{in}$ , is presented as a function of device size in Figure 5.7. The resistance dependence on size can be further analyzed by fitting it to the empirical formula [55]:

$$R = \frac{R_L}{L} + \frac{R_V}{L^2} \quad (5.10)$$

The first term varies inversely with the device size  $L$  (or perimeter) to account for the contact, lateral, and constriction resistance contribution. The second term varies inversely with the device area (or  $L^2$ ) to reflect the voltage drops associated with uniform vertical current flowing through the top mirror and bottom intracavity contact layer. Fitting curve

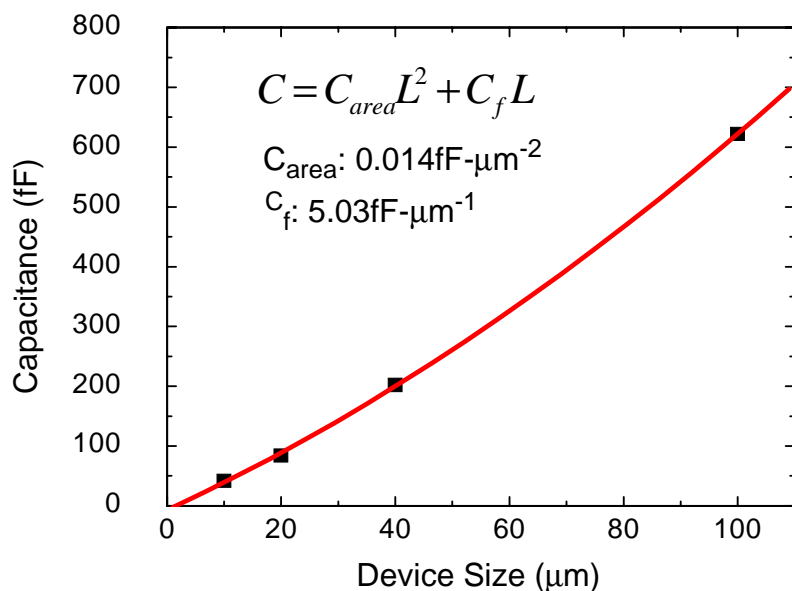


**Figure 5.8:** Capacitance of the modulator diode.

(solid line) and fitting parameters are shown Figure 5.7. The lateral resistance dominates for devices with physical size larger than  $30\mu\text{m}$ . This also emphasizes the need to minimize the lateral resistance in vertical cavity modulators.

Scaling the data as a function of device size is also insightful for evaluating the capacitance of the modulator diode. The extracted capacitance of the modulator diode, which is the slope of the imaginary part of  $1/Z_{in}$  i.e.  $Y_{in}$ , is presented as a function of device size in Figure 5.8. The capacitance dependence on size consists of area capacitance, which is proportional to the area of the device size (or  $L^2$ ), and the fringing capacitance, which is proportional to the perimeter (or  $L$ ) of the device [79][80]. The capacitances scale with the device size more linearly than quadratically, which implies that the fringe capacitance plays the more significant role. This is due to the thick n-type intracavity contact layer.

Figure 5.9 compares the  $S_{11}$  parameter produced by the circuit model with the measured  $S_{11}$  parameter of a  $40\mu\text{m} \times 40\mu\text{m}$  modulator diode with integrated probe pads at  $V_{bias} = -2.2\text{V}$  voltage and swing  $\Delta V = \pm 1\text{V}$  (7dBm). In the frequency range of measurement

from 0.1GHz to 20GHz, the computed  $S_{11}$  parameter agrees well the experimental data. This also verifies the circuit model of the complete device.

The equivalent circuit model can be used to calculate the voltage drops due to the diode capacitor,  $C_{pad}$ , and predict the optical modulation bandwidth  $f_{3dB}$  when the voltage drops to half of its value at low frequency.

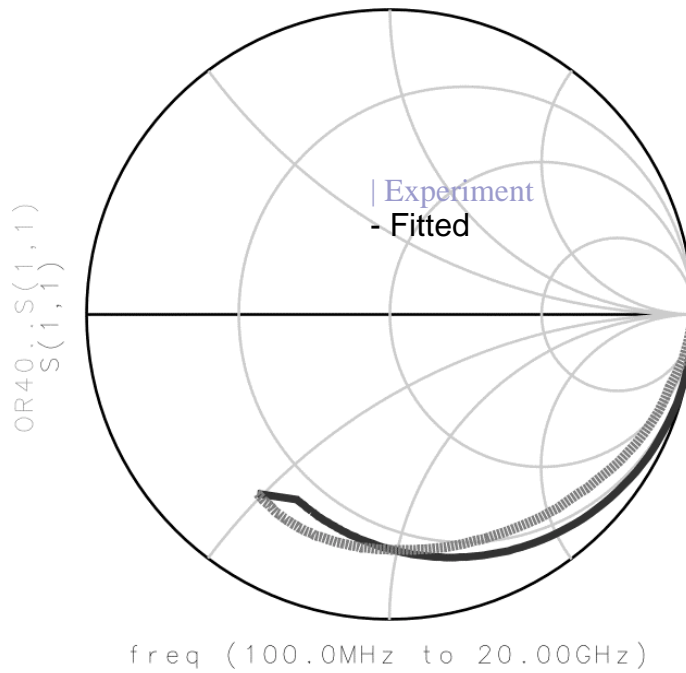


**Figure 5.9:**  $S_{11}$  parameter of a complete device.

This bandwidth is roughly equal to the same value obtained from open-circuit model [53], which is

$$f_{3dB} = \frac{1}{2\pi[C_{dev}(R_s + Z_0) + C_{pad}Z_0]} \quad (5.11)$$

Without the probe pad parasitics, which is usually the case in a real application where the modulator is flip-chip bonded, the  $f_{3dB}$  modulation bandwidth after accurate de-embedding is:

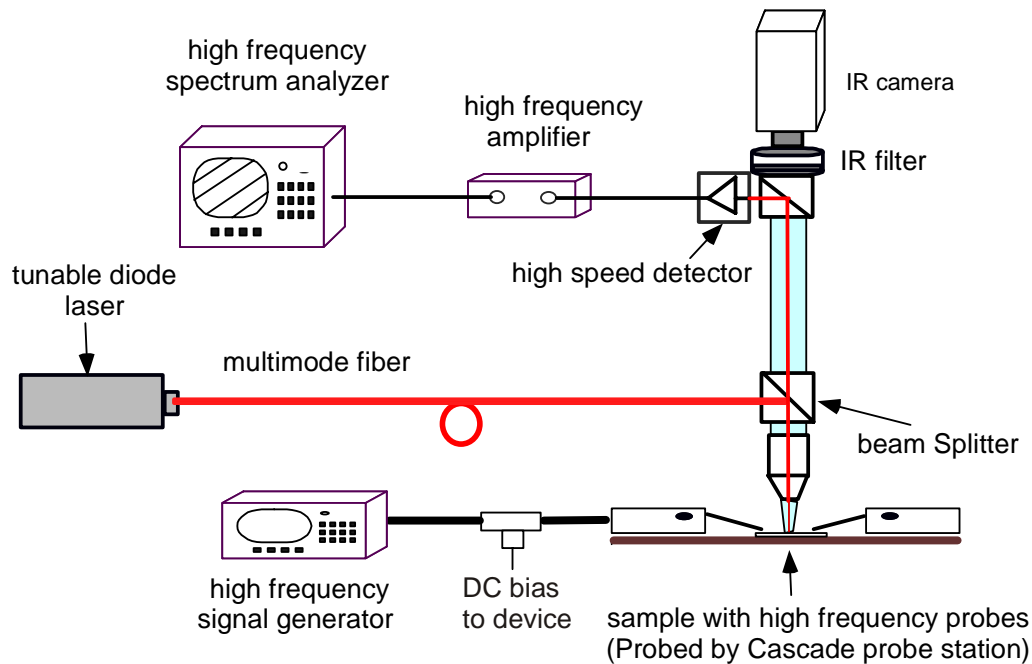
$$f_{3dB_{de}} = \frac{1}{2\pi C_{dev}(R_s + Z_0)} \quad (5.12)$$

Table 5.1 summarizes the extracted circuit parameters of complete devices with different modulator diode sizes. The calculated  $f_{3dB}$  bandwidth of completed devices (Equation 5.11) and the bandwidth of modulator diode itself by applying de-embedding technique (Equation 5.12) are also listed.

	$R_s$ ( $\Omega$ )	$C_{dev}$ (fF)	$f_{3dB}$ (GHz)	$f_{3dB_{de}}$ (GHz)
<b>100<math>\mu</math>m x 100<math>\mu</math>m</b>	8	622	4.0	4.4
<b>40<math>\mu</math>m x 40<math>\mu</math>m</b>	20	204	8.8	11.1
<b>20<math>\mu</math>m x 20<math>\mu</math>m</b>	25	82	16.0	25.9
<b>10<math>\mu</math>m x 10<math>\mu</math>m</b>	120	30	17.9	31.2

**Table 5.1:** Equivalent circuit elements and calculated modulation bandwidth.

Equivalent circuit models are also valuable diagnostic tools that provide information for improving the high speed performance of the devices. The physical basis of circuit model and the accurate determination of the element values provide feedback for modifying the device design and fabrication, which will improve high speed performance. The most obvious information obtained from the circuit modeling work is that as the device sizes shrink down, the modulation bandwidth is not increasing to the same scale, especially when the device is smaller than 20 $\mu$ m. This is due to the fact that the series resistance increase outpaces the reduction of capacitance because of the vertical mirror resistance and fringing capacitance for smaller devices.



**Figure 5.10:** Schematic of experiment setup to measure high speed E-O response.

## 5.2 High Speed E-O Response

### 5.2.1 Measurement setup

To demonstrate high speed modulation of the device, the setup shown in Figure 5.10 was used to measure the electro-optical response. All measurements were performed on-wafer using a Cascade MicroTech air coplanar GSG wafer probe (ACP40-GSG-150) and Cascade MicroTech Summit Probe Station. The RF driving voltage was generated by a HP 83732B CW Synthesized Signal Generator and a HP 8563E spectrum analyzer along with HP 8449B microwave amplifier coupled with a high speed photodetector to measure the modulator optical response.

A tunable SDL diode laser with tuning range of 830nm~850nm was used as the light source. The laser light was launched into a multi-mode fiber so that it can be easily brought into the device under test on the probe station through a microscope objective.

The reflected laser beam from the device is collected by a New Focus 25GHz bandwidth photodetector 1431.

The combined modulator/photodetector system is non-insertable, because it has a coplanar input and coaxial connector output. Because we are measuring a non-insertable device, a conventional response cannot resolve the measured characteristics from the unwanted effects of the microwave wafer probe and photodetector as shown in Figure 5.11. The device measurement was preceded by a calibration of the RF signal generator and spectrum analyzer to correct for the losses in the microwave cabling, bias tees and the detector response. The calibration data were subtracted from the raw data to obtain the calibrated frequency response of modulator.

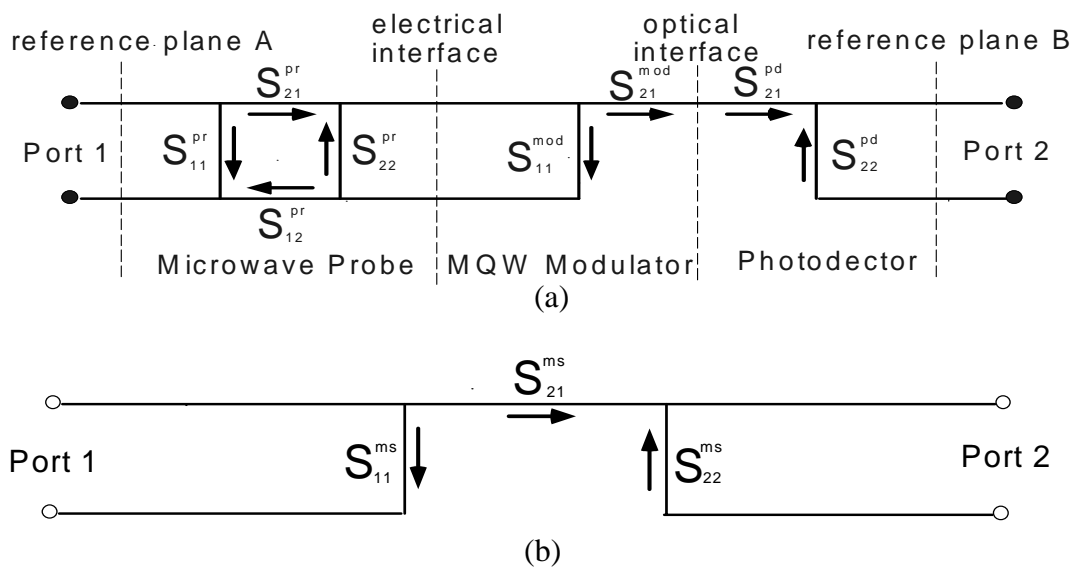


**Figure 5.11:** Signal flow of (a) combined microwave networks consisting of microwave probe, MQW modulator and photodetector (b) equivalent measured two-port network.

## 5.2.2 Results and discussions

According to the DC modulation spectra, the modulator performance should be optimum at a laser wavelength of 847nm and DC biased at -2.2V, AC voltage swing  $\pm 1V$ . Both open and  $50\Omega$  termination were tested. In the case of  $50\Omega$  termination, a second

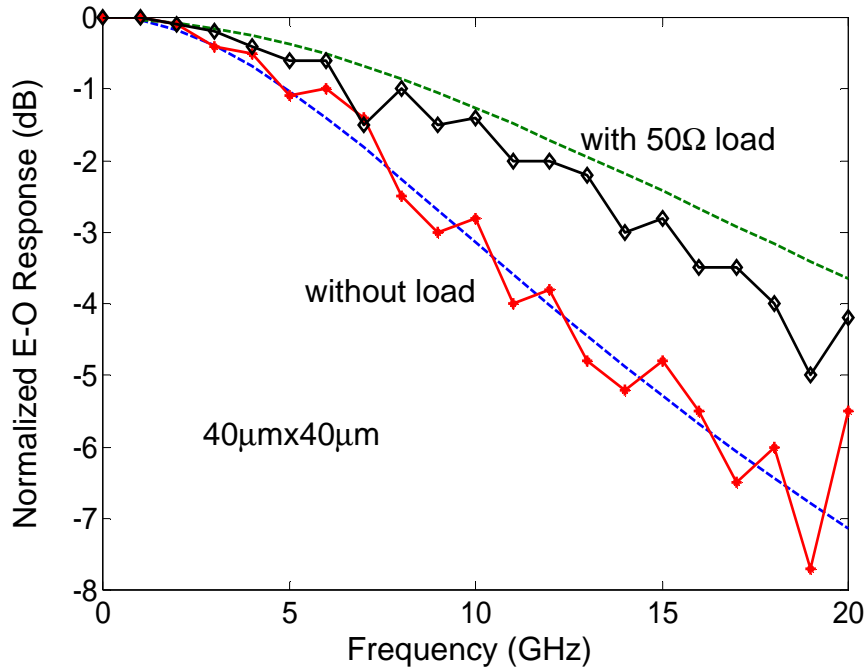


**Figure 5.12:** Normalized electro-optical response for a  $40\mu\text{m} \times 40\mu\text{m}$  device under different terminations.

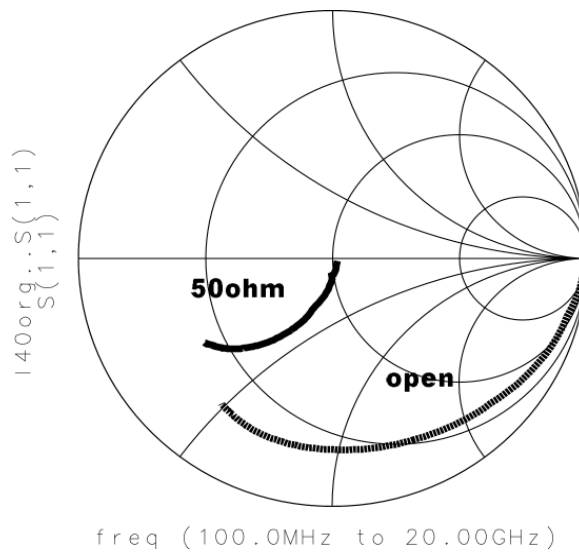
probe was connected to the second set of probe pads on the device and the output of the probe was terminated with a broadband  $50\Omega$  load.

Figure 5.12 shows the normalized electro-optical responses from 0.1GHz to 20GHz for  $40\mu\text{m} \times 40\mu\text{m}$  device under different terminations. The incident laser power on the device is about 1mW. The dots represent measured data and the dash curves represent the theoretical prediction using the equivalent circuit model obtained in Section 5.1. The RC limited prediction agrees with the measured data which proves that the modulators appear to be only RC limited at this optical intensity level.

Each curve was normalized relative to its low frequency signal level. At low frequencies, the absolute signal level for the  $50\Omega$  terminated device was about 6dB lower than that without load. This is because without a load, all the applied voltage drops on the devices. While loaded with  $50\Omega$  termination, the applied voltage is divided between source  $50\Omega$  resistor and the device. At low frequencies, there is only half of the applied voltage dropped across the device. Without a load, the  $f_{3\text{dB}}$  modulation bandwidth is about

10GHz. This increases to about 15GHz with a  $50\Omega$  load because of the decrease of microwave signal reflection at the input port, as shown by the measured  $S_{11}$  parameter in Figure 5.13.

The electro-optical response for different device sizes are also measured and the results are shown in Figure 5.14. The  $f_{3dB}$  modulation bandwidth increases for smaller devices due to the smaller capacitances. However devices smaller than  $20\mu\text{m}$  show less



**Figure 5.13:**  $S_{11}$  parameter of device under different terminations.

bandwidth improvement due to the integrated probe pad capacitance limitation and the significant resistance increase of the modulator diode.

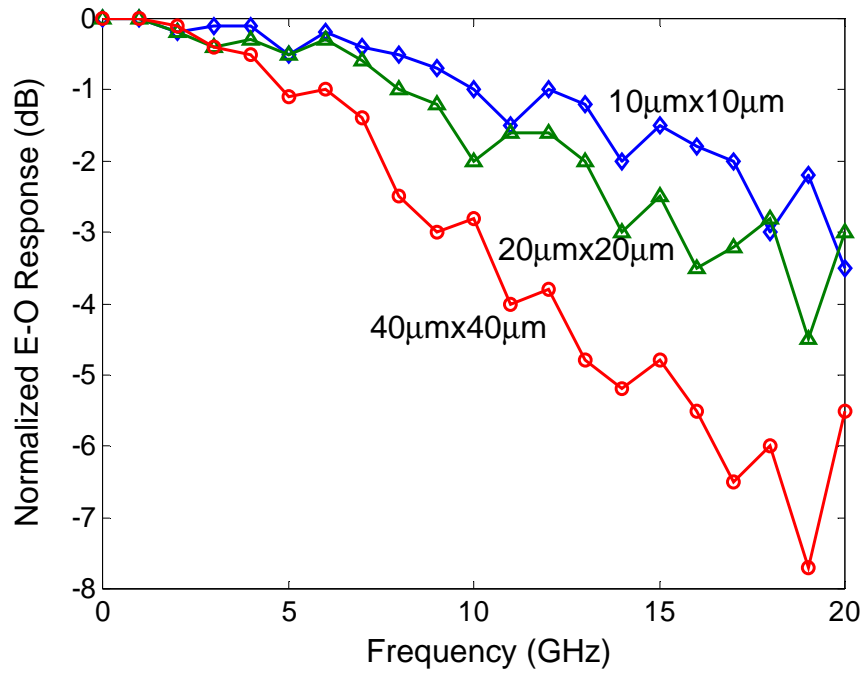


**Figure 5.14:** Normalized electro-optical response for devices of different sizes.



# 6

## *Carrier Dynamics and Photocurrent Response*

### **6.1 Carrier Dynamics**

Vertical cavity multiple quantum well (MQW) modulators are also finding applications as high speed photodetectors and all optical switching elements, both of which depend on carrier dynamic effects in the quantum wells. Also as MQW modulators are scaled to high optical powers and speeds, it is becoming important to understand the dynamics of photo-generated carriers in the active region. In this section, picosecond time-resolved pump/probe measurements were used to study the carrier dynamics of these high speed modulators.

#### **6.1.1 Photovoltage**

For low pump optical power, the transient change of reflectivity is mainly due to the quantum confined Stark effect. By monitoring the transient reflectivity change, the photovoltage change due to photo-generated carriers can be interpreted. The change of photovoltage is mainly due to the following two mechanisms: carrier sweep-out and diffusion recovery.

##### **6.1.1.1 Carrier sweep-out mechanism**

For a reverse biased p-i-n diode with active MQWs in the intrinsic region, as the pump pulse is absorbed in the MQWs, the photo generated carriers in the intrinsic quantum well region escape the quantum wells and move to the two electrodes.

In an MQWs system, the carrier sweep-out mechanism can be quite complicated due to the coupling between wells and carrier recapture by subsequent wells. Assuming the

recapture rate is small, the carrier escape from the quantum wells and travel to the two electrodes is mainly through the following processes: thermionic emission, tunneling and drift under external applied electrical field. A schematic of these processes is shown in Figure 6.1. A time constant is attributed to each of these process.

If we assume these three processes are independent and we neglect the recapture of carriers in the subsequent wells, the carrier transit time is:

$$\frac{1}{\tau} = \frac{1}{\tau_{thm}} + \frac{1}{\tau_{tun}} + \frac{1}{\tau_{dft}} \quad (6.1)$$

where  $\tau_{thm}$  is the thermionic emission time,  $\tau_{tun}$  is the tunneling time, and  $\tau_{dft}$  is the drift time, respectively. As will be seen in later calculations,  $\tau$  is determined by a number of intrinsic and external parameters. They include intrinsic material properties, such as carrier effective masses and band discontinuities, as well as specific device parameters, such as quantum well width and barrier thickness.

The thermionic emission time is the time it takes for the carriers to escape from a quantum well bound state into the conduction band continuum and is determined primarily by the probability that a carrier will have sufficient thermal energy to escape the barrier. By using the model developed by Schneider and von Klitzing [82], assuming the

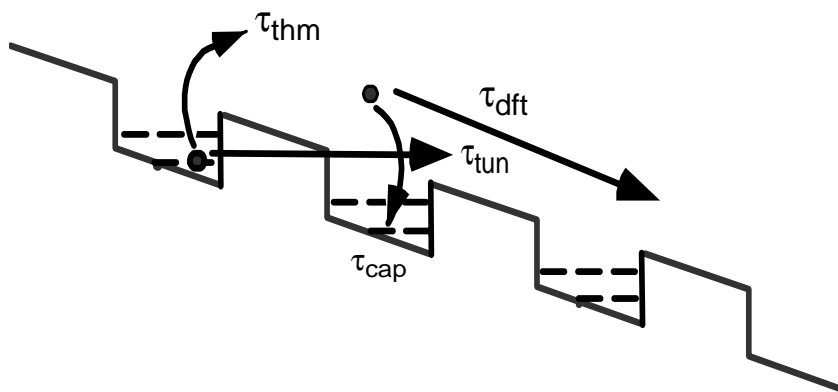


**Figure 6.1:** Various time constants involved in the carrier sweep-out.

carrier statistics are Boltzmann-like, the field dependent thermionic time constant can be expressed as:

$$\frac{1}{\tau_{thm_{e,h}}} = \sqrt{\frac{K_B T}{2\pi m_{e,h} L_w^2}} \exp\left[-\frac{H_{e,h}(F)}{K_B T}\right] \quad (6.2)$$

where the added subscript e,h refer to electrons or holes.  $K_B$  is the Boltzmann constant respectively,  $T$  is temperature,  $m_{e,h}$  is the carrier effective mass,  $L_w$  is the well width, and  $F$  is the electric field.  $H_{e,h}$  is the field dependent barrier height which the carriers must overcome, and is simply given by

$$H_{e,h} = \Delta E_{c,v} - E_{e,h}^{(n)} - \frac{|e|FL_w}{2} \quad (6.3)$$

where  $\Delta E_{c,v}$  is the barrier height for electron or holes, which are equivalent to the conduction band gap and valance band gap offsets.  $E_{e,h}^{(n)}$  is the  $n^{\text{th}}$  sub band energy level, and since most of the carriers are populated at  $n=1$  electron (or heavy-hole) ground state,  $n=1$ , these values are used in future calculations. As the field increases, the thermionic emission time decreases because the effective barrier height decreases.

The tunneling time can be calculated quantum mechanically using Airy function transfer matrix through the finite potential barrier [82]:

$$\frac{1}{\tau_{tun_{e,h}}} = \frac{nh}{4m_{e,h} L_w^2} \exp\left[-\frac{4\pi L_b \sqrt{2m_{be,h} H'_{e,h}(F)}}{h}\right] \quad (6.4)$$

where  $m_{be,h}$  is the carrier effective mass in the barrier,  $L_b$  is the barrier width, and  $h$  is the Plank constant. The field dependent tunneling barrier,  $H'_{e,h}$ , is very similar to the thermionic emission barrier,  $H_{e,h}$ , except that  $L_w$  is replaced with  $(L_w + L_b)$ , and it is expressed as:

$$H'_{e,h} = \Delta E_{c,v} - E_{e,h}^{(n)} - \frac{|e|F(L_w + L_b)}{2} \quad (6.5)$$

The tunneling time is not temperature sensitive, but it depends heavily on the effective mass of the carriers. It also decreases with electrical field due to the reduction of effective tunneling barrier height. When  $n=1$  energy level in a quantum well is in resonance with  $n=2$  energy level in the adjacent quantum well, the tunneling time could exhibit a drastic decrease due to a sudden large increase in the number of available tunneling states. This effect is also known as resonant tunneling and has been observed by several groups [83][86][87].

Once the carriers escape the well, they leave the intrinsic region under the applied electrical field to the two electrodes, where they will be collected. The carriers are accelerated at saturation velocity ( $v_e = 8 \times 10^6 \text{ cm/s}$ ,  $v_h = 6 \times 10^6 \text{ cm/s}$ ) during most of the drift time across intrinsic region when the applied field is greater than  $50 \text{ kV/cm}$  [84][85][87]. But the actual saturation velocity in the quantum well region will be smaller than in bulk GaAs since the carriers are experiencing a non-uniform material when they travel across the quantum wells and barriers.

The calculated carrier transit time for the quantum well structure ( $75 \text{ \AA}$  GaAs quantum well with  $35 \text{ \AA}$   $\text{Al}_{0.35}\text{Ga}_{0.65}\text{As}$  barrier) used in the device are summarized in Table 6.1. The constants used in the calculation are also listed in this table, and the intrinsic region is about  $0.32 \mu\text{m}$  thick.

Note that the electrons and holes have very different thermionic emission time constants. In the GaAs/AlGaAs system, since the valance band offset ( $\Delta E_v = 0.35 \Delta E_g$ ) is smaller than that of the conduction band ( $\Delta E_c = 0.65 \Delta E_g$ ), the holes can be emitted thermionically significantly faster than the electrons. Also the thermionic emission time can be faster in the GaAs/ $\text{Al}_x\text{Ga}_{1-x}\text{As}$  system if lower Al concentration  $x$  is used in the barrier due to the reduction of bandgap offset  $\Delta E_g$ .

At this applied electric field ( $\sim 109 \text{ kV/cm}$ ), tunneling is dominant for the escape of electrons due to the higher thermionic barrier height. Therefore the electrons escape the wells predominantly through tunneling. However, the thermionic time and tunneling time

are on the same order for the holes, hence the holes escape through a combination of field assisted tunneling and thermionic emission. Since the holes have a longer transit time than electrons, this will dominant the turnoff time of the modulator. There might also be pres-

**Table 6.1:** Carrier transit time for GaAs/Al<sub>0.35</sub>Ga<sub>0.65</sub>As quantum well.

Symbol	Description	Value
<b>Constants used in calculation</b>		
$L_w$	quantum well width	75 Å
$L_b$	quantum well barrier width	45 Å
$\Delta E_c$	conduction band difference	0.283 eV
$\Delta E_v$	valence band difference	0.153 eV
$m_{e\_GaAs}$	electron effective mass in GaAs	0.0665 $m_0$
$m_{h\_GaAs}$	hole effective mass in GaAs	0.62 $m_0$
$m_{e\_Al_{0.35}Ga_{0.65}As}$	electron effective mass in Al <sub>0.35</sub> Ga <sub>0.65</sub> As	0.0957 $m_0$
$m_{h\_Al_{0.35}Ga_{0.65}As}$	hole effective mass in Al <sub>0.35</sub> Ga <sub>0.65</sub> As	0.669 $m_0$
$E_e^{(1)}$	1 <sup>st</sup> energy level for electrons	0.0495 eV
$E_{hh}^{(1)}$	1 <sup>st</sup> energy level for heavy holes	0.00778 eV
F	applied electric field at 3.5V	109 kV/cm
<b>Calculated results</b>		
$\tau_{thermal\_e}$	electron thermionic emission time	120 ps
$\tau_{thermal\_h}$	hole thermionic emission time	12 ps
$\tau_{tunneling\_e}$	electron tunneling time	2.67 ps
$\tau_{tunneling\_h}$	hole tunneling time	5.28 ps
$\tau_{drift\_e}$	electron drift time ( $v_e = 8 \times 10^6$ cm/s)	4 ps
$\tau_{drift\_h}$	hole drift time ( $v_h = 6 \times 10^6$ cm/s)	5.33 ps
$\tau_{transit\_e}$	electron transit time	6.62 ps
$\tau_{transit\_h}$	hole transit time	17.45 ps

ence of space charge in the intrinsic region caused by the slow transit holes, which screens the local electric field and further degrades the transit time.

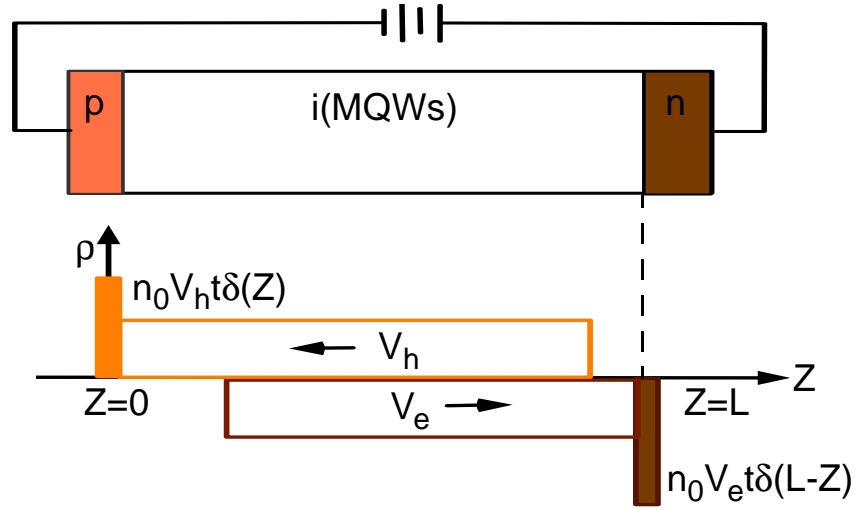


**Figure 6.2:** Photocarrier density distribution at time  $t$ , when  $n_0 v_i t$  carriers have accumulated on the two electrodes.

### 6.1.1.2 Photo-induced electric screening

The escaped electrons and holes, once separated, screen the local electric field in the quantum well region. Figure 6.2 represents a snapshot of the photocarrier density distribution of a p-i-n diode under reverse bias as time evolves after a transient generation of free carriers uniformly over the intrinsic region. In fact, the effective voltage across the intrinsic region is reduced due to this screening effect. Therefore, it detunes the exciton resonance through QCSE and leads to a change of reflectivity by the delayed probe pulse.

The time rate of change of photovoltage is directly proportional to the sum of electron and hole photocurrent. It is the sum of two right-triangular functions, and can be expressed mathematically as:

$$G(t) = \begin{cases} \frac{1}{2} \left( \frac{1}{\tau_e} + \frac{1}{\tau_h} \right) - \frac{t}{4} \left( \frac{1}{\tau_e^2} + \frac{1}{\tau_h^2} \right), & t < 2\tau_e \\ \frac{1}{2\tau_h} - \frac{t}{4\tau_h^2}, & 2\tau_e \leq t \leq 2\tau_h \\ 0, & t > 2\tau_h \end{cases} \quad (6.6)$$

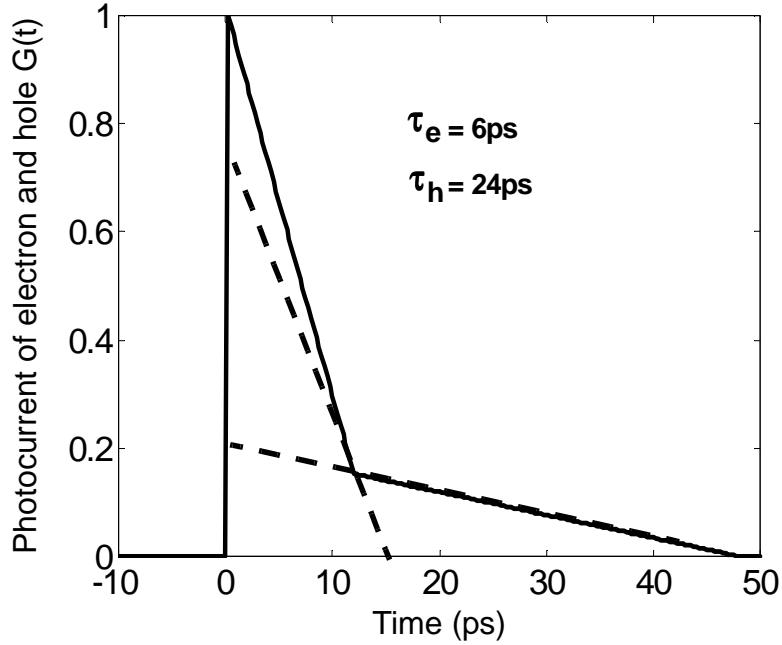


**Figure 6.3:** Normalized electron and hole currents as a function of time.

Figure 6.3 is the plot of this function for electrons and holes, which have different transit times ( $\tau_e = 6\text{ps}$ ,  $\tau_h = 24\text{ps}$ ). One shoulder, which has a faster rate, corresponds to the faster electron transit. The other relatively slower tail corresponds to the slower hole transit time.

In the case of a laser pulse with pulse duration  $\tau_p$ , the photovoltage change rate will be the convolution of the laser pulse with Equation 6.6:

$$G_P(t) = \frac{1}{\sqrt{\pi}\tau_p} \int_{-\infty}^t G(t-t') \cdot e^{-\frac{t'}{\tau_p}} dt' \quad (6.7)$$

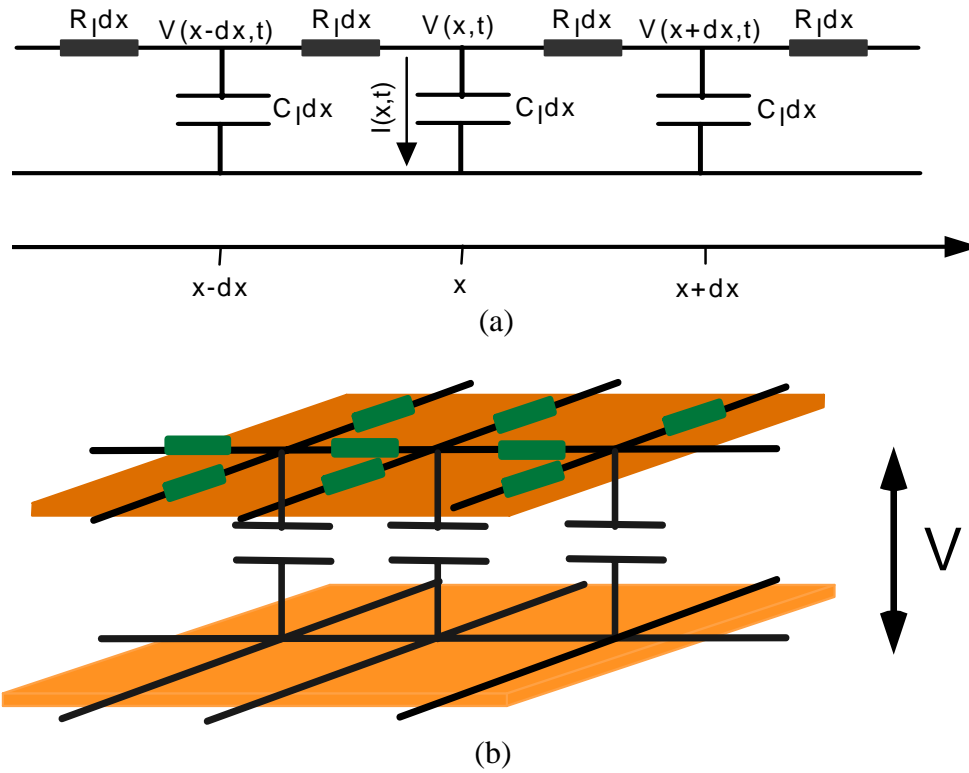


**Figure 6.4:** Propagation of the photo carrier in (a) one dimensional transmission line (b) two dimensional surface with lateral resistance and vertical capacitance.

### 6.1.1.3 Diffusive conduction recovery

In the mean time, the photovoltage under illumination spot recovers through lateral diffusive conduction due to the lateral resistance and vertical capacitance. The diffusive conduction could be a very fast process, very much like the case of an electromagnetic wave propagating along a dissipative transmission line.

Figure 6.4(a) shows schematically a typical dissipative, one dimensional transmission line. For the diffusive propagation of a voltage pulse, it is easy to show that:

$$I(x, t) = \frac{V(x + dx, t) - V(x, t)}{R_l dx} - \frac{V(x, t) - V(x - dx, t)}{R_l dx} \quad (6.8)$$

where  $I(x,t)$  is the conduction current across intrinsic region, which can be expressed as,

$$I(x, t) = C_l dx \frac{\partial V(x, t)}{\partial t} \quad (6.9)$$

where  $R_l$  represents the lateral resistance per unit length of the p and n electrodes and  $C_l$  is the capacitance per unit length associated with the intrinsic region.

From Equations 6.7 and Equation 6.8, the electrostatic potential  $V(x,t)$  can be found to obey the following diffusion equation:

$$\frac{\partial V(x, t)}{\partial t} = \frac{1}{R_l C_l} \frac{\partial^2 V(x, t)}{\partial x^2} \quad (6.10)$$

Analogous to the one dimensional line, the evolution of the voltage,  $V(x,t)$ , for the two dimensional space (Figure 6.4(b)) can be obtained as:

$$\frac{\partial V(x, y, t)}{\partial t} = D \nabla^2 V(x, y, t) \quad (6.11)$$

where  $\nabla^2$  is the Laplacian operator,  $D$  is the effective diffusion coefficient, which is given by:

$$D = \frac{1}{R_{sq} C_A} \quad (6.12)$$

here  $R_{sq}$  is the sum of the resistance per square of the p and n conducting layers, and  $C_A$  is the capacitance per unit area.

In the case where the incident laser pulse is a Gaussian beam with a beam radius ( $w_0$ ) much smaller than the device lateral dimension, the solution to Equation 6.11 can be analytically solved as [87][88]:

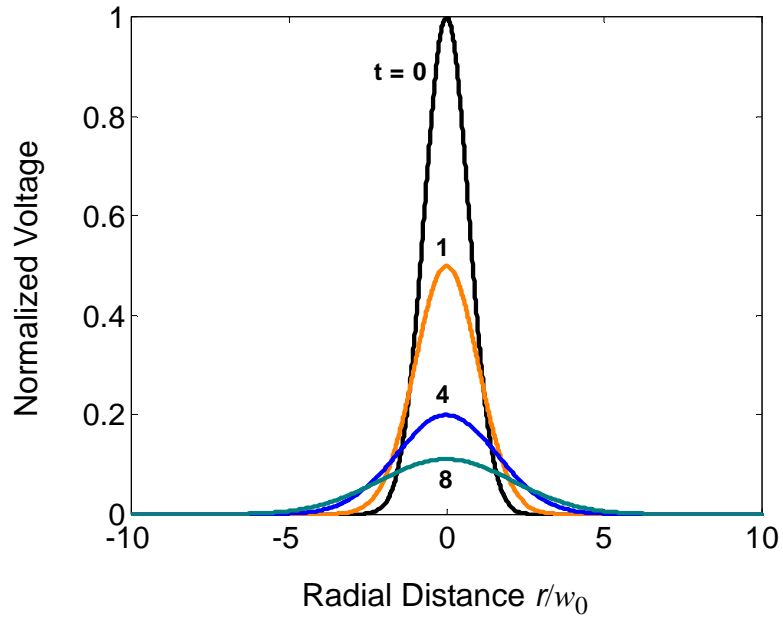


**Figure 6.5:** Voltage relaxation of the initial Gaussian excitation.

$$V(r, t) = V_M \frac{\tau_c}{t + \tau_c} \exp\left(-\frac{r^2}{4D(t + \tau_c)}\right) \quad (6.13)$$

Here  $V_M = 2Q_{\text{tot}}/\pi w_0^2 C_A$ , and  $Q_{\text{tot}}$  is the charge generated by the absorbed photons. The characteristic time  $\tau_c = w_0^2/8D$ , which is the time after which the area of voltage diffusion doubles. This characteristic time, which can be controlled by the illuminating laser pump beam waist, could be much faster than the RC time constant of the device itself, since the photogenerated carriers do not have to reach the contacts to close the optical gates. It is the lateral field variation which drives the diffusion of carriers to wash out the induced voltage.

Figure 6.5 plots the time evolution of the Gaussian voltage perturbation (i.e. Equation 6.13) as a function of the radial distance away from the center of the laser spot.

#### 6.1.1.4 Photovoltage evolution

The total photovoltage change across the intrinsic region which is the sum of these two effects, photovoltage generation and diffusion recovery, can be found by solving the following equation:

$$\frac{\partial}{\partial t} V_{ph} = V_{p, max} \cdot G_p(t) \cdot \exp\left(-\frac{r^2}{\omega_0^2}\right) + D \nabla^2 V_{ph} \quad (6.14)$$

where  $G_p(t)$  is the normalized photovoltage generation rate with laser pulse duration of  $\tau_p$ .

The solution of Equation 6.14 is

$$V_{ph}(r, t) = V_{p, max} \int_{-\infty}^t \frac{dt'' t_c}{(t-t'') + t_c} \cdot \exp\left(\frac{-r^2}{4D(t-t'' + t_c)}\right) \cdot G_p(t'') \quad (6.15)$$

which is simply the convolution of Equation 6.6 and Equation 6.13.

Figure 6.6 shows the calculated time evolution of the normalized photovoltage from Equation 6.15 (at the center of excitation,  $r = 0$ ). Figure 6.6(a) and Figure 6.6(b) show the results with diffusion time ( $t_c$ ) and carrier transit time varied (assume  $\tau_e = \tau_h$ ). Photovoltage increases with larger diffusion time and smaller carrier transit time. This is due to the fact that larger diffusion time and faster carrier transit time allow the photovoltage to build up at the two electrodes. However the larger  $t_c$  also means slow recovery, which slows down the switch off time of the device. Figure 6.6(c) shows a more realistic case where electrons and holes have different transit time. As the hole transit times become larger, a shoulder starts to grow after the peak of photovoltage due to the slow drift of the holes. Effectively it slows the decay time of photovoltage.

The switch-on time ( $\propto t^2$ ) is primarily determined by the laser pulse width and electron transit time and it is relatively fast compared to the switch-off time. The switch-off time

( $\propto 1/t$ ), which is determined by the slower diffusion and slower hole transit time, has a larger tail with a falling slope proportional to the hole transit time. The carrier transit times and diffusion time can be extracted from the photovoltage measurement data.

### **6.1.2 Pump/probe measurement setup**

Figure 6.7 shows the setup of pump/probe measurement, which is used to study the carrier dynamics under picosecond laser excitation. The laser pulses are from a mode-locked Ti:Sapphire laser (diode laser pumped), producing  $\sim 2$ ps pulses at  $\sim 80$ MHz repetition rate. The laser was tuned near 847nm, where the device has the biggest contrast ratio. The device is reverse biased and excited by a picosecond laser pulse (“pump”) to generate photocarriers in the quantum well region. A second weak laser beam (“probe”) then monitors the reflectivity change of the device. The pump beam was chopped at  $\sim 200$ Hz, the probe beam was time-delayed with respect to the probe beam by changing the

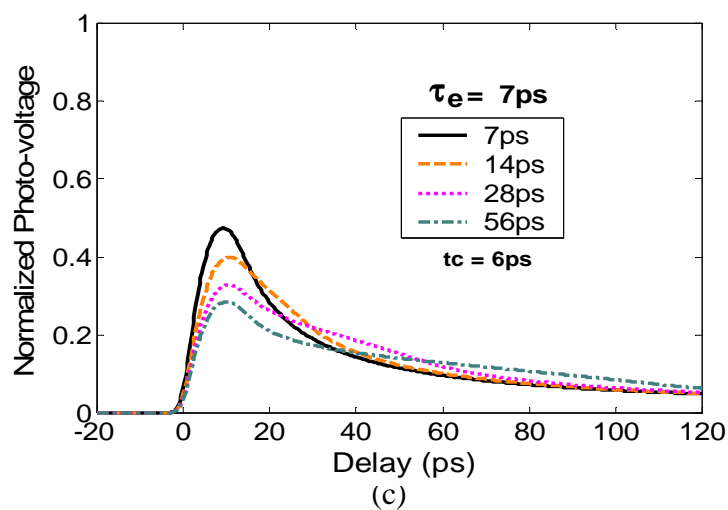
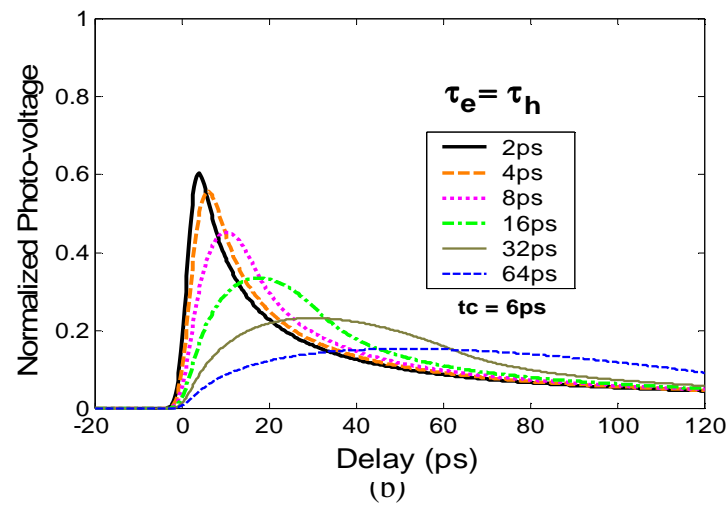
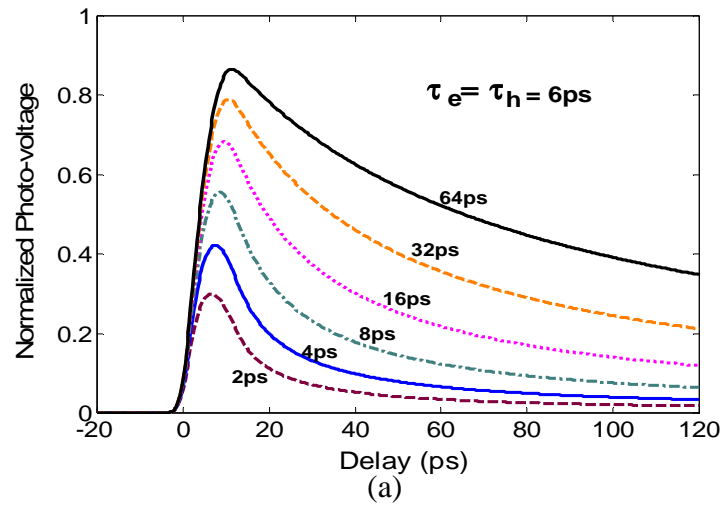


**Figure 6.6:** Time evolution of the normalized photovoltage for different (a) diffusive

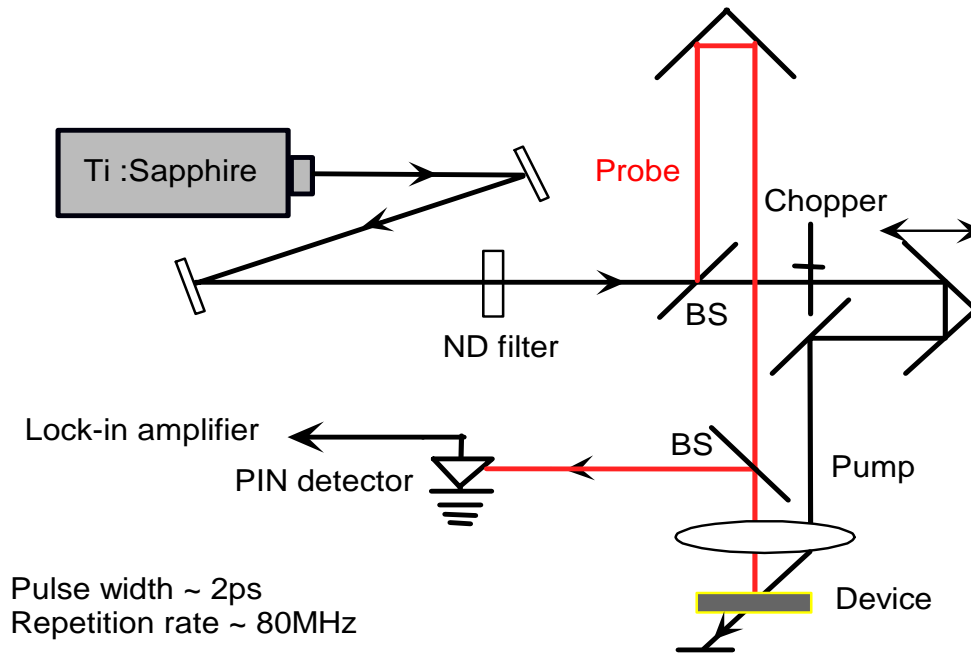


**Figure 6.7:** Schematic of pump/probe setup.

optical path length between these two. The pump and probe beams were brought together to the device by an objective lens.

### 6.1.3 Results and discussion

Figure 6.8(a) shows the time-resolved probe reflectivity change at different bias voltages. Pump optical energy is about 375fJ (30 $\mu$ W), probe power is about 3 $\mu$ W. The spot size of the pump beam is about 20 $\mu$ m. It can be seen at the arrival of the pump beam, the reflectivity change can be either positive or negative depending on the bias condition. For -3.5V bias, where the exciton peak coincides with the Fabry-Perot resonance, the reduced bias voltage caused by the photogenerated voltage shifts exciton resonance peak to shorter

wavelength and increases the reflectivity of the device. While for -8.5V bias voltage, the exciton resonance peak is at a longer wavelength than the Fabry-Perot resonance. The

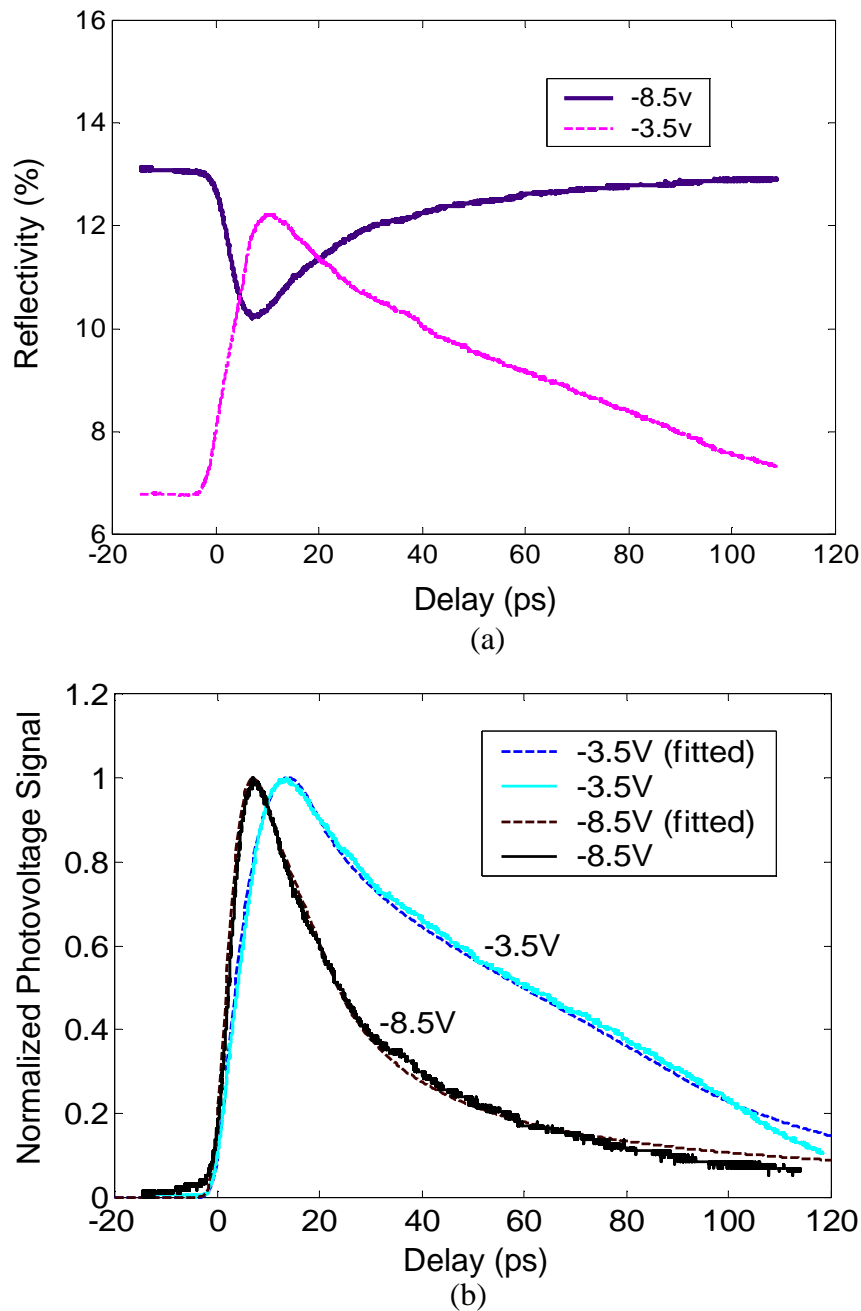


**Figure 6.8:** Measurement result of (a) reflectivity change (b) normalized photovoltage change as function of pump-probe delay time.

reduced bias voltage caused by photogenerated carriers moves the exciton to shorter wavelength and increases the overlap of exciton and Fabry-Perot resonance. Therefore it decreases the reflectivity of the device. Figure 6.8(b) shows the same data normalized to the peak photovoltage value along with the least squares fit of Equation 6.15 with diffusion time, electron and hole transit times as fitting parameters. Note the excellent fit between the theoretical prediction and the experimental data.

The rise and fall times seem to vary with bias conditions. Figure 6.9 shows the rise time as a function of bias voltage. The rise time, which is determined primarily by the faster carrier (electron, for this case) transit time, seem to vary little with bias voltage. The electrons, once they escape from the wells, are traveling at the saturated velocity in this electric field range, therefore are independent of bias voltage [84][85]. The little peak of the rise time could be due to the resonant tunneling of carriers escaping from quantum wells [83][92]. Figure 6.10 shows the measured fall time as a function of bias voltage. The fall time decreases exponentially as the bias voltage increases from 3V to 9V. The fall time, which is dominated by the slower hole transit time, is longer than the theoretically

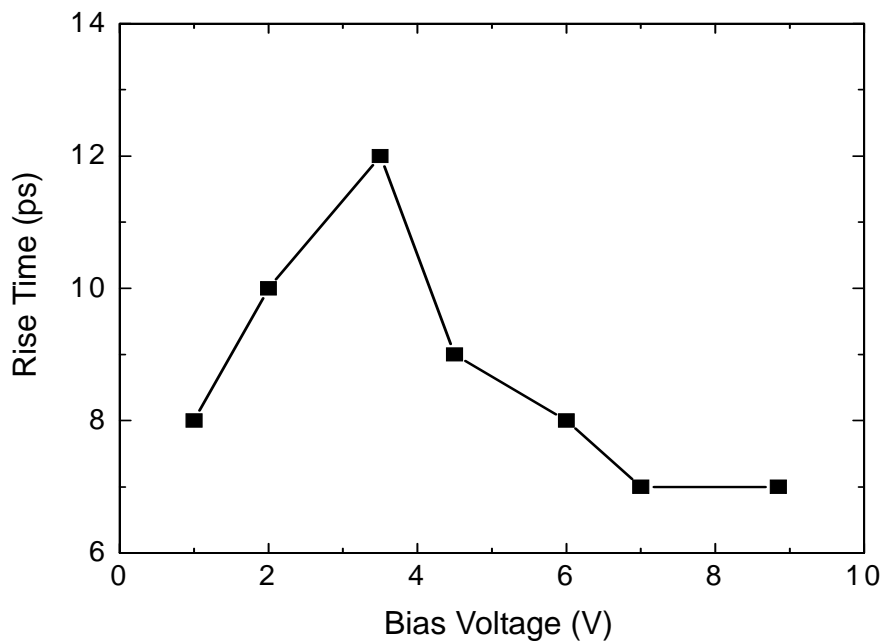


**Figure 6.9:** Rise time of the device as a function of bias voltage.

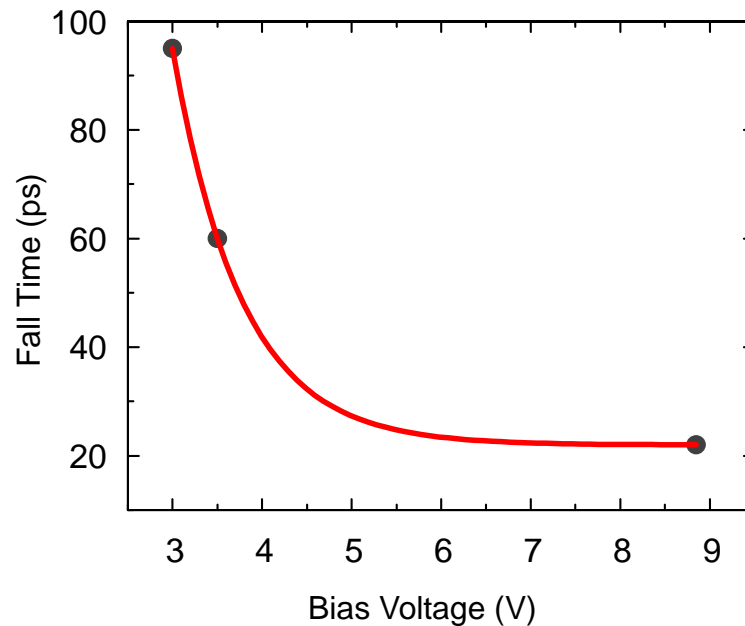


**Figure 6.10:** Fall time as a function of bias voltage.

predicted time in Table 6.1, especially at low bias voltages. This most likely results from the fact that the holes have a significant possibility of being recaptured by subsequent quantum wells. The carrier recapture effectively increases the recovery time of the device and was ignored in this calculation.

## 6.2 High Speed Photocurrent

### 6.2.1 High speed dual function photodetector

A vertical cavity modulator can serve the dual function as a high efficiency resonant cavity photodetector. The dual functioned modulator-photodetector can double optical I/O to a photonic layer. It also helps reducing the optical loss associated with providing multiple optical paths to the optoelectronic chips when bidirectional communication is needed [27].

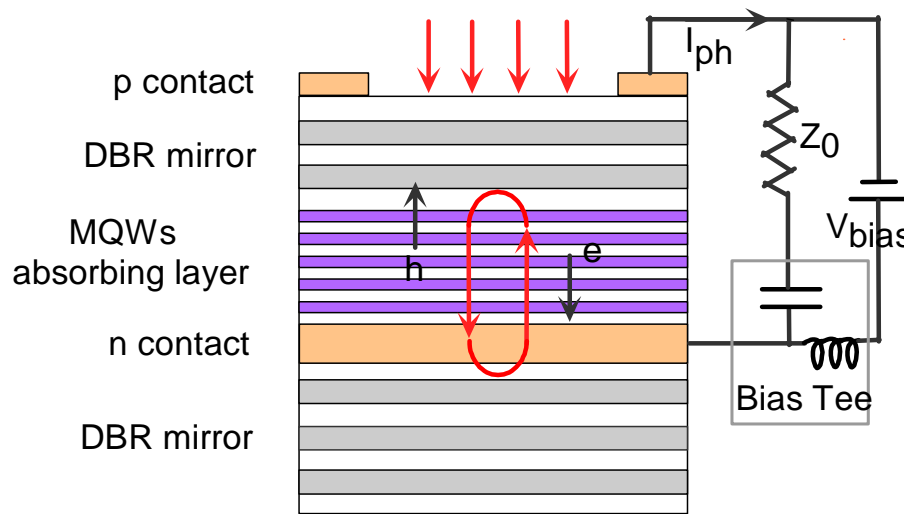


**Figure 6.11:** High speed modulator works as a high efficiency photodetector.

A vertical cavity modulator, while operating in reflection mode, is also a photodetector of high quantum efficiency. The quantum efficiency of a photodetector is defined as the fractional number of electron-hole pairs generated by a single photon. On the assumption that all the generated electron-hole pairs contribute to the photocurrent, the quantum efficiency is simply the ratio of absorbed power to the incident optical power. As illustrated in Figure 6.11, the resonant cavity structure of the modulator increases the quantum efficiency of a PIN photodetector at the resonant wavelength. At the resonant wavelength, where the device has the minimum reflectivity and the back mirror reflectivity is greater than 99%, most of the incident light is absorbed in the intrinsic region and near unity quantum efficiency can be achieved.

There are two competing limitations on the modulation speed of such a photodetector: RC time constant and carrier-transit time. As shown in Figure 6.11, the photo generated carrier pairs move in opposite directions under an external electrical field. The motion of the carriers results in a current, therefore a voltage drop in the external resistor. When the carriers reach the two electrodes, they neutralize and close the current loop. The 3dB bandwidth due to RC time limit for a device with equivalent circuit like Figure 6.12 is:

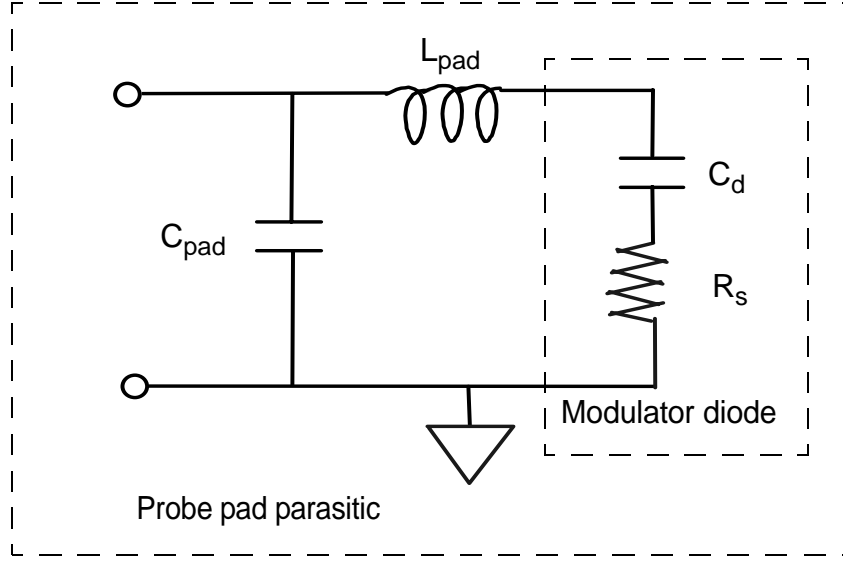


**Figure 6.12:** Equivalent circuit model of photodetector diode and probe pad.

$$f_{RC} = \frac{1}{2\pi[C_{dev}(R_s + Z_0) + C_{pad}Z_0]} \quad (6.16)$$

where the capacitance of the diode itself,  $C_{dev}$ , is:

$$C_{dev} = \frac{\epsilon A}{d} \quad (6.17)$$

which is inversely proportional to the intrinsic region  $d$ .

The frequency response of the photocurrent due to carrier transit, derived from Equation 6.6 by doing Fourier transform, is represented as:

$$\left| \frac{i(f)}{i(0)} \right| = \frac{1}{2} \left( \frac{\sin \pi f \tau_e}{\pi f \tau_e} \right)^2 + \frac{1}{2} \left( \frac{\sin \pi f \tau_h}{\pi f \tau_h} \right)^2 \quad (6.18)$$

where carrier transit times are proportional to the intrinsic region thickness  $d$  as given by

$$\tau_{e,h} = \frac{d}{v_{e,h}} \quad (6.19)$$

The photocurrent response, due to both RC and transit time limit, is:

$$\left| \frac{i^2(f)}{i^2(0)} \right|_{indB} = -10 \log \left( 1 + \frac{f^2}{f_{RC}^2} \right) + 20 \log \left( \frac{1}{2} \left( \frac{\sin \pi f \tau_e}{\pi f \tau_e} \right)^2 + \frac{1}{2} \left( \frac{\sin \pi f \tau_h}{\pi f \tau_h} \right)^2 \right) \quad (6.20)$$

Figure 6.13 shows the modulation bandwidth as a function of intrinsic region thickness for devices with different dimensions. There are trade-offs between RC and transit time limit in choosing the intrinsic region thickness for a high speed photodetector. This compromise limits the speed which a photodetector, with given dimensions, may achieve. Some complex epitaxial layer designs, like a dual-depletion region, have been used to

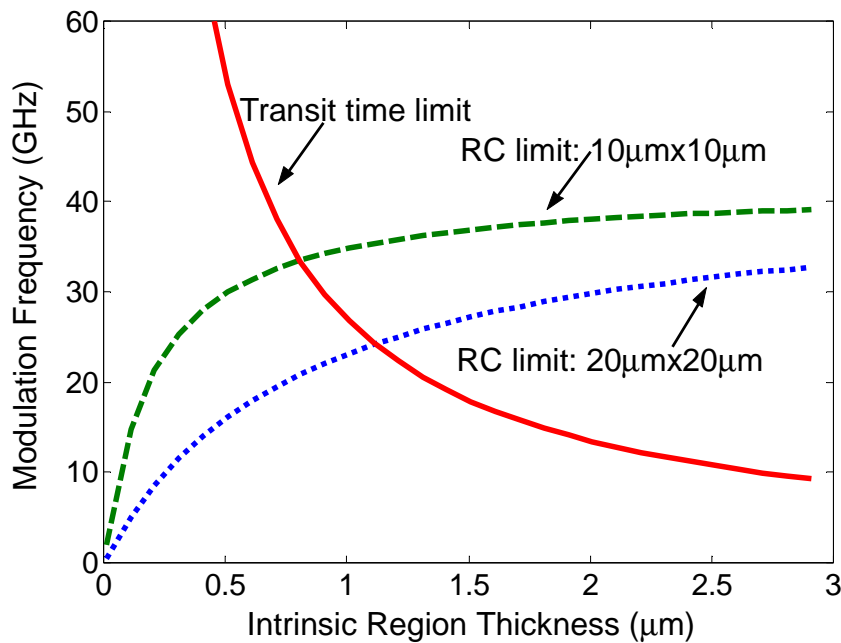


**Figure 6.13:** P-I-N photodetector bandwidth dependence on depletion intrinsic region thickness for  $10\mu\text{m} \times 10\mu\text{m}$  and  $20\mu\text{m} \times 20\mu\text{m}$  devices.

overcome this limit [93], but most of the high speed photodetectors work in the region where the RC and carrier transit times are nearly equal.

## 6.2.2 Characterization and discussion

The high speed photocurrent response of the dual-function modulator-photodetector is measured using the setup shown in Figure 6.14. The laser is focused onto the device and the resulting photocurrent is fed into the high frequency spectrum analyzer HP 8566B. The Ti:Sapphire laser produces 847nm, 200fs pulses at an 80MHz repetition rate. In the frequency domain, these laser pulses are equivalent to broad bandwidth laser source at a comb frequency of 80MHz. The DC bias of the device is applied through a high frequency bias T. The frequency spectrum of the pulse laser stream is flat in the frequency range we measured. Any roll off of the signal, after the calibration of the cables and bias tee, is due to the frequency response of the photodetector.

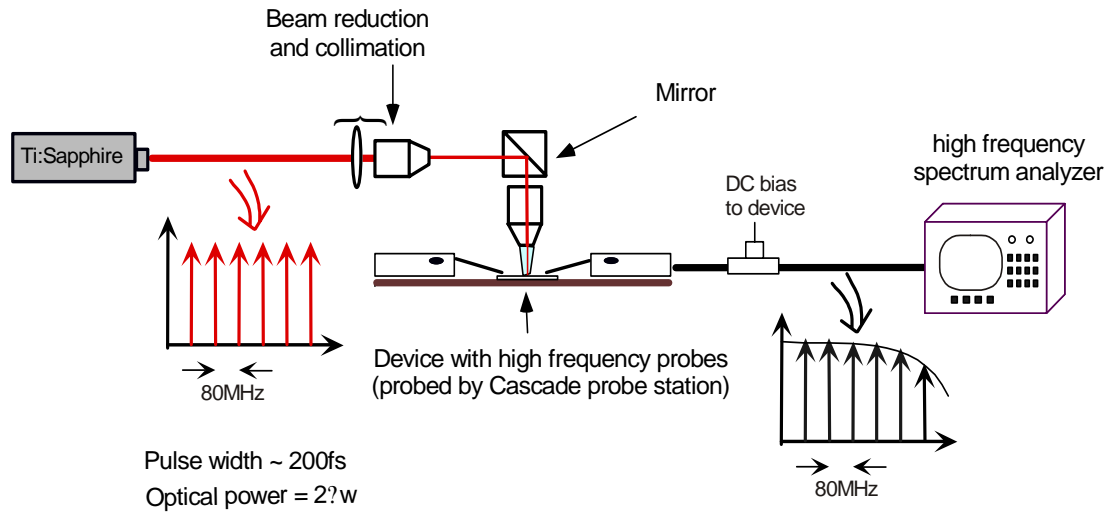


**Figure 6.14:** Schematic of high speed photodetector characterization setup.

For a  $40\mu\text{m}\times 40\mu\text{m}$  device at an optical power of  $2\mu\text{W}$  with  $-3.5\text{V}$  bias, where the device has minimum reflectivity, the measured photocurrent signal at  $100\text{MHz}$  is  $-70.74\text{dBm}$ , which corresponds to a quantum efficiency of about 95%. Figure 6.15 shows its normalized photocurrent response. The 3dB bandwidth is about  $4.5\text{GHz}$ . The dashed line is the frequency response due to RC limitation, using the R, C parameters from the equivalent circuit extraction experiment in Section 5.1. The dotted line is due to carrier transit limitation (Equation 6.18), using the carrier transit times ( $\tau_e=6\text{ps}$ ,  $\tau_h=32\text{ps}$ ), which we measured in the pump-probe measurement. The solid curve includes both RC and carrier transit limit (Equation 6.20), and it agrees well with the measured photocurrent data. This proves that the bandwidth of this photodetector has both RC and carrier transit contributions to its frequency response.

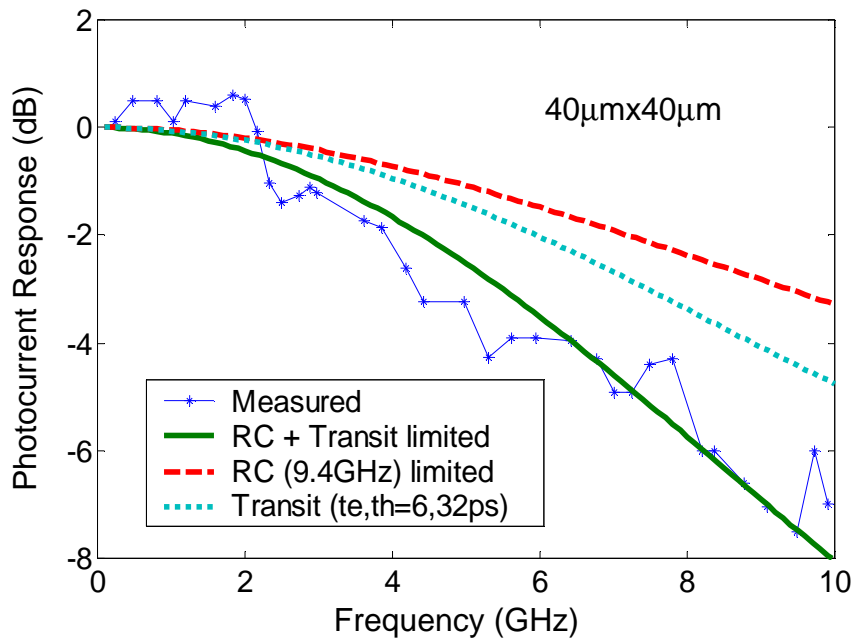


**Figure 6.15:** High speed photocurrent response of the  $40\mu\text{m}$  device.

Normalized photocurrent frequency response for a  $40\mu\text{m} \times 40\mu\text{m}$  device at different bias voltages were also measured as shown in Figure 6.16(a). Modulation  $f_{3\text{dB}}$  bandwidth increases at higher bias voltage due to faster carrier transit time. However, there is little  $f_{3\text{dB}}$  bandwidth improvement for higher bias voltages. This is because the carriers have already reached the saturation velocity at bias voltage greater than  $-2\text{V}$ .

Figure 6.16(b) shows the normalized photocurrent frequency response for devices at  $-3.5\text{V}$  bias voltage for different device sizes of  $10\mu\text{m}$ ,  $20\mu\text{m}$  and  $40\mu\text{m}$ . The smaller device has the higher  $3\text{dB}$  bandwidth due to the smaller RC constant. However, a smaller modulation bandwidth improvement is seen for device smaller than  $20\mu\text{m}$  due to the dominance of fringing capacitance which does not scale with area.

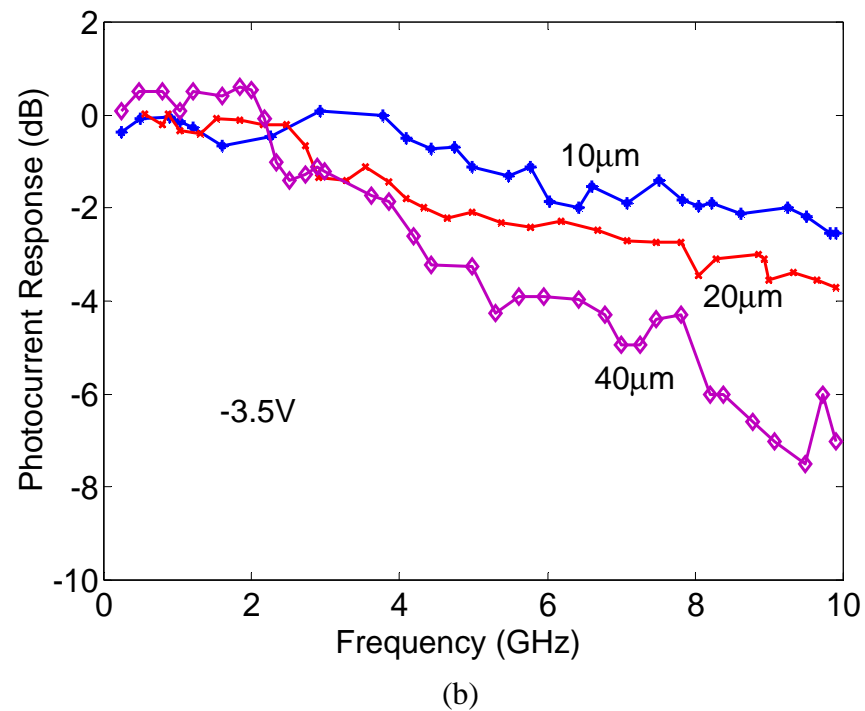
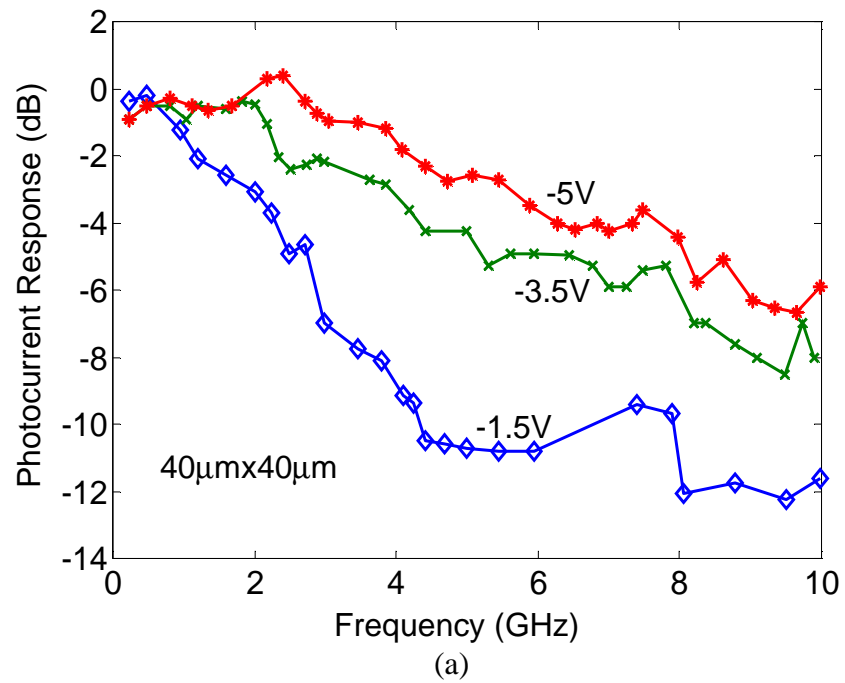


**Figure 6.16:** Photocurrent response for (a)  $40\mu\text{m} \times 40\mu\text{m}$  device under different bias voltages (b) devices of different sizes.



# 7

## *Conclusions*

### **7.1 Summary**

Vertical cavity modulators have wide applications in the area of optical interconnects and optical communication. The motivation of this work was to develop a high speed optical measurement system and de-embedding techniques to provide accurate high speed device parameters. It was also to develop a high speed device models to improve high speed performance and low driving voltage of optical modulators for practical systems application. The design, fabrication and high speed characterization of vertical cavity modulators were investigated.

The first part of the work, Chapter 3, focused on the design of material and device structure to achieve low driving voltage and high speed operation at both low and high optical intensities. Quantum well width and the spacing between exciton and Fabry-Perot peaks were optimized to reduce the operating voltage without sacrificing contrast ratio. To improve the high speed performance of the device, quantum well barrier height was lowered to help the carrier sweep-out at high optical intensity. Resistance and capacitance of the device were also minimized. Specifically, an n-type intracavity contact and highly doped p-contact were used to minimize the series resistance. A semi-insulating substrate and low dielectric constant passivation layer were used to minimize the parasitic capacitance of the device probe pads.

Chapter 4 discussed the device fabrication and DC characterization. Photo sensitive BCB was used as a passivation layer in the fabrication as it has a high degree of planarization and good via shape. The device has very good DC performance with a small switching voltage of 3.5V, large contrast ratio of greater than 11dB, and small insertion loss of less than 1.74dB.

In Chapter 5, an accurate de-embedding technique was described which was used to extract the equivalent circuit parameters from microwave scattering parameter measurements. We also investigated how resistance and capacitance scale with respect to the device physical dimensions, as this will help device design to improve performance. The result of electro-optical modulation response was also discussed for devices with different sizes and under different bias conditions with and without termination of matching resistance.

Chapter 6 discussed the high speed properties of the device under ultrafast optical laser excitation. Carrier dynamics of the device were investigated and carrier transit times were extrapolated from the experimental data. The photocurrent response of the device was measured and this response demonstrated that both RC and carrier transit time limit the response speed. The results also demonstrate that the vertical cavity modulator can perform the dual-function of a high speed photodetector with near unity quantum efficiency.

## 7.2 Future Work

There are many issues related to high speed vertical cavity modulators that are interesting for future work. These issues can be summarized as (i) improving device performance and (ii) investigating the techniques to use the device in the large system.

The bandwidth of the current device is limited by series resistance of the p-type DBR mirror contact. A traditional MBE p-type dopant is Beryllium (Be). However since Beryllium diffuses rapidly under high temperature and/or high drift fields at high concentrations, relatively moderate doping levels must be used. This results in a relatively high resistance for the p-contact layer of these devices. Carbon doping using  $\text{CBr}_4$  in MBE has generated a lot of attention lately because Carbon has a diffusivity several orders of magnitude lower than Be. Using heavily carbon-doped  $\text{Al}_x\text{Ga}_{1-x}\text{As}$  will be very important in reducing DBR mirror series resistance.

The probe pad capacitance of our device is determined primarily by the probe pad size and spacing. The bandwidth of the device could be improved with smaller probe pad sizes, which have smaller capacitance. This can be done when smaller probes are available and probing is not a problem. The bandwidth should also be able to be improved with proper load termination design. The measured microwave scattering parameters of the devices (like Figure 5.9, Figure 5.13) could be used to find the optimum load. By fabricating integrated thin film resistors at the other end of the diode, the microwave reflection could be reduced and this should improve the modulation bandwidth even more.

Most of the telecommunication systems today use digital modulation, the device is modulated by “0” or “1” pulses from a high frequency pulse generator. Performance is measured by an eye diagram and/or bit-error-rate (BER) measured at the receiving end. Due to the lack of test instruments, such digital characterization was not done in this work. It will be interesting to measure the digital modulation of such a device because this will ultimately provide useful feedback for performance improvement of the design.

One of the challenges in using these types of resonant cavity devices in practical system is the ability to manufacture large arrays of these devices. Due to the growth rate variation across the wafer, either by MBE or MOCVD, the length of the optical cavity is not uniform across the wafer (see Figure 4.3). For the devices to achieve large contrast ratios, the spacing between the heavy hole exciton and Fabry-Perot resonance is crucial. In our system, it was necessary to adjust the optical cavity length before growth of the front mirror to form the optical resonant cavity with same resonant wavelength. Improvement in both wafer uniformity and wafer-to-wafer reproducibility will be important for manufacture of these devices.

The understanding of the high speed operation of the device is not limited to the AlGaAs material system or to modulator/photodetectors. Applying the same device concept and using a new material system (such as GaInNAs on GaAs, or InGaAsP on InP), high speed long wavelength modulator/photodetector arrays can be fabricated at wavelength, such as  $1.3\mu\text{m}$  and  $1.55\mu\text{m}$ , which are the desirable wavelengths for fiber optic communication systems. Because high speed long wavelength VCSELs can also be made

if the epitaxial structure is modified for an active laser, there will be competition between these sources in optical transmitters. The optimization of series resistance and capacitance will help reduce the laser threshold voltage and increase the modulation bandwidth of VCSELs.

## *Appendix A Atlas Input Deck File*

The code listed below is the input file for running Atlas program. The program was used to simulate the space-charge distribution, electrical field and photovoltage screening in the bulk GaAs region, with  $\text{Al}_{0.33}\text{Ga}_{0.67}\text{As}$  under laser illumination.

```
go atlas
```

```
Title Field Profile of GaAs pin diode
```

```
# Define the mesh
mesh space.mult=1.0
#
x.mesh loc=0.0 spac=1.0
x.mesh loc=10.0 spac=2.0
x.mesh loc=20 spac=1.0
x.mesh loc=25 spac=1.0
#
y.mesh loc=0.0 spac=0.1
y.mesh loc=0.8 spac=0.1
y.mesh loc=0.9 spac=0.01
y.mesh loc=0.95 spac=0.002
y.mesh loc=1.05 spac=0.002
y.mesh loc=1.1 spac=0.01
y.mesh loc=1.2 spac=0.1
y.mesh loc=1.8 spac=0.1
y.mesh loc=1.9 spac=0.01
y.mesh loc=1.95 spac=0.002
y.mesh loc=2.05 spac=0.002
y.mesh loc=2.1 spac=0.01
y.mesh loc=2.2 spac=0.01
y.mesh loc=3.0 spac=0.01
y.mesh loc=4.0 spac=0.1
```

```

y.mesh loc=6.0 spac=0.1
y.mesh loc=8.0 spac=0.5
y.mesh loc=50 spac=5 region num=1 material=AlGaAs y.min=0 y.max=1.0 x.comp=0.33
grad.34=0
region num=2 material=GaAs y.min=1.0 y.max=2.0
region num=3 material=AlGaAs y.min=2.0 y.max=4.0 x.comp=0.33 grad.34=0
region num=4 material=GaAs y.min=4.0
region num=5 material=air y.min=0 y.max=2.5 x.min=20 x.max=30
#
elec num=1 name=ncontact x.min=21 x.max=25 y.min=2.5 y.max=2.5
elec num=2 name=pcontact x.min=0 x.max=18 y.min=0 y.max=0 z.min=2 z.max=4
#
doping region=1 uniform conc=2.0e18 p.type
doping region=3 uniform conc=2.0e18 n.type

# input the models and their parameters
models print conmob srh kla watt consrh auger bgn fldmob shi fermidirac
temperature=300
material material=GaAs taun0=1.0e-9 taup0=1.0e-9
material material=AlGaAs f.bandcomp="/home/hongliu/diode/bogus.lib"
#
method newton autonr
output e.field charge con.band val.band jx.total jy.total j.total
solve init
save outfile="/home/hongliu/diode/data/10beam/2um/2um_diode.out" master
extract init infile="/home/hongliu/diode/data/10beam/2um/2um_diode.out"

extract name="E Field" curve(depth,efield material="GaAs" mat.occno=1 x.val=0.1)
outfile="/home/hongliu/diode/data/10beam/2um/2um_efield"
extract name="Potential" curve(depth,potential material="GaAs" mat.occno=1 x.val=0.1)
outfile="/home/hongliu/diode/data/10beam/2um/2um_potential"
extract name="electron Conc" curve(depth,n.conc material="GaAs" mat.occno=1
x.val=0.1) outfile="/home/hongliu/diode/data/10beam/2um/2um_electron"
extract name="hole conc" curve(depth,p.conc material="GaAs" mat.occno=1 x.val=0.1)
outfile="/home/hongliu/diode/data/10beam/2um/2um_holeconc"
extract name="intrinsic doping" curve(depth,intrinsic material="GaAs" mat.occno=1
x.val=0.1) outfile="/home/hongliu/data/10beam/2um/2um_intrinsic"

```

```
# Optical source definition
```

```
beam num=1 x.origin=0 y.origin=-1 angle=90.0 wavelength=0.83 min.window=0  
max.window=10
```

```
solve vgate=0 vstep=0.1 vfinal=0.5 name=ncontact
```

```
solve vgate=0.5 vstep=0.5 vfinal=3 name=ncontact
```

```
save outfile="/home/hongliu/diode/data/10beam/2um/2um_diode3v.out" master
```

```
extract init infile="/home/hongliu/diode/data/10beam/2um/2um_diode3v.out"
```

```
extract name="net doping" curve(depth,impurity="Net Doping" material="GaAs"  
mat.occno=1 x.val=0.1) outfile="/home/hongliu/data/10beam/2um/2um_netdoping"
```

```
extract name="Potential" curve(depth,potential material="GaAs" mat.occno=1 x.val=0.1)  
outfile="/home/hongliu/diode/data/10beam/2um/2um_potential3v"
```

```
extract name="electron Conc" curve(depth,n.conc material="GaAs" mat.occno=1  
x.val=0.1) outfile="/home/hongliu/diode/data/10beam/2um/2um_electron3v"
```

```
extract name="hole conc" curve(depth,p.conc material="GaAs" mat.occno=1 x.val=0.1)  
outfile="/home/hongliu/diode/data/10beam/2um/2um_holeconc3v"
```

```
extract name="E Field" curve(depth,efield material="GaAs" mat.occno=1 x.val=0.1)  
outfile="/home/hongliu/diode/data/10beam/2um/2um_efield3v"
```

```
solve b1=0.0001 vgate=3 name=ncontact
```

```
solve b1=0.01 vgate=3 name=ncontact
```

```
solve b1=1 vgate=3 name=ncontact
```

```
solve b1=10 vgate=3 name=ncontact
```

```
solve b1=100 vgate=3 name=ncontact
```

```
solve b1=1000 vgate=3 name=ncontact
```

```
solve b1=2500 vgate=3 name=ncontact
```

```
save outfile="/home/hongliu/diode/data/10beam/2um/2um_diode2500.out" master
```

```
extract init infile="/home/hongliu/diode/data/10beam/2um/2um_diode2500.out"
```

```
extract name="E Field" curve(depth,efield material="GaAs" mat.occno=1 x.val=0.1)  
outfile="/home/hongliu/diode/data/10beam/2um/2um_efield2500"
```

```
extract name="Potential" curve(depth,potential material="GaAs" mat.occno=1 x.val=0.1)  
outfile="/home/hongliu/diode/data/10beam/2um/2um_potential2500"
```

```
extract name="electron Conc" curve(depth,n.conc material="GaAs" mat.occno=1  
x.val=0.1) outfile="/home/hongliu/diode/data/10beam/2um/2um_electron2500"
```

```
extract name="hole conc" curve(depth,p.conc material="GaAs" mat.occno=1 x.val=0.1)
outfile="/home/hongliu/diode/data/10beam/2um/2um_holeconc2500"
```

```
solve b1=5000 vgate=3 name=ncontact
solve b1=7500 vgate=3 name=ncontact
solve b1=8750 vgate=3 name=ncontact
```

```
solve b1=10000 vgate=3 name=ncontact
save outfile="/home/hongliu/diode/data/10beam/2um/2um_diode10k.out" master
extract init infile="/home/hongliu/diode/data/10beam/2um/2um_diode10k.out"
extract name="E Field" curve(depth,efield material="GaAs" mat.occno=1 x.val=0.1)
outfile="/home/hongliu/diode/data/10beam/2um/2um_efield10k"
extract name="Potential" curve(depth,potential material="GaAs" mat.occno=1 x.val=0.1)
outfile="/home/hongliu/diode/data/10beam/2um/2um_potential10k"
extract name="electron Conc" curve(depth,n.conc material="GaAs" mat.occno=1
x.val=0.1) outfile="/home/hongliu/diode/data/10beam/2um/2um_electron10k"
extract name="hole conc" curve(depth,p.conc material="GaAs" mat.occno=1 x.val=0.1)
outfile="/home/hongliu/diode/data/10beam/2um/2um_holeconc10k"
```

```
solve b1=12500 vgate=3 name=ncontact
solve b1=15000 vgate=3 name=ncontact
solve b1=17500 vgate=3 name=ncontact
solve b1=20000 vgate=3 name=ncontact
save outfile="/home/hongliu/diode/data/10beam/2um/2um_diode20k.out" master
extract init infile="/home/hongliu/diode/data/10beam/2um/2um_diode20k.out"
extract name="E Field" curve(depth,efield material="GaAs" mat.occno=1 x.val=0.1)
outfile="/home/hongliu/diode/data/10beam/2um/2um_efield20k"
extract name="Potential" curve(depth,potential material="GaAs" mat.occno=1 x.val=0.1)
outfile="/home/hongliu/diode/data/10beam/2um/2um_potential20k"
extract name="electron Conc" curve(depth,n.conc material="GaAs" mat.occno=1
x.val=0.1) outfile="/home/hongliu/diode/data/10beam/2um/2um_electron20k"
extract name="hole conc" curve(depth,p.conc material="GaAs" mat.occno=1 x.val=0.1)
outfile="/home/hongliu/diode/data/10beam/2um/2um_holeconc20k"
```

```
quit
```

# Appendix B Coplanar Waveguide Parameters

This appendix gives analytical expressions of circuit parameters for the coplanar waveguide with infinite ground planes, finite-extent ground planes, and a lower ground plane. These parameters include the effective permittivity,  $\epsilon_{eff}$ , the characteristic impedance,  $Z_0$ , the capacitance per unit length,  $C$ , and the inductance per unit length  $L$ . The analytical expressions are obtained by means of either exact or an approximate conformal mapping technique. More accurate values can be calculated from Agilent ADS, which uses a spectral-domain approach [67].

## A.1 Coplanar waveguide with infinite ground plane

For a coplanar waveguide with an infinite ground plane (CPW) as shown in Figure B.1. The microwave parameters are [68]

$$\epsilon_{eff} = 1 + \frac{\epsilon_r - 1}{2} \frac{K(k')K(k_1)}{K(k)K(k_1')} \quad (\text{B.1})$$

$$Z_0 = \frac{30\pi}{\sqrt{\epsilon_{eff}}} \frac{K(k')}{K(k)} \quad (\text{B.2})$$

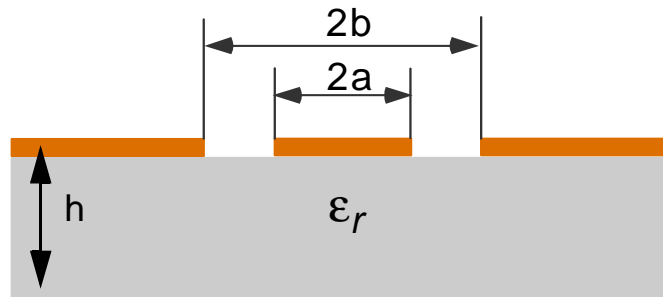


**Figure B.1:** Coplanar waveguide with infinite ground plane (CPW).

$$C = \epsilon_0 \epsilon_r \frac{K(k_1)}{K(k_1')} \quad (\text{B.3})$$

$$L = Z_0 \sqrt{\mu_0 \epsilon_0 \epsilon_{eff}} \quad (\text{B.4})$$

Where  $\epsilon_0$  and  $\mu_0$  are permittivity and permeability of vacuum, and

$$k = a/b \quad (\text{B.5})$$

$$k' = \sqrt{1 - k^2} \quad (\text{B.6})$$

$$k_1 = \sinh(\pi a/2h) / \sinh(\pi b/2h) \quad (\text{B.7})$$

$$k_1' = \sqrt{1 - k_1^2} \quad (\text{B.8})$$

$K(k)$  is the complete elliptic integral of the first kind, and can be represented as:

$$K(k) = \int_0^1 \frac{dt}{\sqrt{(1-t^2)(1-kt^2)}} = \int_0^{\pi/2} \frac{d\theta}{\sqrt{1-k\sin^2\theta}} \quad (\text{B.9})$$

## A.2 Coplanar waveguide with lower ground plane

For a coplanar waveguide with an infinite ground plane (CPW) as shown in Figure B.2. The microwave parameters are [69]

$$\epsilon_{eff2} = \frac{1 + \epsilon_r \frac{K(k_2')K(k_3)}{K(k_2)K(k_3')}}{1 + \frac{K(k_2')K(k_3)}{K(k_2)K(k_3')}} \quad (\text{B.10})$$

$$Z_{02} = \frac{60\pi}{\sqrt{\epsilon_{eff2}}} \frac{1}{K(k_2)/K(k_2') + K(k_3)/K(k_3')} \quad (\text{B.11})$$

$$C_2 = 2\epsilon_0 \frac{K(k_2)}{K(k_2')} + 2\epsilon_0 \epsilon_r \frac{K(k_1)}{K(k_1')} \quad (\text{B.12})$$

$$L = Z_{02} \sqrt{\mu_0 \epsilon_0 \epsilon_{eff2}} \quad (\text{B.13})$$

Where  $\epsilon_0$  and  $\mu_0$  are permittivity and permeability of vacuum, and

$$k_2 = a/b \quad (\text{B.14})$$

$$k_2' = \sqrt{1 - k_2^2} \quad (\text{B.15})$$

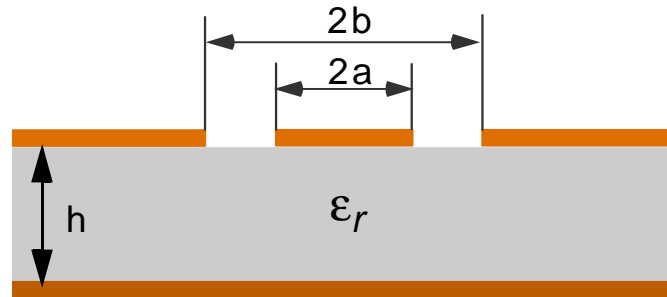


**Figure B.2:** Coplanar waveguide with lower ground plane.

$$k_3 = \tanh(\pi a/2h) / \tanh(\pi b/2h) \quad (\text{B.16})$$

$$k_3' = \sqrt{1 - k_3^2} \quad (\text{B.17})$$

$K(k)$  is the complete elliptic integral of the first kind.

### A.3 Coplanar waveguide with finite ground plane

For a coplanar waveguide with a finite lateral ground plane as shown in Figure B.3. The microwave parameters are [70]

$$\epsilon_{eff3} = 1 + \frac{\epsilon_r - 1}{2} \frac{K(k_4')K(k_5)}{K(k_4)K(k_5')} \quad (\text{B.18})$$

$$Z_{03} = \frac{30\pi}{\sqrt{\epsilon_{eff3}}} \frac{K(k_4')}{K(k_4)} \quad (\text{B.19})$$

$$C_3 = 4\epsilon_0\epsilon_r \frac{K(k_4)}{K(k_4')} + 2\epsilon_0(\epsilon_r - 1) \frac{K(k_5)}{K(k_5')} \quad (\text{B.20})$$

$$L_3 = Z_{03} \sqrt{\mu_0\epsilon_0\epsilon_{eff3}} \quad (\text{B.21})$$

Where  $\epsilon_0$  and  $\mu_0$  are permittivity and permeability of vacuum, and

$$k_4 = \frac{a}{b} \cdot \sqrt{\frac{1 - b^2/c^2}{1 - a^2/c^2}} \quad (\text{B.22})$$

$$k_4' = \sqrt{1 - k_4^2} \quad (\text{B.23})$$

$$k_5 = \frac{\sinh(\pi a/2h)}{\sinh(\pi b/2h)} \sqrt{\frac{1 - \sinh^2(\pi b/2h) / \sinh^2(\pi c/2h)}{1 - \sinh^2(\pi a/2h) / \sinh^2(\pi c/2h)}} \quad (\text{B.24})$$

$$k_5' = \sqrt{1 - k_5^2} \quad (\text{B.25})$$

$K(k)$  is the complete elliptic integral of the first kind.

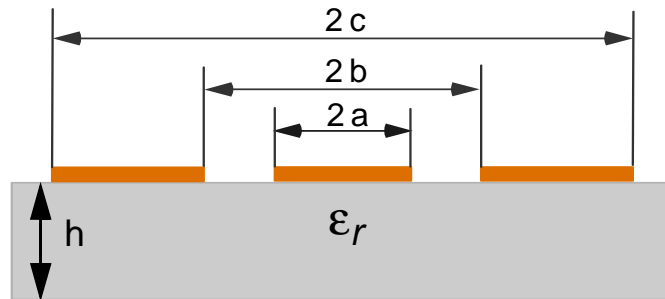


**Figure B.3:** Coplanar waveguide with finite lateral ground plane.



# *Appendix C High-speed Modulator Fabrication Process Flow*

## **Front Pcontact lithography (mask PCONTACT)**

20 min singe at 120°C  
Spin HMDS at 3000rpm for 40sec  
Spin 3612 photoresist at 3000rpm for 40sec  
Prebake at 90°C for 20min  
15 min chlorobenzene immersion  
5 min bake @ 90°C  
Expose 1.8 sec @ 30mW/cm<sup>2</sup> using Karl Suss Aligner  
Develop 75sec in LDD26W (1.2 μm thick)  
O<sub>2</sub> Plasma etch, 20sccm O<sub>2</sub>, 170mT, 100W, for 30secs  
Dip in HCl:DI (1:1) for 15sec  
E-beam evaporate Ti/Pt/Au 250Å/400Å/1200Å  
Lift off in Acetone/Methanol

## **Ntrench-etch lithography (mask NETCH)**

20 min singe at 120°C  
Spin HMDS at 3000rpm for 40sec  
Spin 3612 photoresist at 3000rpm for 40sec  
Prebake at 90°C for 20min  
Expose 1.8sec  
Develop 75sec in LDD26W  
20 min bake @ 110°C

## **Ntrench-etch**

Etch GaAs and AlGaAs to intracavity contact Al<sub>0.1</sub>Ga<sub>0.9</sub>As region using Plasmaquest ECR-RIE plasma etcher: 13.5sccm Ar, 9.9sccm BCl<sub>3</sub>, 4.0sccm Cl<sub>2</sub>, microwave power (400W), RF plasma power (35W), 2mT, 18°C. Etching rate is about 7423Å/464sec  
Strip photoresist in acetone/methanol  
O<sub>2</sub> Plasma etch, 20sccm O<sub>2</sub>, 170mT, 100W, for 60 min

**Cavity contact lithography (mask NCONTACT)**

20 min singe at 120°C

Spin HMDS at 3000rpm for 40sec

Spin 3612 photoresist at 2000rpm for 40sec

Prebake at 90°C for 20min

15 min chlorobenzene immersion

5 min bake @ 90°C

Expose 1.5sec @ 35mW/cm<sup>2</sup> using Karl Suss Aligner

Develop 70sec in LDD26W (1.6 μm thick)

Etch 12sec in H<sub>2</sub>SO<sub>4</sub>:H<sub>2</sub>O<sub>2</sub>: H<sub>2</sub>O (1:8:160) at 20°C (520Å into contact layer)

O<sub>2</sub> Plasma etch, 20sccm O<sub>2</sub>, 170mT, 100W, for 30secs

Dip in HCl:DI (1:1) for 15sec

E-beam evaporate Au/Ge/Ni/Au 400Å/120Å/125Å/1000Å

Lift off in Acetone/Methanol

Contact annealing

RTA 405°C, 30sec

Step	Time (sec)	Temperature (°C)
Delay	5	25
Ramp	75	405
Stay	30	405
Delay	30	25

**Mesa forming lithography (mask MESA)**

20 min singe at 120°C

Spin HMDS at 3000rpm for 40sec

Spin 3612 photoresist at 2000rpm for 40sec

Prebake at 90°C for 20min

Expose 2.5sec

Develop 60sec in LDD26W (1.64 μm thick)

20 min bake @ 110°C

**Mesa-etch**

Etch GaAs and AlGaAs to semi-insulating region using Plasmaquest ECR-RIE plasma etcher: 13.5sccm Ar, 9.9sccm BCl<sub>3</sub>, 4.0sccm Cl<sub>2</sub>, microwave power (400W), RF plasma power (35W), 2mT, 18°C. Etching rate is about 22000Å/1550sec

Strip photoresist in acetone/methanol

O<sub>2</sub> Plasma etch, 20sccm O<sub>2</sub>, 175mT, 100W, for 60 min

**Dielectric BCB processing (mask BCB)****Spin coating**

Spin AP3000 at 3000rpm for 20sec

Dispense photo BCB at 100rpm

Spread at 500rpm for 30sec

Spin at 5000rpm for 30sec

**Pre-exposure bake**

Immediately hot plate soft bake at 75°C for 90sec

**Exposure and solvent development**

Expose 8.5sec @ 17mW/cm<sup>2</sup> (Cl1) using Karl Suss Aligner

Develop in DS3000 at 32°C (hot plate temperature is set about 45°C) for 225sec (film thickness 5.25 µm)

Dip in DS3000 at 23°C for 10sec

Immediately hot plate bake at 90°C for 60sec

**Thermal curing**

Use BLUEM inertial gas oven to thermal cure the photo BCB using the following profile

Step 1	5min. ramp to 50°C	5 min. soak
Step 2	15 min. ramp to 100°C	15 min. soak
Step 3	15 min. ramp to 150°C	15 min. soak
Step 4	60 min. ramp to 250°C	60 min. soak
Step 5	Natural cool down	

**Plasma Descum**

SF<sub>4</sub>/O<sub>2</sub> plasma etch: 2sccm SF<sub>4</sub>, 18sccm O<sub>2</sub>, 175mT, 100W for 2min (2.6 µm thick). Etch rate is 1.3 µm/2 min.

**Transmission line lithography (mask TRANSMISSION LINE)**

20 min singe at 120°C

Spin HMDS at 3000rpm for 40sec

Spin 3612 photoresist at 2000rpm for 40sec

Prebake at 90°C for 20min

15 min chlorobenzene immersion

5 min bake @ 90°C

Expose 1.5sec @ 35mW/cm<sup>2</sup> using Karl Suss Aligner

Develop 70sec in LDD26W (1.6 μm thick)

O<sub>2</sub> Plasma etch, 20sccm O<sub>2</sub>, 170mT, 100W, for 30secs

Dip in HCl:DI (1:1) for 15sec

E-beam evaporate Ti/Au 500Å/5000Å

Lift off in Acetone/Methanol

# *Bibliography*

- [1] W. J. Dally and J. W. Poulton, *Digital systems engineering*, Cambridge University Press, Cambridge, United Kingdom, 1998.
- [2] A. V. Krishnamoorthy and D. A. B. Miller, "Scaling optoelectronic-VLSI circuit into the 21st century: a technology roadmap," *IEEE J. Sel. Top. Quantum Electron.*, vol. 2, no. 1, pp. 55-76, April 1996.
- [3] R. A. Nordin, A. F. J. Levi, R. N. Nottenburg, J. O'Gorman, T. T. an bun-Ek, and R. A. Logan, "A system perspective on digital interconnection technology," *J. Lightwave Technol.*, vol. 10, no. 6, pp. 811-827, June 1992.
- [4] J. D. Meindl, "Low power microelectronics: retrospect and prospect," *Proceedings of The IEEE*, vol. 83, No.4, pp. 619-635, April 1995.
- [5] H. Johnson and M. Graham, *High Speed Digital Design*, Prentice Hall PTR, Upper Saddle River, NJ, 1993.
- [6] D. S. McCallum and P. S. Guilfoyle, "Smart multiple module communications using free-space optical interconnects," *Proceedings of SPIE, Optoelectronic Interconnects and Packaging*, vol. CR62, pp. 68-87, 1996.
- [7] L. G. Kazovsky, S. Benedetto, and A. Willner, *Optical fiber communication systems*, Artech House, Boston, MA, 1996.
- [8] M. Yoneyama, K. Takahata, T. Otsuji, and Y. Akazawa, "Analysis and application of a novel model for estimating power dissipation of optical interconnections as a function of transmission bit error rate," *J. Lightwave Technol.*, vol. 14, no. 1, pp. 13-21, June 1992.
- [9] D. K. Cheng, *Field and Wave Electromagnetics*, Addison-Wesley, Reading, MA, 1990.
- [10] H. B. Bakoglu, *Circuit, interconnections, and packaging for VLSI*, Addison-Wesley, Reading, MA, 1990.

- [11] M. J. Goodwin and A. J. Moseley, "Application of optoelectronic technologies to high performance electronic processor interconnects," *Opt. and Quantum Electron.*, vol. 26, no. 5, pp. S455-S470, May 1994.
- [12] D. A. B. Miller, "Physical reasons for optical interconnection," *Special Issue on Smart Pixels, Int'l J. Optoelectronics*, vol. 11, no. 3, pp. 155-168, 1997.
- [13] A. L. Lentine, K. W. Goossen, J. A. Walker, L. M. F. Chirovsky, L. A. D'Asaro, and etc., "Arrays of optoelectronic switching nodes comprised of flip-chip-bonded MQW modulators and detectors on silicon CMOS circuitry," *IEEE Photonics Technol. Lett.*, vol. 8, no. 2, pp. 221-223, February 1996.
- [14] H. S. Hinton, "Progress in the smart pixel technologies," *IEEE J. Sel. Top. Quantum Electron.*, vol. 2, no. 1, pp. 14-23, April 1996.
- [15] A. L. Lentine, K. W. Goossen, J. A. Walker, L. M. F. Chirovsky, L. A. D'Asaro, and etc., "High-speed optoelectronic VLSI switching chip with >4000 optical I/O based on flip-chip bonding of MQW modulators and detectors to silicon CMOS," *IEEE J. Sel. Top. Quantum Electron.*, vol. 2, no. 1, pp. 77-84, April 1996.
- [16] H-J J. Yeh and J. S. Smith, "Integration of GaAs vertical-cavity surface emitting laser on Si by substrate removal," *Appl. Phys. Lett.*, vol. 64, no. 12, March 1994.
- [17] F. A. P. Tooley, "Optically interconnected electronics-challenges and choices," *IEEE Proceedings of MPPOI*, pp. 138-145, 1996.
- [18] N. Nagli, "Wide-bandwidth lasers and modulators for RF photonics," *IEEE Trans. Microw. Theory Tech.*, vol. 47, no.7, pp. 1151-1165, 1999.
- [19] F. A. P. Tooley, "Challenges in optically interconnecting electronics," *IEEE J. Sel. Top. Quantum Electron.*, vol. 2, no. 4, pp. 3-13, April 1996.
- [20] G. I. Yayla, P. J. Marchand, and S. Esener, "Speed and energy analysis of digital interconnections: comparison of on-chip, off-chip, and free-space technologies," *Appl. Opt.*, vol. 37, no. 2, pp. 205-227, January 1998.
- [21] C. Fan, B. Mansoorian, D. A. Van Blerkom, M. W. Hansen, V. H. Ozguz, S. C. Esener, and G. C. Marsden, "Digital free-space optical interconnections: a comparison of transmitter technologies," *Appl. Opt.*, vol. 34, no. 17, pp. 3103-3115, June 1995.
- [22] O. Kibar, D. A. Van Blerkom, C. Fan, and S. C. Esener, "Power minimization and technology comparisons for digital free-space optoelectronic interconnections," *J. Lightwave Technol.*, vol. 17, no. 4, pp. 546-555, April 1999.

- [23] D. A. B. Miller, "Rationale and challenges for optical interconnects to electronic chips," *Proc. IEEE*, vol. 88, pp. 728-749, 2000.
- [24] D. G. Cunningham and W. G. Lane, *Gigabit Ethernet Networking*, Macmillan Technical Publishing, Indianapolis, IN, 1999.
- [25] N. K. Dutta, "Power penalty due to timing jitter for lasers modulated without prebias," *Appl. Phys. Lett.*, vol. 67, no. 22, pp. 3230-3232, 1995.
- [26] R. K. Gug and W. E. Hagston, "Enhancement of the quantum-confined stark effect utilizing asymmetric quantum well structures," *Appl. Phys. Lett.*, vol. 74, no. 2, pp. 254-256, 1999.
- [27] A. V. Krishnamoorthy, T. K. Woodward, K. W. Goossen, J. A. Walker, S. P. Hui, B. Tseng, J. E. Cunningham, W. Y. Jan, F. E. Kiamilev, and D. A. B. Miller, "Dual-function detector-modulator smart-pixel module," *Appl. Opt.*, vol. 36, no. 20, pp. 4866-4870, July 1997.
- [28] S. Adachi, "GaAs, AlAs, and  $\text{Al}_x\text{Ga}_{1-x}\text{As}$ : material parameters for use in research and device applications," *J. Appl. Phys.*, vol. 58, no. 3, pp. R1-R29, August 1985.
- [29] J. Batey and S. L. Wright, "Energy band alignment in GaAs:(Al,Ga)As heterostructure: The dependence on alloy composition," *J. Appl. Phys.*, vol. 59, no. 1, pp. 200-209, January 1986.
- [30] J. Singh, *Physics of Semiconductors and their Heterostructure*, McGraw-Hill, New York, NY, 1993.
- [31] S. L. Chuang, *Physics of Optoelectronic Devices*, Wiley, New York, NY, 1995.
- [32] D. A. B. Miller, *Advanced Optoelectronic Devices*, Stanford EE 343 Class Note, Spring 1997.
- [33] D. A. B. Miller, D. S. Chemla, T. C. Damen, A. C. Gossard, W. Wiegmann, T. H. Wood, and C. A. Burrus, "Band-edge electroabsorption in quantum well structures: the quantum-confined stark effect," *Phys. Rev. Lett.*, vol. 53, no. 22, pp. 2173-2176, November 1984.
- [34] D. A. B. Miller, D. S. Chemla, T. C. Damen, A. C. Gossard, W. Wiegmann, T. H. Wood, and C. A. Burrus, "Electric field dependence of optical absorption near the band gap of quantum-well structures," *Phys. Rev. B*, vol. 32, no. 2, pp. 2173-2176, November 1984.

- [35] S. Schmitt-rink, D. S. Chemla, and D. A. B. Miller, "Linear and nonlinear optical properties of semiconductor quantum wells," *Advances in Physics*, vol. 38, no. 2, pp. 89-188, 1989.
- [36] D. C. Hutchings, "Transfer matrix approach to the analysis of an arbitrary quantum well structure in an electric field," *Appl. Phys. Lett.*, vol. 55, no. 11, pp. 1082-1084, September 1989.
- [37] K. Nakamura, A. Shimizu, K. Fujii, M. Koshihara, and K. Hayata, "Numerical analysis of the absorption and the refractive index change in arbitrary semiconductor quantum-well structures," *IEEE J. Quantum Electron.*, vol. 28, no. 7, pp. 1670-1676, July 1992.
- [38] P. J. Stevens, M. Whitehead, G. Parry, and K. Woodbridge, "Computer modeling of the electrical field dependent absorption spectrum of multiple quantum well material," *IEEE J. Quantum Electron.*, vol. 24, no. 10, pp. 2007-2016, October 1988.
- [39] N. Suba and T. Nakahara, "Design of AlGaAs/GaAs quantum wells for electroabsorption modulator," *Solid-State Electron.*, vol. 36, no. 9, pp. 1277-1287, 1993.
- [40] K. W. Jelley, R. W. H. Engelmann, K. Alavi, and H. Lee, "Well size related limitations on maximum electroabsorption in GaAs/AlGaAs multiple quantum well structures," *Appl. Phys. Lett.*, vol. 55, no. 1, pp. 70-72, July 1989.
- [41] M. S. Ünlü and S. Strite, "Resonant cavity enhanced photonic devices," *J. Appl. Phys.*, vol. 78, no. 2, pp. 607-639, July 1995.
- [42] B. Pezeshki, *Optimization of reflection electro-absorption modulators*, Ph.D. Dissertation, Stanford University, CA, June 1991.
- [43] C. Amano, S. Matsuo, T. Kurokawa, and H. Iwamura, "20dB contrast GaAs/AlGaAs multiple quantum-well nonresonant modulators," *IEEE Photonics Technol. Lett.*, vol. 4, no. 1, pp. 31-33, January 1992.
- [44] K. K. Law, J. L. Merz, and L. A. Coldren, "Self-linearized optical modulation of a normally-on asymmetric Fabry-Perot modulator with high contrast, low insertion-loss, and low operating energy," *Jpn. J. Appl. Phys.*, vol. 31, pt. 2, no. 12A, pp. L1699-L1701, 1992.
- [45] J. A. Trezza, M. C. Larson, S. M. Lord, and J. S. Harris, Jr., "Large, low-voltage absorption changes and absorption bistability in GaAs/AlGaAs/InGaAs asymmetric quantum wells," *J. Appl. Phys.*, vol. 74, no. 3, pp. 1972-1978, 1993.

- [46] K. W. Goossen, J. E. Cunningham, and W. Y. Jan, "Stacked-diode electroabsorption modulator," *IEEE Photonics Technol. Lett.*, vol. 6, no. 8, pp. 936-938, August 1994.
- [47] R. T. Sahara, M. Matsuda, K. Morito, and H. Soda, "Type 1.5 coupled quantum wells for electroabsorption modulation with low electric fields," *Opt. and Quantum Electron.*, vol. 28, pp. 599-604, 1996.
- [48] C. C. Barron, C. J. Mahon, B. J. Thibeault, and L. A. Coldren, "Design, fabrication and characterization of high-speed asymmetric Fabry-Perot modulators for optical interconnect applications," *Opt. and Quantum Electron.*, vol. 25, pp. S885-S898, 1993.
- [49] R. J. Simes, R. H. Yan, C. C. Barron, D. Derrickson, D. G. Lishan, J. Karin, L. A. Coldren, M. Rodwell, S. Elliott, and B. Hughes, "High-frequency electrooptic Fabry-Perot modulators," *IEEE Photonics Technol. Lett.*, vol. 4, no. 6, pp. 513-515, June 1991.
- [50] C. C. Barron, M. Whitehead, K. K. Law, J. W. Scott, M. E. Heimbuch, and L. A. Coldren, "K-band operation of asymmetric Fabry-Perot modulators," *IEEE Photonics Technol. Lett.*, vol. 4, no. 5, pp. 459-461, May 1992.
- [51] C. C. Barron, C. J. Mahon, B. J. Thibeault, G. Wang, W. Jiang, L. A. Coldren, and J. E. Bowers, "Millimeter-wave asymmetric Fabry-Perot modulators," *IEEE J. Quantum Electron.*, vol. 31, no. 8, pp. 1484-1493, August 1995.
- [52] M. C. Larson and J. A. Trezza, Private Communication, *FF Program*, Harris Group, Stanford University.
- [53] T. H. Lee, *The Design of CMOS Radio-Frequency Integrated Circuits*, Cambridge University Press, Cambridge, U.K., 1998.
- [54] D. L. Huffaker and D. G. Deppe, "Intracavity contacts for low-threshold oxide-confined vertical-cavity surface-emitting lasers," *IEEE Photonics Technol. Lett.*, vol. 11, no. 8, pp. 934-936, August 1999.
- [55] K. L. Lear and R. P. Schneider, Jr., "Uniparabolic mirror grading for vertical cavity surface emitter lasers," *Appl. Phys. Lett.*, vol. 68, no. 5, pp. 605-607, January 1996.
- [56] S. A. Chalmers, K. L. Lear, and R. P. Schneider, Jr., "Low resistance wavelength-reproducible p-type (Al,Ga)As distributed Bragg reflectors grown by molecular beam epitaxy," *Appl. Phys. Lett.*, vol. 62, no. 14, pp. 1585-1587, 1993.

- [57] M. G. Peters, B. J. Thibeault, D. B. Young, J. W. Scott, F. H. Peters, A. C. Gossard, and L. A. Coldren, "Band-gap engineered digital alloy interfaces for lower resistance vertical-cavity surface-emitting lasers," *Appl. Phys. Lett.*, vol. 63, no. 25, pp. 3411-3413, December 1993.
- [58] J. M. Fastenau and G. Y. Robinson, "Low-resistance visible wavelength distributed Bragg reflectors using smaller energy band offset heterojunctions," *Appl. Phys. Lett.*, vol. 74, no. 25, pp. 3758-3760, June 1999.
- [59] K. L. Bacher, *Improvements Toward High-Efficiency Vertical-Cavity Surface-Emitting Lasers*, Ph.D. Dissertation, Stanford University, CA, June 1995.
- [60] R. F. Kopf, E. F. Schubert, S. W. Downey, and A. B. Emerson, "N- and P-type dopant profiles in distributed Bragg reflector structures and their effect on resistance," *Appl. Phys. Lett.*, vol. 61, no. 15, pp. 1820-1822, July 1992.
- [61] Silovaco, *Atlas*, Silovaco Inc., Sunnyvale, CA.
- [62] B. Deveaud, J. Shah, T. C. Damen, and W. T. Tsang, "Capture of electrons and holes in quantum wells," *Appl. Phys. Lett.*, vol. 52, no. 15, pp. 1886-1888, July 1988.
- [63] N. Peyghambarian, S. W. Koch, and A. Mysyrowicz, *Introduction to semiconductor optics*, Prentice Hall, Englewood Cliffs, NJ, 1993.
- [64] A. M. Fox, D. A. B. Miller, G. Livescu, J. E. Cunningham, and W. Y. Jan, "Quantum well carrier sweep out: relation to electroabsorption and exciton saturation," *IEEE J. Quantum Electron.*, vol. 27, no.10, pp. 2281-2295, October 1991.
- [65] Z. P. Yu and R. Dutton, Private Communication, *PROPHET*, Stanford University.
- [66] R. H. Yan and L. A. Coldren, "Effect of temperature on the operating characteristics of asymmetric Fabry-Perot reflection modulators," *Appl. Phys. Lett.*, vol. 57, no. 3, pp. 267-269, July 1990.
- [67] Hewlett Packard, *HP ADS*, Santa Rose, CA, 1998
- [68] G. Ghione and C. Naldi, "Analytical formulas for coplanar lines in hybrid and monolithic MICs," *Electron. Lett.*, vol. 20, no.4, pp. 179-181, February 1984.
- [69] G. Ghione and C. Naldi, "Parameters of coplanar waveguides with lower ground plane," *Electron. Lett.*, vol. 19, no.18, pp. 734-735, September 1983.

- [70] G. Ghione and C. U. Naldi, "Coplanar waveguides for MMIC applications: effect of upper shielding, conductor backing, finite-extent ground planes, and line-to-line coupling," *IEEE Trans. on Microw. Theory and Tech.*, vol. MTT-35, no. 3, pp. 260-267, March 1987.
- [71] K. Bacher, B. Pezeshki, S. M. Lord, and J. S. Harris, Jr., "Molecular beam epitaxy growth of vertical cavity optical devices with *in situ* corrections," *Appl. Phys. Lett.*, vol. 61, no. 12, pp.1387-1389, September 1992.
- [72] T. Shimoto, K. Matsui, and K. Utsumi, "Cu/Photosensitive-BCB thin-film multilayer technology for high-performance multichip modules," *IEEE Trans. on Compon., Packag., and Manufac. Technol. - Part B*, vol. 18, no. 1, pp. 18-22, February 1995.
- [73] V. B. Krishnamurthy, H. S. Cole, and T. Sitnik-Nieters, "Use of BCB in high frequency MCM Interconnects," *IEEE Trans. on Compon., Packag., and Manufac. Technol. - Part B*, vol. 19, no. 1, pp. 42-47, February 1996
- [74] P. B. Chinoy and J. Tajadod, "Processing and microwave characterization of multilevel interconnects using benzocyclobutene dielectric," *IEEE Trans. on Compon., Hybrids, and Manufac. Technol.*, vol. 16, no. 7, pp. 714-719, November 1993.
- [75] R. Foster, "Photoimageable BCB technology lowers costs for MCMs," *Solid State Technol*, pp. 125-130, June 1995.
- [76] Application Note, *Processing Procedures for Photosensitive Cyclotene Advance Electronics Resins (Photo-BCB)*, The Dow Chemical Company, Midland, MI, 1998.
- [77] P. E. Garrou, R. H. Heistand, M. G. Dibbs, T. A. Mainal, C. E. Mohler, T. M. Stokich, P. H. Townsend, G. M. Adema, M. J. Berry, and I. Turlik, "Rapid thermal curing of BCB dielectric," *IEEE Trans. on Compon., Hybrids, and Manufac. Technol.*, vol. 16, no. 1, pp. 46-51, February 1993.
- [78] Cascade Microtech, *WinCal 2.1*, Beaverton, OR, 1998.
- [79] T. Sakuri and K. Tamaru, "Simple formulas for two and three-dimensional capacitances," *IEEE Trans. on Electron Devices*, vol. Ed-30, no. 2, pp. 183-185, February 1983.
- [80] M. Kakiuchi and M. Yano, "Flip-chip planar GaInAs/InP p-i-n photodiodes analysis of frequency response," *J. Lightwave Technol.*, vol. 14, no. 1, pp. 97-103, January 1996.

- [81] D. Costa, *Microwave and Low-frequency Noise Characterization of Npn AlGaAs/GaAs Heterojunction Bipolar Transistors*, Ph.D. Dissertation, Stanford University, CA, December 1991.
- [82] H. Schneider and K. Von Klitzing, "Thermionic emission and Gaussian transport of holes in a GaAs/AlGaAs multiple-quantum-well structure," *Phys. Rev. B*, vol. 38, pp. 6160-6165, 1988.
- [83] G. Livescu, A. M. Fox, D. A. B. Miller, T. Sizer, and W. H. Knox, "Resonantly enhanced electron tunneling rates in quantum wells," *Phys. Rev. Lett.* vol. 63, pp. 438-441, 1989.
- [84] J. E. Bowers and C. A. Burrus, "Ultrawide-band long-wavelength p-i-n photodetectors," *J. Lightwave Technol.*, vol. LT-5, no. 10, pp. 1339-1350, October 1987.
- [85] S. M. Sze, *Physics of Semiconductor Devices*, Wiley, New York, NY, 1981.
- [86] T. Tasa, A. Yamaguchi, and H. Sakaki, "Tunneling escape rate of electrons from quantum well in double-barrier heterostructure," *Phys. Rev. Lett.*, vol. 59, pp. 2356-2359, 1987.
- [87] J. A. Cavallès, D. A. B. Miller, J. E. Cunningham, P. L. K. Wa, and A. Miller, "Simultaneous measurements of electron and hole sweep-out from quantum wells and modeling of photoinduced field screening dynamics," *IEEE J. Quantum Electron.*, vol. 28, no. 10, pp. 2486-2497, October 1992.
- [88] G. Livescu, D. A. B. Miller, T. Sizer, D. J. Burrowers, and J. E. Cunningham, "High-speed absorption recovery in quantum well diode by diffusive electrical conduction," *Appl. Phys. Lett.*, vol. 54, no. 5, pp. 748-750, February 1989.
- [89] P. J. Bradley, C. Rigo, and A. Stano, "Carrier induced transit electric fields in a p-i-n InP-InGaAs multiple-quantum-well modulator," *IEEE J. Quantum Electron.*, vol. 32, no. 1, pp. 43-52, January 1996.
- [90] D. Mahgerefteh, C. M. Yang, L. Chen, K. Hu, W. Chen, E. Garmire, and A. Madhukar, "Picosecond time-resolved measurements of electroabsorption in an InGaAs/GaAs multiple quantum well p-i-n modulator," *Appl. Phys. Lett.*, vol. 61, no. 21, pp. 2592-2594, November 1992.
- [91] C. M. Yang, E. Canoglu, E. Garmire, K. W. Goossen, J. E. Cunningham, and W. Y. Jan, "Measurement of effective drift velocities of electrons and holes in shallow multiple-quantum-well p-i-n modulators," *IEEE J. Quantum Electron.*, vol. 33, no. 9, pp. 1498-1506, September 1997.

- [92] N. M. Froberg, A. M. Johnson, K. W. Goossen, J. E. Cunningham, M. B. Santos, W. Y. Jan, T. H. Wood, and C. A. Burrus, Jr., "Picosecond carrier escape by resonant tunneling in pseudomorphic InGaAs/GaAsP quantum well modulators," *Appl. Phys. Lett.*, vol. 64, no. 13, pp.1705-1707, March 1994.
- [93] F. J. Effenberger and A. M. Joshi, "Ultrafast, dual-depletion region, InGaAs/Inp p-i-n detector," *J. Lightwave Technol.*, vol. 14, no. 8, pp. 1859-1864, August 1996.
- [94] H. A. MacLeod, *Thin Film Optical Filters*, Macmillan Pub. Co., New York, NY, 1986.

